Biophysical Journal
Article

Identification of Bifurcations from Observations of Noisy Biological Oscillators

Joshua D. Salvi,[1] Dáibhid Ó Maoiléidigh,[1] and A. J. Hudspeth[1,2,*]
[1]Laboratory of Sensory Neuroscience and [2]Howard Hughes Medical Institute, The Rockefeller University, New York, New York

ABSTRACT Hair bundles are biological oscillators that actively transduce mechanical stimuli into electrical signals in the auditory, vestibular, and lateral-line systems of vertebrates. A bundle's function can be explained in part by its operation near a particular type of bifurcation, a qualitative change in behavior. By operating near different varieties of bifurcation, the bundle responds best to disparate classes of stimuli. We show how to determine the identity of and proximity to distinct bifurcations despite the presence of substantial environmental noise. Using an improved mechanical-load clamp to coerce a hair bundle to traverse different bifurcations, we find that a bundle operates within at least two functional regimes. When coupled to a high-stiffness load, a bundle functions near a supercritical Hopf bifurcation, in which case it responds best to sinusoidal stimuli such as those detected by an auditory organ. When the load stiffness is low, a bundle instead resides close to a subcritical Hopf bifurcation and achieves a graded frequency response—a continuous change in the rate, but not the amplitude, of spiking in response to changes in the offset force—a behavior that is useful in a vestibular organ. The mechanical load in vivo might therefore control a hair bundle's responsiveness for effective operation in a particular receptor organ. Our results provide direct experimental evidence for the existence of distinct bifurcations associated with a noisy biological oscillator, and demonstrate a general strategy for bifurcation analysis based on observations of any noisy system.

INTRODUCTION

A bifurcation occurs when a quantitative change in the value of some parameter–a control parameter–induces a qualitative change in the behavior of a system. Bifurcations are often encountered in theoretical and experimental systems in physics, chemistry, biology, medicine, economics, and climatology (1–4). All systems operating near a given type of bifurcation exhibit similar dynamics (5), and systems operating near different bifurcations can exhibit distinct behaviors. Therefore, by identifying a bifurcation, one can determine generic properties of a complex system and predict that system's function when it operates near the bifurcation.

The activity of spiking neurons, for example, can be segregated into at least two classes of excitability, with distinct patterns in the frequency of spiking that are attributed to operation near different types of bifurcation (6–8). Class I neurons display a continuous change in spike frequency in response to changes in stimulus current, a behavior that is commonly ascribed to their operation near a saddle-node on invariant cycle (SNIC) bifurcation (9). Class II neurons, by contrast, exhibit a discontinuous jump in frequency as a function of the applied current, a behavior that is consistent with their crossing a Hopf bifurcation (10). By identifying the type of bifurcation, one can assess generic features of neuronal excitability in different neuronal populations.

Bifurcation analysis is usually conducted on purely mathematical stereotypes or on simplified representations of real-world systems in which the effects of noise are small. In certain experimentally accessible systems, however, noise plays a significant and irreducible role in shaping the dynamics. Among these systems is the hair cell, the sensory receptor of the auditory, vestibular, and lateral-line sensory systems of vertebrate animals (11). A hair cell detects mechanical signals derived from sounds, accelerations, and water movements, transducing them into electrical signals that are transmitted to the brain. This detection is achieved through the motion of a mechanosensitive organelle—the hair bundle—that projects from the hair cell's apical surface and transduces mechanical input into electrical output in the cell body. For small-magnitude stimuli, the hair bundle operates in an environment dominated by noise. In fact, the sensitivity of our hearing is limited by the clattering of air molecules against the eardrum and the rattling of water molecules within the cochlea (12,13). Thermal noise also plays

---

Submitted January 15, 2016, and accepted for publication July 22, 2016.

*Correspondence: hudspaj@rockefeller.edu

Editor: Charles Wolgemuth.
http://dx.doi.org/10.1016/j.bpj.2016.07.027

an important role in setting the sensitivity of vestibular organs (14).

Auditory organs deal with noise by employing an active process, a metabolically powered mechanism that enhances their sensitivity (15). Vestibular systems might also employ the active process to improve their effectiveness. The effects of the active process depend on the values of a sensory organ's parameters (16). For example, it has been hypothesized that auditory hair bundles achieve enhanced frequency selectivity and a broadened dynamic range in response to periodic stimuli when they are poised near the onset of spontaneous oscillation, that is, when they operate close to a supercritical Hopf bifurcation (17–19). Observations of individual bundles support this hypothesis (20). Hair bundles have also been observed to attain a graded frequency response with changes in static offsets, which could occur if hair bundles operate near a SNIC bifurcation or, as we argue below, a subcritical Hopf bifurcation (20–22). We propose that this graded response allows hair bundles to function as static force detectors, which would be of use in a vestibular system. By operating near particular bifurcations, a mechanically active hair bundle can therefore be useful in different mechanosensory systems.

A bundle's state diagram depicts its behavior for different operating points defined by the values of the system's control parameters (16,20). These control parameters include the mechanical loads imposed on individual hair bundles by accessory structures in vivo, such as the tectorial membrane coupled to the bundles of outer hair cells in the mammalian cochlea or the otolithic membrane coupled to hair cells of the utriculus and sacculus. Each structure loads the bundle with a mass, a drag, a stiffness, and an offset force, the combination of which allows a bundle to operate near the type of bifurcation that is suitable for its sensory role.

Although biophysical experiments have identified several of the mechanisms that underlie the active process (15), the noisy environment of a hair bundle complicates the identification of the relevant bifurcations. In particular, noise blurs the boundaries between the dynamical regimes in the bundle's state diagram and conceals the characteristics of various bifurcations. There are several types of bifurcation in which a quiescent system becomes self-oscillatory. In the absence of noise, a system crossing a SNIC or Hopf bifurcation exhibits a continuous rise or discontinuous jump, respectively, in the frequency of spontaneous oscillation (5–7). Changes in the amplitude of oscillation with the adjustment of a parameter further distinguish two types of Hopf bifurcation: a gradual rise in amplitude corresponds to a supercritical Hopf bifurcation and a discontinuous jump signals a subcritical Hopf bifurcation (7). In the presence of noise, however, sharp transitions in the amplitude and frequency of spontaneous oscillation are blunted and become difficult to differentiate from their gradual counterparts, complicating both the localization and identification of bifurcations. We have overcome this challenge by employing a battery of statistical tests to locate and identify bifurcations from experimental observations of a noisy system.

Deterministic bifurcations, which are those defined in the absence of noise, occur at well-specified parameter values. For example, a deterministic system possessing a supercritical Hopf bifurcation is quiescent on one side of the bifurcation and oscillatory on the other. Although the location of this bifurcation can only be estimated from observations, we can nonetheless identify its quiescent and oscillatory sides to define the bifurcation empirically. By analogy with the deterministic case, we defined the location of an empirical bifurcation for a noisy system as the parameter value at which spontaneous oscillations can be reliably detected from observations. The quiescent side of this empirical bifurcation covers the range of parameter values for which oscillations cannot be detected with sufficient statistical certainty. In this manner, we delineated the oscillatory and quiescent regions near supercritical Hopf, subcritical Hopf, and SNIC bifurcations from noisy data.

We explored various metrics that capture the distinguishing features of systems crossing different bifurcations. To do so, we compared simulations of noisy systems near various bifurcations with experimental observations of noisy hair-bundle motion. Based on these comparisons, we ascertained which metrics best characterize the identities and locations of bifurcations near which hair bundles operate. By employing these metrics to assess the behavior of individual hair bundles, we established that a hair bundle can operate near at least two types of bifurcation. We then associated the bundle's operation near these bifurcations with the functions of auditory and vestibular receptor organs. Our methodology not only furthers our understanding of hair-bundle dynamics but also provides a general strategy for analyzing empirical observations of noisy dynamical systems.

MATERIALS AND METHODS

All experiments were performed on spontaneously active hair bundles from the saccular maculae of adult bullfrogs, *Rana catesbeiana* (20).

Supporting Material

We have included detailed Supporting Material to accompany this article. Although the entirety of the document is not required for a general understanding of our findings, we prepared the Supporting Material so that it can serve as a self-contained guide for those who wish to apply our approach to other systems.

Mechanical-load clamp

We employed a feedback system with a real-time interface to control the load stiffness and constant force applied to individual hair bundles (23). Using a glass fiber as a model hair bundle, we confirmed that the clamp achieves this performance with high precision and accuracy (Fig. S1).

For a complete description of the mechanical-load clamp, see Supporting Material Section A.

State-diagram mapping

To calculate the amplitude and frequency of hair-bundle motion in response to various combinations of load stiffness and constant force, we employed both previously described methods (20) and a peak-detection algorithm (24). Operating points for which the bundle's position histogram displayed at least two clear maxima, as signaled by a Hartigans' dip statistic that exceeded 0.01 with $p < 10^{-3}$, were classified as oscillatory (25). All other operating points were deemed quiescent. Hartigans' dip statistic is described in more detail below, and an expanded explanation of the state-diagram calculations can be found in Supporting Material Section B.

Time-series analysis

We employed a battery of statistical tests to assess the behavior of experimentally observed hair bundles and simulated systems. We included simple tests that limited the number of manually selected parameters. Our approach requires only noisy time-series data and does not necessitate stimulation. These features enhance the versatility of the method, permitting its use in systems for which stimulation is difficult or impossible. For a complete description of these metrics, see Supporting Material Section C.

A bifurcation occurs when a system undergoes a qualitative change in behavior. For example, the system may transition from a domain of quiescence to one of spontaneous oscillation. We first sought to estimate the location of a bifurcation by detecting the onset of spontaneous oscillations across a range of control-parameter values. A system that oscillates spontaneously displays a position distribution with more than one peak (20,26,27). Although previous studies measured the distance between peaks in the distribution to describe this phenomenon (27,28), we instead employed Hartigans' dip statistic to measure the modality of a distribution (25). Not only is the dip statistic an inferential measure of modality with an associated p-value, it is also less biased by skew and sample size relative to other metrics (29). Whereas a small value of the dip statistic corresponds to a position distribution with one peak, a large value reflects a distribution that has more than one peak. We therefore defined a position distribution possessing a large value of the dip statistic with a correspondingly small p-value as an indicator of spontaneous oscillation, and a small value of the dip statistic as an indicator of quiescence.

The behavior of a system is typically recorded using only a single observable, such as a bundle's position in time. However, in many instances a system is described by more than one variable and the system's dynamics occupies a space of many variables, called a phase space. A dynamical trajectory in phase space possesses information that is not apparent from a single-variable time series. We therefore wished to reconstruct a two-dimensional phase-space representation of hair-bundle dynamics based only on observations of its displacement. Because many methods for phase-space reconstruction require the manual selection or empirical estimation of several parameter values (30–33), we focused instead on a simpler alternative. The Hilbert transform of a signal is the imaginary part of its analytical representation (34). The joint probability distribution of a bundle's real-valued position and the Hilbert transform of that position—an analytic distribution—is a distribution over a system's phase space that can be calculated without the need for complicated analysis and challenging parameter selection. The analytic distribution appears ring-shaped when a system displays limit-cycle oscillations, which correspond to stable, closed-loop trajectories in phase space. Near quiescent fixed points, the distribution instead exhibits an enhanced, disk-shaped density. This representation is similar to that used to analyze spontaneous otoacoustic emissions (35).

We next estimated the frequency, amplitude, and regularity of spontaneous oscillations by using a peak-detection algorithm that allows the detection in a time series of all peaks and troughs that cross defined thresholds (24). This method permits one to calculate a system's amplitude and frequency of oscillation for time series with substantial noise, short durations, and nonsinusoidal waveforms. For each peak-detection threshold, the frequency is defined as the inverse of the mean time interval between peaks, and the amplitude is calculated as half of the mean difference in position between each peak and trough.

We did not employ spectral methods to determine the location or identity of a bifurcation. In the presence of noise, both a quiescent resonant system and a limit-cycle system exhibit peaks in their Fourier spectra (36). A qualitative change in spectra as this noisy system crosses a bifurcation does not exist. In contrast, a system's position distribution exhibits a qualitative change when the system crosses a bifurcation. Moreover, because many of our signals were subjected to substantial noise and displayed nonsinusoidal waveforms, the Fourier frequency and amplitude of oscillation often fluctuated considerably as the value of a control parameter was changed, and consequently this approach did not yield a clear estimate of a bifurcation's location that was consistent across the systems we studied (Figs. S6–S8). The peak-detection algorithm also performed more reliably than spectral analysis in estimating the amplitude and frequency of noise-induced spikes (Fig. S9).

As a system transitions from a regime dominated by limit-cycle oscillations to one dominated by noise, that system's spontaneous motion becomes more irregular. The distribution of interpeak time intervals, the times between neighboring peaks, correspondingly broadens. We therefore assessed the regularity of a system's oscillations by calculating the coefficient of variation, defined as the ratio of this distribution's standard deviation to its mean. As a system's oscillations become increasingly irregular, the metric grows and thus traces the transition from motion governed by limit-cycle oscillations to that dominated by noise. The regularity of oscillations determined using the coefficient of variation implies that multiple peaks in the position histogram stem from limit-cycle oscillations rather than from noise-induced switching between stable states. For example, a system crossing a saddle-node, or fold, bifurcation may possess a stable state on one side of the bifurcation and two stable states on the other. This system can stochastically switch between two states in the bistable regime. We found that the coefficient of variation for a noisy system transitioning from monostability to bistability is large for all control-parameter values, in contrast with the smaller coefficients of variation displayed by systems displaying limit-cycle oscillations (Fig. S12).

Finally, we estimated the location of a bifurcation using an information-theoretical metric. Upon crossing certain bifurcations, a system exhibits limit-cycle oscillations that appear ring-shaped in that system's analytic distribution. To quantify this phenomenon, we estimated the mutual information between the real and imaginary parts of the system's analytic signal, which we entitle the analytic information. The analytic information resembles the time-delayed mutual information, a nonlinear measure of temporal correlation in a signal (37). As opposed to a shift of the signal in *time*, however, the analytic information is calculated from a real-valued signal and that signal shifted in *phase*. In the presence of a limit cycle the analytic information is large, and in the absence of a cycle its value is small. For example, the analytic information approaches zero for a narrow-band Gaussian-distributed noise sequence as its length increases (Fig. S10). The information increases as a system crosses a bifurcation and begins to oscillate spontaneously. Together with the dip statistic, the analytic information therefore serves as an indicator of the onset of limit-cycle oscillations.

Numerical simulations

A system operating near a bifurcation can be described by the normal form corresponding to the type of bifurcation. The normal form is a standard mathematical expression that captures the generic features of any system operating near that kind of bifurcation. We performed simulations of the normal forms for different bifurcations, in which we included various levels

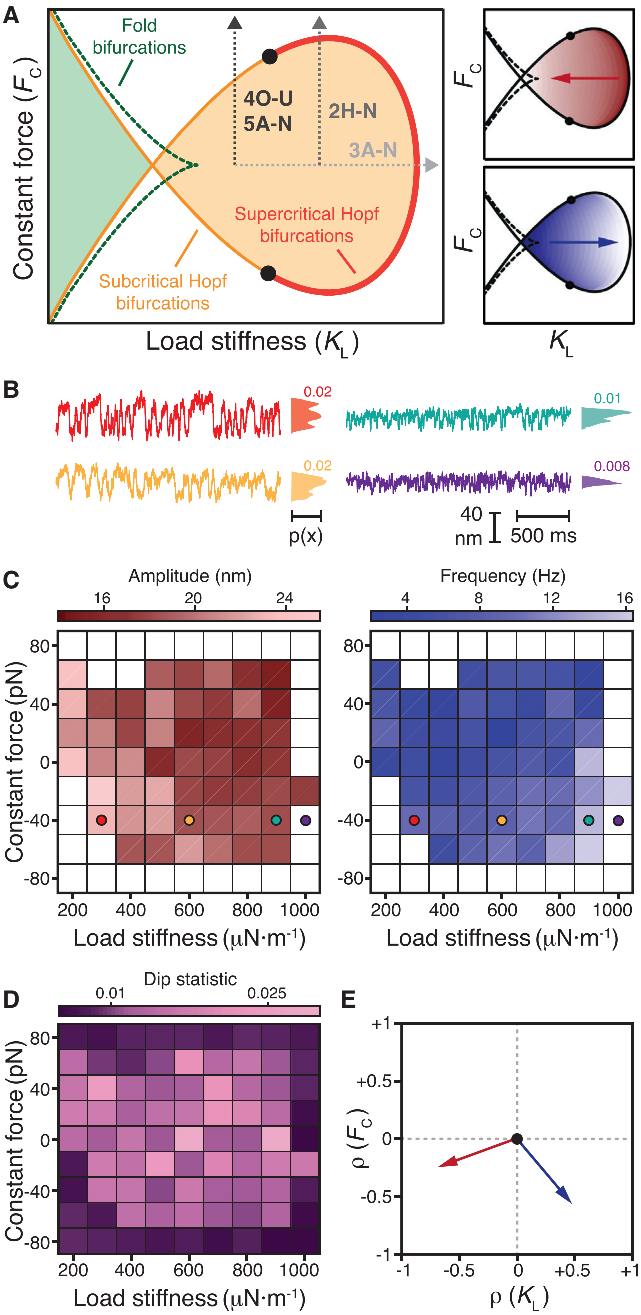

FIGURE 1 Hair-bundle state diagram. (*A*) A theoretical state diagram specifies the behaviors of a hair bundle for various combinations of constant force (F_C) and load stiffness (K_L). A line of Hopf bifurcations (*red*) separates a region within which a hair bundle oscillates spontaneously (*orange*) from one in which the bundle remains quiescent (*white*). Bautin points (*black*) lie at the border between the supercritical and subcritical segments of this line. Within the spontaneously oscillatory region, a bundle's oscillations fall in amplitude and rise in frequency with an increase in load stiffness (*red and blue arrows*, *right panels*). A line of fold bifurcations (*green, dashed*) confines a region within which a bundle exhibits bistability (*light green*). The gray arrows correspond to the regions of the bundle's state diagram explored in Figs. 2, 3, 4, and 5. (*B*) Oscillations of an experimentally observed hair bundle changed in appearance as the load stiffness increased from 300 $\mu N \cdot m^{-1}$ to 1000 $\mu N \cdot m^{-1}$ (*red to purple*). The position histograms and associated dip statistics shown to the right of each trace signal the presence or absence of spontaneous oscillations. The dip statistic quantifies the modality of the system's position histogram; a dip statistic of at least 0.01 with $p < 10^{-3}$ implies spontaneous oscillation. (*C*) An experimental state diagram depicts the behavior of a hair bundle for different values of the load stiffness and constant force. White boxes correspond to operating points at which the bundle's position histogram possessed a dip statistic of <0.01, indicating quiescent behavior. Within the territory of spontaneous oscillation, the intensities of red and blue correspond to the amplitude and frequency, respectively, of the bundle's oscillations calculated with a peak-detection algorithm with a threshold of 25 nm. Colored circles correspond to the traces in (*B*). (*D*) The dip-statistic values for the experimental state diagram in (*C*) are displayed in shades of purple. (*E*) Spearman's rank correlation (ρ) quantifies the relationships between amplitude (*red arrow*) and frequency (*blue arrow*) with the load stiffness ($\rho(K_L)$) and constant force ($\rho(F_C)$) (Table S1). For all experimental data, the stiffness and drag coefficient of the stimulus fiber were $k_{SF} = 109\ \mu N \cdot m^{-1}$ and $\xi_{SF} = 142\ nN \cdot s \cdot m^{-1}$, respectively. The proportional gain of the load clamp was 0.01. For a complete description of the bundle's experimental state diagram, see Supporting Material Section B.

of additive noise for each variable. We simulated the normal forms of the supercritical Hopf, the subcritical Hopf, and the SNIC bifurcations. We also simulated a model of hair-bundle dynamics with additive noise (16). We refer to all these simulations as stochastic simulations throughout this work. All simulations were conducted in MATLAB (R2014a, 8.3.0.532; The MathWorks, Natick, MA) using the Euler-Murayama method.

Because the simulations of the normal forms and the hair-bundle model have no meaningful dimensions in position and time, the results of the simulations are reported without units. In keeping with the convention in the dynamical-systems literature, we orient the abscissa of every plot such that the quiescent regime occurs to the left and the oscillatory regime occurs to the right of each bifurcation. For a complete description of these simulations, see Supporting Material Sections D and E.

RESULTS

The hair bundles of various receptor organs confront a variety of physical loads (15). Both modeling and experiments show that adjusting the mechanical load qualitatively changes a hair bundle's behavior (16,20). Our previous work was limited, however, by the stability and precision of the clamp system used to apply the load on a hair bundle. These limitations impeded determination of the location and identity of bifurcations displayed by a bundle. After improving the mechanical-load clamp to overcome these restrictions (Figs. S1–S3), we were able to probe the nature of bifurcations more systematically than was possible heretofore.

The hair bundle's state diagram

Changing the load stiffness and constant force applied to an individual hair bundle yields a map of the bundle's behavior—a state diagram—for combinations of these two control parameters (Fig. 1 *A*). We predicted earlier that a hair bundle oscillates spontaneously within a region bounded by subcritical and supercritical Hopf bifurcations and exhibits bistability in a regime bounded by lines of fold bifurcations (16). Within the oscillatory regime, we also expect the bundle's spontaneous motion to fall in amplitude and rise in frequency with an increase in load stiffness. In this study, we explored a bundle's behavior within different locales of its state diagram and identified the types of bifurcation near which the bundle could operate.

Using the improved load clamp, we determined the behavior of a bundle as a function of its mechanical load. In agreement with the theoretical expectation, the load stiffness controlled the character of the bundle's spontaneous oscillations (Fig. 1 *B*). When the stiffness was small, the bundle oscillated at low frequency and with a high amplitude, and in some cases exhibited mixed-mode oscillations. Increasing the load stiffness caused the bundle's oscillations to increase in frequency and decrease in amplitude until they vanished altogether.

A spontaneously oscillating hair bundle displays a distribution of positions with more than one peak, whereas the position distribution of a quiescent bundle has only a single peak (20,26,27). We therefore classified the bundle's behavior as either oscillatory or quiescent based on its position histogram. To do so, we employed Hartigans' dip statistic: a large value corresponds to a multimodal position distribution generated by a spontaneously oscillating bundle, and a small value arises from a unimodal position distribution produced by a quiescent bundle (25). This metric revealed an ovoid oscillatory regime surrounded by a domain of quiescence (Figs. 1, *C* and *D*, and S4). The boundary between these two regimes is expected to

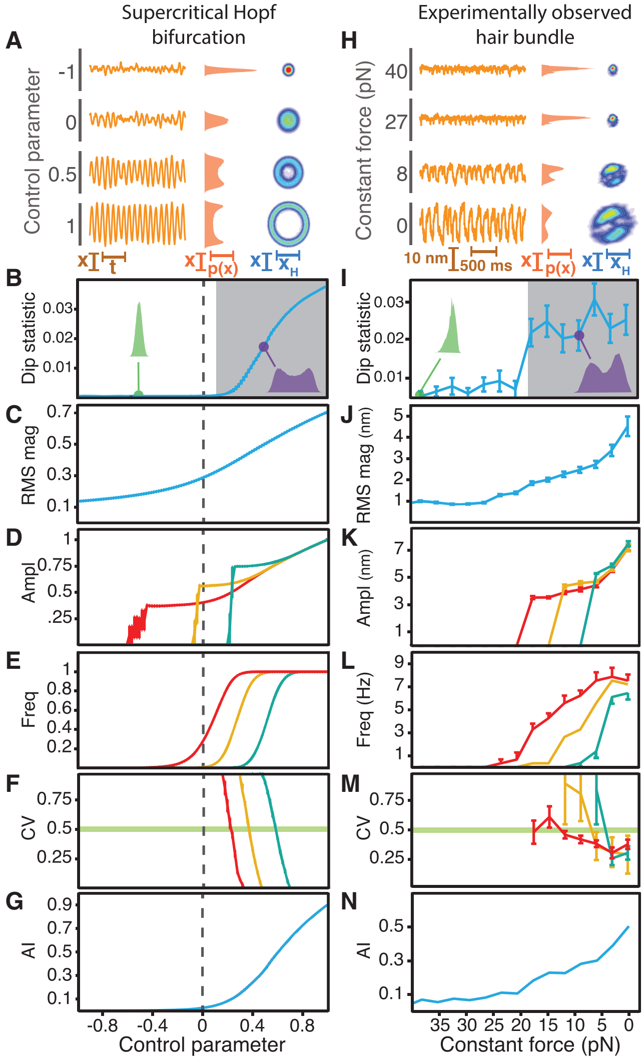

FIGURE 2 Crossing a supercritical Hopf bifurcation by adjusting the constant force. (*A*–*N*) Over a range of parameter values, we compared the behavior near a supercritical Hopf bifurcation with additive noise (*A*–*G*) with that of an experimentally observed hair bundle (*H*–*N*). (*A*) A noisy system operating near a supercritical Hopf bifurcation displayed noise-induced ringing when the control parameter was negative, but oscillated spontaneously for positive values (*left*). When the amplitude of spontaneous oscillation surpassed that of the noise, the position histogram (*middle*) disclosed two peaks. When the control parameter exceeded zero, the joint probability distribution (*right*) for each real-valued position (X) and its Hilbert transform (X_H)—the analytic distribution—was circular, with a diameter that grew with the control parameter. In all of the analytic distributions, red and blue correspond to high and low probability values, respectively. Probabilities of or near zero are displayed in white. (*B*) The dip statistic for the position distribution is shown as a function of the control parameter. A low value for the dip statistic corresponded to a unimodal distribution (*green*). When the control parameter exceeded zero and the amplitude of oscillation exceeded the level of the noise, the position histogram displayed two peaks (*purple*) corresponding to a large value of the dip statistic. The control parameter value at which the dip statistic achieved significance (*shaded*; $p < 10^{-3}$) served as an estimate of the bifurcation's location (*dashed line*). (*C*) The RMS magnitude of the system's motion rose gradually as the control parameter increased. (*D*) The amplitude rose with the control parameter for peak-detection thresholds of 0.68 (*red*), 1.06 (*yellow*), and 1.45 (*cyan*). (*E*) The frequency of oscillation, with the same thresholds as in (*D*), grew with an increase in the control parameter until it achieved a constant value. The value of the control parameter at which the rise in frequency was steepest increased with the threshold. (*F*) The coefficient of variation describes the regularity of oscillation, with a high value corresponding to increased variability in the interpeak time interval. The value of the control parameter at which the coefficient of variation crossed 0.5 increased with the peak-detection threshold. (*G*) The analytic information rose gradually with the control parameter. (*H*) The behavior of an experimentally observed hair bundle was transformed by changes in the constant force: as the force decreased, the amplitude of spontaneous oscillation rose (*left*) and the position histogram became bimodal (*middle*). The analytic distribution formed a loop whose diameter increased with a decrease in the constant force (*right*). (*I*) Reflecting a unimodal position histogram, the dip statistic remained small for large values of the constant force (*green*). When the constant force fell below 20 pN, the position histogram displayed two peaks (*purple*) and the dip statistic increased, defining the boundary of an oscillatory regime (*shaded*; $p < 10^{-3}$). (*J*) The RMS magnitude of the bundle's motion rose gradually as the constant force decreased. (*K*) The amplitude increased as the constant force declined for peak-detection thresholds of 6 nm (*red*), 8 nm (*yellow*), and 10 nm (*cyan*). (*L*) The frequency of oscillation rose gradually with a decrease in constant force until it achieved a constant value near 5 pN. The force at which this rise in frequency occurred depended on the threshold value. (*M*) The coefficient of variation exceeded 0.5 at a value of constant force that decreased as the peak-detection threshold increased. (*N*) The analytic information rose gradually as the constant force fell. For all experimental data, the load stiffness was 400 $\mu\text{N}\cdot\text{m}^{-1}$ with a gain of 0.1. The stiffness and drag coefficient of the stimulus fiber were respectively 109 $\mu\text{N}\cdot\text{m}^{-1}$ and 142 $\text{nN}\cdot\text{s}\cdot\text{m}^{-1}$. All simulations possessed noise with standard deviations of $\sigma_R = \sigma_I = 0.1$. The error bars represent the standard errors of the means.

correspond to lines of subcritical and supercritical Hopf bifurcations (16,20). Improvements in data acquisition and analysis allowed us to construct the experimental state diagram with greater stability and obtain a higher signal/noise ratio over this range of control parameters than was possible heretofore, eliminating the need for additional statistics to delineate the locus of oscillation (20). The frequency of spontaneous oscillation rose and the amplitude fell with an increase in load stiffness. With an increase in the constant force, however, both the amplitude and frequency declined (Fig. 1 *E*). These correlations accord with theoretical predictions and prior experimental investigations of the effects of load stiffness on a bundle's behavior (16,20).

Although the experimental state diagram depicted the boundary of and patterns within a regime of spontaneous oscillation, the identity of the bifurcations that define the boundary has not been determined definitively. Because a bundle's operation near a particular bifurcation can in part dictate its mechanosensory function, we developed a strategy to identify bifurcations in experimental systems with substantial noise.

A supercritical Hopf bifurcation for high-stiffness loads

We first assessed whether a hair bundle in the high-stiffness regime can operate near a supercritical Hopf bifurcation. To do so, we compared simulations of a noisy system crossing a supercritical Hopf bifurcation described by the bifurcation's normal-form equation with experimental observations of a hair bundle subjected to a high load stiffness and increasing values of constant force (Fig. 2). Both the model system and the experimentally observed hair bundle oscillated spontaneously with amplitudes that grew with an increase in the control parameter or a decrease in the bundle's constant force, respectively (Figs. 2, *A* and *H*, and S5 *A*). When the amplitude of oscillation exceeded the noise, the position histogram displayed two distinct peaks. The analytic distribution, a two-dimensional representation of the bundle's motion, formed a loop corresponding to a limit cycle. An increase in the control parameter or a decrease in the bundle's constant force caused the diameter of the loop to grow in concert with a rise in the amplitude of oscillation.

We determined the location of an empirical bifurcation as the point at which the dip statistic assumed a statistically significant value. We estimated that the noisy bifurcation was located on the oscillatory side of a deterministic supercritical Hopf bifurcation (Fig. 2 *B*). For an active hair bundle, we found a sharp transition between small and large values of the dip statistic, corresponding to a bifurcation defining the boundary between a quiescent and an oscillatory regime (Fig. 2 *I*).

Although an oscillatory system's amplitude and frequency of motion are typically calculated from its Fourier transform, the Fourier amplitude and frequency can be uninformative for determining a bifurcation's location when noise is substantial, when the signals are brief, or when oscillations deviate substantially from pure sinusoids. We illustrate this problem with the Fourier transform both for noisy simulations and for experimental observations of hair-bundle motion (Supporting Material Section C.7). For an oscillator operating far from a bifurcation, spectral analysis performs well. Near a bifurcation and in the presence of noise, however, detection of the bifurcation using the Fourier amplitude and frequency becomes difficult. We show that the amplitude and frequency calculated with the Fourier transform fluctuate considerably as a system's control parameter is changed (Fig. S8). Furthermore, spectral methods do not reliably capture the amplitude and frequency for a system that exhibits noise-induced spikes (Fig. S9). Consequently, this method can fail to detect bifurcations in systems dominated by noise.

We therefore characterized the amplitude of spontaneous oscillation using two other metrics. First, we calculated the root-mean-square (RMS) magnitude. For both the simulation and the experimentally observed hair bundle, the RMS magnitude rose gradually as the operating point was moved toward the region of spontaneous oscillation (Fig. 2, *C* and *J*). However, both the amplitude and the frequency of oscillation can affect the RMS magnitude. For example, constant-amplitude spikes that become less frequent correspond to a declining RMS magnitude even though their amplitude does not change. To circumvent this issue, we additionally determined the amplitude of oscillation from a peak-detection algorithm that found the local maxima (peaks) and minima (troughs) separated by a threshold distance. Our peak-detection algorithm accurately estimated the amplitude and frequency of oscillation (Supporting Material Section C.7). We defined the amplitude as half of the average distance between the position of a peak and its neighboring trough. As the control parameter grew or the bundle's constant force shrank, the amplitude rose sharply and then more gradually regardless of the peak-detection threshold (Fig. 2, *D* and *K*). The amplitudes calculated from the peak-detection algorithm were sensitive to the selected peak-detection threshold. For both the simulated and experimentally observed time series, the amplitude curve shifted toward the oscillatory region as the threshold rose.

We then used the same peak-detection algorithm to calculate the frequency of oscillation, which we defined as the inverse of the mean time interval between successive peaks. As noted for the amplitude relations, the frequencies calculated with this method were sensitive to changes in the peak-detection threshold. Increasing the value of the peak-detection threshold shifted the frequency curve farther into the oscillatory side of the bifurcation for both the noisy simulations and the experimental observations (Fig. 2, *E* and *L*).

As a system transitions from a regime dominated by large-amplitude oscillations to one dominated by noise, its spontaneous motion becomes increasingly irregular. We therefore quantified the variability of a system's spontaneous motion by the coefficient of variation for the system's interpeak time intervals: large and small coefficients correspond respectively to irregular and regular oscillations. For all peak-detection thresholds, this metric fell as the systems' operating points moved farther into the oscillatory regime, indicating less variation in the interpeak intervals as the system's motion became dominated by limit-cycle oscillations (Fig. 2, *F* and *M*). As with the amplitude and frequency of motion, the coefficient of variation depended on the peak-detection threshold. Increasing the value of the peak-detection threshold shifted the location at which the coefficient of variation crossed a threshold of 0.5 farther into the oscillatory regime for both a noisy system crossing a supercritical Hopf bifurcation and for an experimentally observed hair bundle.

A noisy bistable or multistable system exhibits a position histogram with more than one peak and consequently a large value for the dip statistic. Therefore, the dip statistic alone cannot distinguish limit-cycle oscillations from noise-induced switching between stable states. However, position fluctuations are much less coherent for bistable and multistable systems than for a limit-cycle oscillator. We can therefore use the coefficient of variation to determine whether a system exhibits limit-cycle behavior or whether it displays noised-induced switching between stable states. The coefficient of variation never falls below 0.5 for a bistable or multistable system, but it can approach zero for a limit-cycle oscillator (Supporting Material Section D.6).

Finally, we sought to pinpoint the location of a bifurcation and to determine its identity with another metric. The analytic information, defined as the mutual information between the real and imaginary parts of the system's analytic signal, approaches zero for normally-distributed noise and grows as limit-cycle oscillations emerge. The analytic information rose gradually with an increase in the control parameter in the simulation and with a decrease in the bundle's constant force in the experiment (Fig. 2, *G* and *N*). Although the gradual rise in the analytic information failed to identify the exact location of a bifurcation, the trends for both the model and experiment displayed a strong similarity. Taken together, the striking agreement between the simulations and experimental observations implies that a hair bundle subjected to a large load stiffness can traverse a supercritical Hopf bifurcation as the constant force is changed.

To confirm that the high-stiffness boundary between the oscillatory and quiescent regions constitutes a line of supercritical Hopf bifurcations, we subjected both a model hair bundle and an experimentally observed one to a constant force of zero and decreasing values of load stiffness, a regime in which the model bundle is known to cross a supercritical Hopf bifurcation. We then employed the same battery of tests as before to assess the similarities between the time series of the simulated and experimentally observed hair bundles (Fig. 3). All panels in Fig. 3 display the same metrics as the corresponding panels in Fig. 2, but for different time series.

In agreement with the generic features of a noisy system crossing a supercritical Hopf bifurcation (Fig. 2 *A*), both the simulated and experimentally observed hair bundles displayed spontaneous oscillations whose amplitude grew with a decrease in stiffness (Figs. 3, *A* and *H*, and S5 *B*). Their analytic distributions also displayed limit cycles that correspondingly increased in diameter. Consistent with that of a noisy system near a supercritical Hopf bifurcation (Fig. 2 *B*), the simulated bundle's position histogram became bimodal on only the oscillatory side of the deterministic bifurcation (Fig. 3 *B*). We observed a clear transition at which the simulated and experimentally observed hair bundles became oscillatory (Fig. 3, *B* and *I*).

Both the RMS magnitude (Fig. 3, *C* and *J*) and the amplitude (Fig. 3, *D* and *K*) of spontaneous oscillation rose gradually with a decrease in stiffness; this pattern accorded with that of a noisy system crossing a supercritical Hopf bifurcation (Fig. 2, *C* and *D*). The frequency of oscillation, however, followed a trend that differed from our simulations of generic dynamics near that bifurcation. As the stiffness decreased from its greatest value, the frequency of oscillation first rose for both the simulated and experimentally observed hair bundles, in agreement with a quiescent system's approach to a supercritical Hopf bifurcation (Fig. 3, *E* and *L*). Further decreases in stiffness, however, caused the frequency to achieve a maximal value and subsequently to decline as the operating point moved beyond the range of influence of the bifurcation. Although this pattern in frequency differs from the generic behavior of a system operating near a supercritical Hopf bifurcation, it accords with the specific behavior predicted for hair-bundle dynamics (Fig. 1 *A*). The coefficient of variation was once again sensitive to changes in the peak-detection threshold, consistent with the generic behavior of a system operating near a supercritical Hopf bifurcation (Fig. 2 *F*). For both the simulated and experimentally observed bundles, the coefficient of variation crossed 0.5 at smaller stiffness values when the value of the peak-detection threshold was larger (Fig. 3, *F* and *M*). Finally, the analytic information rose gradually as the systems' operating points advanced into the oscillatory regime (Fig. 3, *G* and *N*), in agreement with that of a system crossing a supercritical Hopf bifurcation (Fig. 2 *G*).

All of the observations of hair-bundle behavior agreed with stochastic simulations of the normal form of a supercritical Hopf bifurcation and of a model of hair-bundle dynamics. Taken together, these data strongly support the prediction that for an active hair bundle, the boundary of oscillation for large stiffnesses is a line of supercritical Hopf bifurcations (16,20).

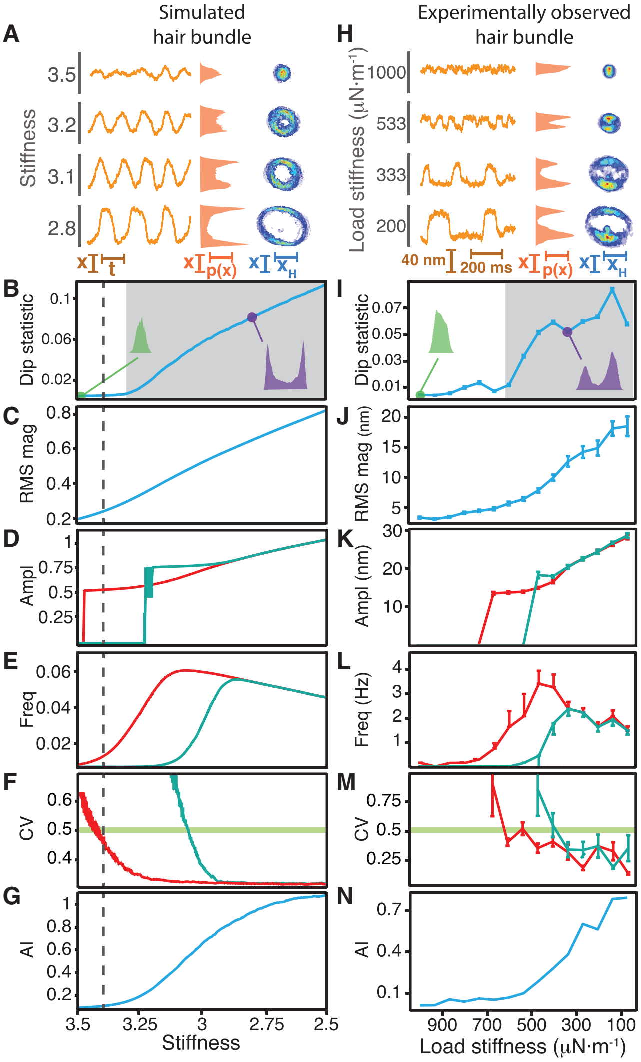

FIGURE 3 Traversing a supercritical Hopf bifurcation by altering the load stiffness. (*A–N*) Over a range of load stiffnesses, we compared the behavior of a model hair bundle crossing a supercritical Hopf bifurcation (*A–G*) with that of an experimentally observed hair bundle (*H–N*). All of the panels depicted here display the same metrics as shown in Fig. 2. (*A* and *H*) As the stiffness declined, the amplitude of spontaneous oscillation rose (*left*), the position histogram became bimodal (*middle*), and the diameter of the limit cycle increased (*right*). (*B* and *I*) The dip statistic rose as the stiffness decreased, signaling the emergence of bimodal position histograms and the onset of spontaneous oscillations (*shaded*; $p < 10^{-3}$). The estimated boundary of the oscillatory regime occurred on the oscillatory side of the deterministic bifurcation (*dashed line*). (*C* and *J*) The RMS magnitude rose gradually as the stiffness decreased. (*D* and *K*) The amplitude increased with a decrease in stiffness. For these and subsequent panels, we used peak-detection thresholds of (*D–F*) 1 (*red*) and 1.5 (*cyan*) or (*K–M*) 26 nm (*red*) and 34 nm (*cyan*). (*E* and *L*) The stiffness at which the frequency rose depended on the value of the peak-detection threshold. Spontaneous oscillations emerged with a frequency that first rose and subsequently fell with decreases in stiffness. (*F* and *M*) The stiffness at which the coefficient of variation exceeded 0.5 depended on the threshold value. (*G* and *N*) The analytic information rose gradually as the stiffness decreased. For all panels, the constant force was zero with a gain of 0.1. The stiffness and drag coefficient of the stimulus fiber were 109 $\mu N \cdot m^{-1}$ and 142 $nN \cdot s \cdot m^{-1}$, respectively. Dashed lines correspond to the location of the supercritical Hopf bifurcation in the absence of noise. Stochastic simulations employed noise with standard deviations of $\sigma_x = \sigma_f = 0.1$. The error bars represent the standard errors of the means.

A subcritical Hopf bifurcation for low-stiffness loads

We predicted that a hair bundle subjected to a small load stiffness operates near a subcritical Hopf bifurcation (Fig. 1 *A*), whereas an alternate analysis suggested that the bundle lies close to a SNIC bifurcation (22,38). To evaluate these alternatives, we used the methodology discussed above to compare experimental observations of a hair bundle subjected to a small load stiffness with those of noisy systems operating near either a subcritical Hopf or a SNIC bifurcation. All panels in Fig. 4 correspond to the metrics displayed in Figs. 2 and 3, but for different sets of simulations and experimental observations.

When operating on the oscillatory side of a subcritical Hopf or SNIC bifurcation, the noisy systems exhibited large-amplitude oscillations (Fig. 4, *A* and *H*) that accorded with those of an experimentally observed hair bundle subjected to a small stiffness (Fig. 4 *O*). On the other side of a subcritical Hopf bifurcation, however, this system displayed noise-induced bursts of high-amplitude oscillations (Fig. 4 *A*). A system near a SNIC bifurcation instead exhibited noise-induced spikes with a frequency that fell with a decrease in the control parameter (Fig. 4 *H*). The bursting behavior near a subcritical Hopf bifurcation occurred when a limit cycle coexisted with a stable point at its center, as evidenced by an analytic distribution possessing an enhanced density within a loop (Figs. 4 *A* and S5 *C*). Fluctuations induced transitions between the stable point and the limit cycle, resulting in bursts of noisy oscillations. Bursting occurred only for parameter values within the region of coexistence that fell between the subcritical Hopf bifurcation and a saddle-node of limit cycles bifurcation. The latter bifurcation, at which a stable and an unstable limit cycle collide and annihilate one another, is a consequence of operation near a subcritical Hopf bifurcation. The spiking behavior exhibited by a system near a SNIC bifurcation, by contrast, engendered a locus of high probability along one part of a cycle (Figs. 4 *H* and S5 *C*). The bundle's spontaneous motion most closely resembled the spiking behavior and analytic distributions of a noisy system proximal to a SNIC bifurcation (Figs. 4 *O* and S5 *C*).

Whereas the dip statistic indicated noisy oscillations solely on the oscillatory side of a deterministic supercritical Hopf bifurcation (Fig. 2 *B*), it evidenced noisy oscillations not only on the deterministically oscillatory side but also within the coexistence region of a deterministic subcritical Hopf bifurcation (Fig. 4 *B*). The dip statistic also detected oscillations on the oscillatory side of a deterministic SNIC bifurcation (Fig. 4 *I*). The dip statistic for an experimentally observed hair bundle clearly delineated the boundary

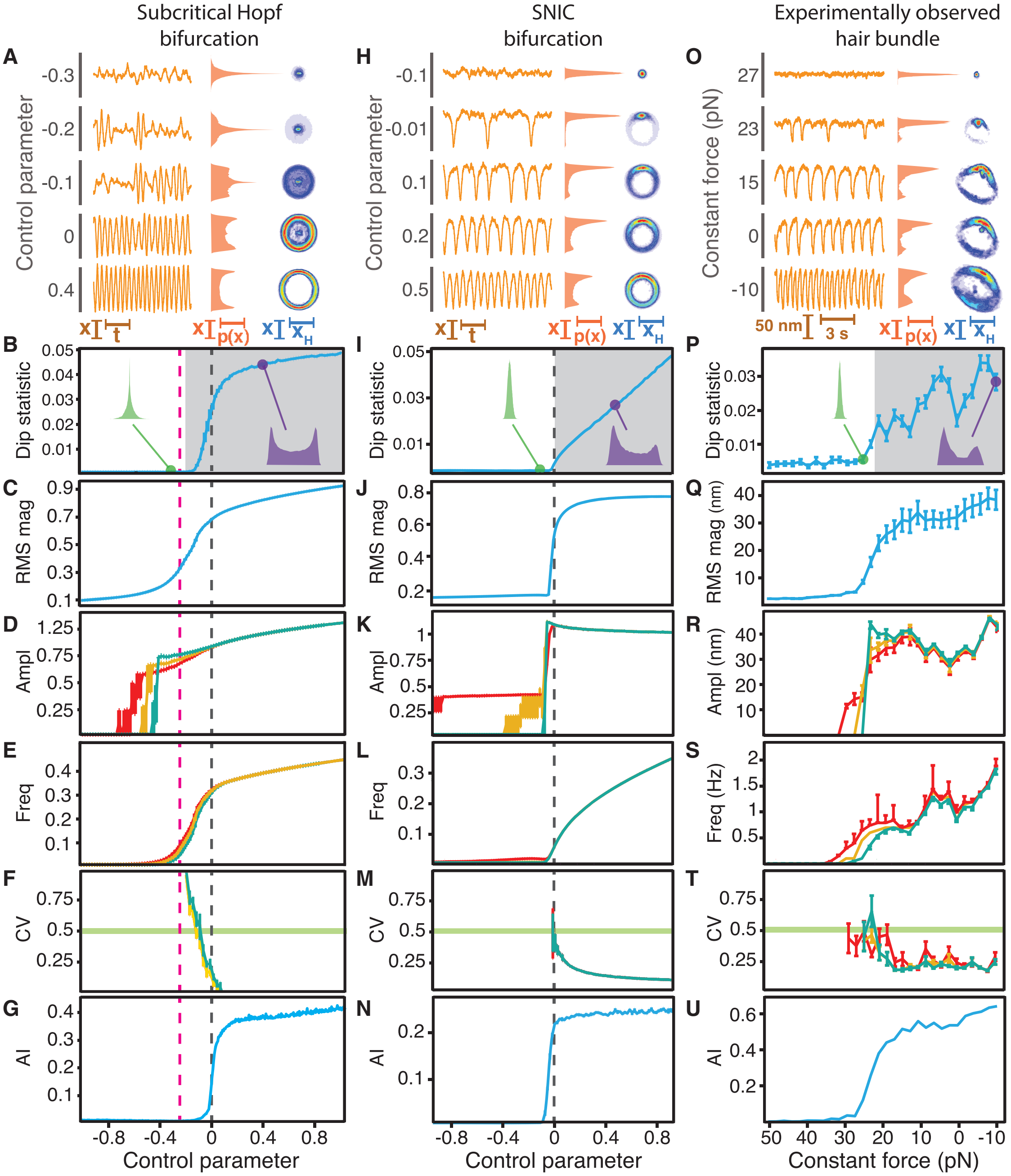

FIGURE 4 A subcritical Hopf or SNIC bifurcation at low stiffness. (*A–U*) We compared the behavior of noisy systems near either a subcritical Hopf bifurcation (*A–G*) or a SNIC bifurcation (*H–N*) with that of an experimentally observed hair bundle subjected to changes in constant force (*O–U*). Each row of panels describes the same metrics as the corresponding rows in Figs. 2 and 3. (*A*) A noisy system poised near a subcritical Hopf bifurcation displayed noise-induced bursts of high-amplitude oscillations when the control parameter fell between -0.25 and 0, a regime in which a limit cycle coexisted with a stable fixed point (*left*). When the control parameter exceeded zero, the system exhibited high-amplitude sinusoidal oscillations. The position histogram featured multiple peaks when the control parameter exceeded -0.25, a regime bounded by a saddle-node of limit cycles and a subcritical Hopf bifurcation (*middle*). The analytic distribution formed a cycle whose diameter changed little with the control parameter and in some cases included a stable region at the center (*right*). (*B*) The dip statistic evidenced the oscillatory boundary within the coexistence region of a subcritical Hopf bifurcation (*shaded*; $p < 10^{-3}$). (*C*) The RMS magnitude grew gradually with the control parameter. (*D*) The amplitude rose abruptly with the control parameter for peak-detection thresholds of 1.2 (*red*), 1.4 (*yellow*), and 1.6 (*cyan*). (*E*) The frequency of oscillation rose briskly between the saddle-node of limit cycles and the subcritical Hopf bifurcation and then gradually on the exclusively oscillatory side of the Hopf bifurcation. (*F*) The coefficient of variation was insensitive to changes in the peak-detection threshold. (*G*) The analytic information rose sharply near the subcritical Hopf bifurcation. (*H*) A system poised near a SNIC bifurcation displayed large-amplitude spikes that increased in frequency with a rising control parameter (*left*). In agreement with this behavior, the position histograms became increasingly bimodal (*middle*). The analytic distribution disclosed a cycle whose diameter remained invariant to changes in the control parameter (*right*). Consistent with its spiking behavior, the system dwelled more often along one part of the cycle for low values of the control parameter. (*I*) The dip statistic determined

(legend continued on next page)

between a quiescent regime and an oscillatory one, again demonstrating the utility of this metric in pinpointing a bifurcation's location (Fig. 4 *P*).

All of the other metrics were qualitatively indistinguishable between noisy systems operating near a subcritical Hopf or a SNIC bifurcation, with the behaviors of both systems resembling those of an experimentally observed hair bundle subjected to a low stiffness. However, these behaviors were distinct from those of a system close to a supercritical Hopf bifurcation (Figs. 2 and 3). In all cases, the RMS magnitude increased abruptly near a bifurcation (Fig. 4, *C*, *J*, and *Q*). The amplitude rose suddenly before a bifurcation and then grew gradually or remained constant (Fig. 4, *D*, *K*, and *R*). Unlike the pattern of a system operating near a supercritical Hopf bifurcation, the rise in the frequency of spontaneous oscillation and the fall in the coefficient of variation with an increase in control parameter were insensitive to the value of the peak-detection threshold (Fig. 4, *E*, *F*, *L*, *M*, *S*, and *T*). Finally, the analytic information rose abruptly near the bifurcation (Fig. 4, *G*, *N*, and *U*), in contrast to the gradual rise displayed by a system near a supercritical Hopf bifurcation (Fig. 2 *G*). Together, these data demonstrate that for a low stiffness, a hair bundle can cross a subcritical Hopf or SNIC bifurcation, but not a supercritical Hopf bifurcation.

We next assessed whether the bursting behavior of a system near a subcritical Hopf bifurcation disqualifies this bifurcation as that exhibited by observed hair bundles at low stiffnesses. Using the same battery of tests, we compared experimental observations of another hair bundle with stochastic simulations of a model bundle that is known to operate near a subcritical Hopf bifurcation (Figs. 1 *A* and 5). In the presence of noise, the simulated bundle exhibited downward excursions resembling the spikes displayed by both of the experimentally observed bundles at low stiffnesses (Figs. 4 *O*, 5, *A* and *H*, and S5 *D*). Unlike a system displaying bursting near a subcritical Hopf bifurcation (Fig. 4 *A*), the simulated bundle showed noise-induced spikes well beyond the saddle-node of limit cycles bifurcation (Fig. 5 *A*). The bundle displayed a graded frequency response: the spiking frequency fell with an increase in the bundle's constant force. This change was accompanied by a locus of increasing probability in the analytic distribution that rested upon one part of a large-amplitude limit cycle. Spikes may therefore result either from the asymmetric dynamics associated with a SNIC bifurcation or from the specific asymmetry captured by the hair-bundle model near a subcritical Hopf bifurcation, but lacking in the normal form of a subcritical Hopf bifurcation. All metrics showed a strong qualitative agreement between the model bundle operating near a subcritical Hopf bifurcation, a SNIC bifurcation, and both experimentally observed hair bundles (Figs. 4 and 5). The changes in the metrics with a control parameter were once again distinct from those of a noisy system traversing a supercritical Hopf bifurcation.

DISCUSSION

A hair bundle's function can be dictated in part by its operation near a particular bifurcation. Here, we identified the types and locations of bifurcations from experimental observations of noisy hair bundles. By employing several metrics to compare models with experimental observations, we analyzed the bifurcation structure of experimentally observed hair bundles operating in a noisy environment and confirmed the predictions of a qualitative model of hair-bundle dynamics.

Our model makes no assumptions about the temporal or spatial scales of a bundle's dynamics and requires only two properties of hair bundles: their nonlinear stiffness and adaptation to stimulation (15,39–42). Any actual bundle or hair-bundle model that possesses these features will exhibit the same state diagram as our model and thus show qualitatively similar responses to stimulation (16). Moreover, we previously used a quantitative model of hair-bundle mechanics with physical parameters plausible for the mammalian cochlea to demonstrate that hair-bundle activity is likely essential for the mammalian auditory system to achieve great sensitivity and sharp frequency selectivity in response to high-frequency periodic stimuli (43).

Guided by the qualitative model, we found that a single hair bundle can operate near more than one type of

---

the location of the deterministic SNIC bifurcation (*shaded*; $p < 10^{-3}$). (*J*) The RMS magnitude grew rapidly to a constant value near the SNIC bifurcation. (*K*) The amplitude remained constant on the oscillatory side of the SNIC bifurcation for thresholds of 0.7 (*red*), 0.9 (*yellow*), and 1.1 (*cyan*). (*L*) The frequency of oscillation rose gradually from zero near the SNIC bifurcation for all peak-detection thresholds. (*M*) The coefficient of variation was insensitive to the peak-detection threshold near the SNIC bifurcation. (*N*) The analytic information reached a plateau for positive values of the control parameter. (*O*) As the constant force decreased, the spontaneous oscillations of an experimentally observed hair bundle resembled spikes of rising frequency (*left*), the position histograms became increasingly bimodal (*middle*), and the analytic distributions formed loops that changed little in diameter with a locus of greater probability along one section of each cycle (*right*). (*P*) The dip statistic located the boundary of the spontaneously oscillatory region (*shaded*; $p < 10^{-3}$). (*Q*) The bundle's RMS magnitude rose abruptly to a nearly constant value near the oscillatory boundary. (*R*) The amplitude remained nearly constant for constant forces below 25 pN for peak-detection thresholds of 20 nm (*red*), 27.5 nm (*yellow*), and 35 nm (*cyan*). (*S*) The bundle's frequency of spontaneous oscillation rose gradually from zero for constant forces below 30–35 pN. (*T*) The coefficient of variation remained insensitive to changes in threshold. (*U*) The analytic information rose sharply and then gradually as the constant force decreased. For all experimental data, the load stiffness was 50 $\mu\mathrm{N}\cdot\mathrm{m}^{-1}$ with a gain of 0.1. The stiffness and drag coefficient of the stimulus fiber were 139 $\mu\mathrm{N}\cdot\mathrm{m}^{-1}$ and 239 $\mathrm{nN}\cdot\mathrm{s}\cdot\mathrm{m}^{-1}$, respectively. Black dashed lines in (*B*–*G*) and (*I*–*N*) correspond to the locations of a subcritical Hopf bifurcation and a SNIC bifurcation, respectively. Pink dashed lines depict the location of a saddle-node of limit cycles bifurcation. Stochastic simulations for a subcritical Hopf bifurcation and for a SNIC bifurcation possessed noise levels of $\sigma_R = \sigma_I = 0.2$. The error bars represent the standard errors of the means.

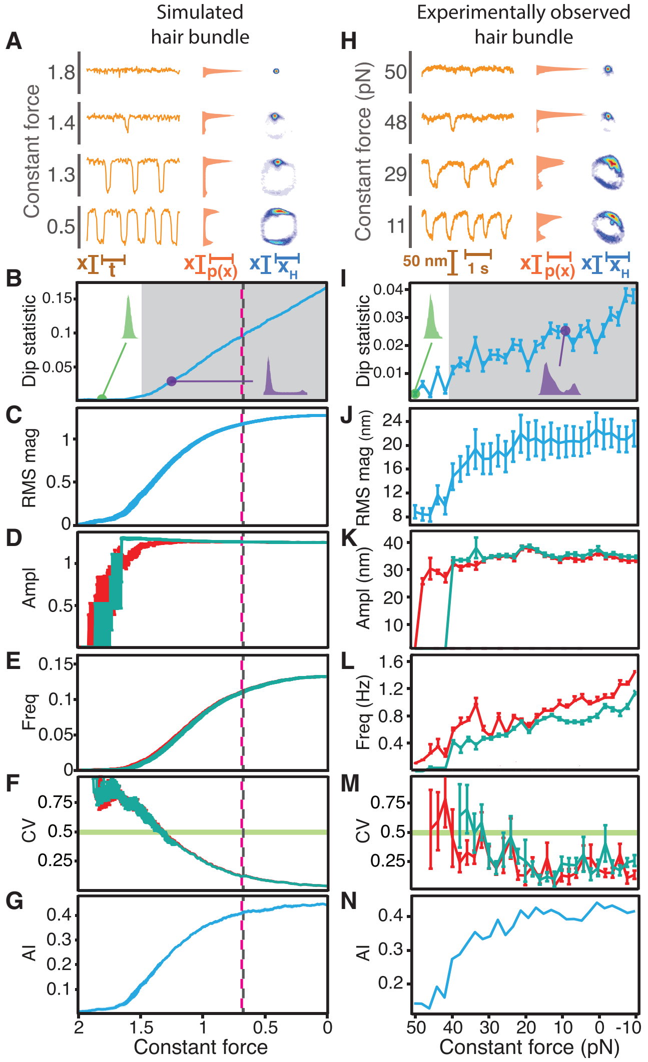

FIGURE 5 A subcritical Hopf bifurcation can be crossed by controlling the constant force. When the load stiffness remains low, a decrease in constant force advances a bundle's operating point across a subcritical Hopf bifurcation. (*A–N*) Stochastic simulations of a model of hair-bundle motility (*A–G*) were compared with an experimentally observed hair bundle (*H–N*). The results depicted here correspond to the same metrics displayed in Figs. 2, 3, and 4. (*A*) As the constant force decreased, a model bundle exhibited noise-induced spikes of rising frequency (*left*), an increasingly bimodal position histogram (*middle*), and an analytic distribution with a cycle whose diameter changed little over a range of forces and upon which rested a locus of higher probability (*right*). (*B*) The dip statistic defined an oscillatory boundary at a control parameter smaller than the control parameters corresponding to the deterministic bifurcations (*shaded*; $p < 10^{-3}$). (*C*) The model bundle's RMS magnitude rose to a nearly constant value as the constant force decreased. (*D*) Calculated with thresholds of 1 (*red*) and 2 (*cyan*), the amplitude of the bundle's motion remained constant for forces below 1. (*E*) The frequency of oscillation for a model bundle rose smoothly from zero as the constant force decreased for both peak-detection thresholds. (*F*) The coefficient of variation remained insensitive to changes in the peak-detection threshold. (*G*) The analytic information rose with a decrease in constant force. (*H*) An experimentally observed hair bundle exhibited behaviors that accorded with those of a model bundle crossing a subcritical Hopf bifurcation in the presence of noise. As the constant force declined, the bundle displayed spikes of increasing frequency (*left*), a more clearly bimodal position histogram (*middle*), and an analytic distribution with a cycle that changed little in diameter over a range of forces and upon which rested a locus of enhanced probability (*right*). (*I*) The dip statistic defined the boundary of the oscillatory region (*shaded*; $p < 10^{-3}$). (*J*) The RMS magnitude of the bundle's motion rose as the constant force fell below 40–45 pN and achieved a constant value for forces below 35 pN. (*K*) The amplitude of the bundle's oscillations achieved a nearly constant value for forces below 35–48 pN. We employed peak-detection thresholds of 50 nm (*red*) and 60 nm (*cyan*). (*L*) The bundle's frequency of oscillation rose gradually from zero as the constant force decreased. (*M*) The constant force at which the coefficient of variation exceeded 0.5 remained relatively insensitive to changes in the peak-detection threshold. (*N*) The analytic information rose as the constant force decreased. For experimental data, the load stiffness was 100 $\mu N \cdot m^{-1}$ with a gain of 0.1. The stiffness and drag coefficient of the stimulus fiber were 139 $\mu N \cdot m^{-1}$ and 239 $nN \cdot s \cdot m^{-1}$, respectively. Black dashed lines correspond to the location of the subcritical Hopf bifurcation at $F_C = 0.66$, and pink dashed lines correspond to the location of the saddle-node of limit cycles bifurcation at $F_C = 0.664$ in the absence of noise. Stochastic simulations of the model of hair-bundle motility possessed a stiffness of 2 and noise levels of $\sigma_x = \sigma_f = 0.2$. The error bars represent standard errors of the means.

bifurcation depending on its mechanical load. Although it can be argued that noise introduces new bifurcations and changes the character of existing ones (44), our observations accord well with simulations of systems crossing bifurcations in the presence of noise.

Proximity to a bifurcation

To understand certain dynamical systems, one must determine whether they can operate near bifurcations. We employed a battery of quantitative metrics to isolate the location of such bifurcations as a function of a control parameter. Among these metrics, Hartigans' dip statistic offered multiple advantages when used to determine the modality of a bundle's position distribution. First, the dip statistic is an inferential metric that provides an associated *p*-value that allowed us to estimate the bifurcation's position consistently across all of the data sets. Second, the dip statistic is less sensitive to sample size and skew than other measures of a distribution's modality (29).

A phenomenological bifurcation occurs when the probability distribution of a system's state, including but not limited to its position distribution, exhibits a qualitative change; for example, the distribution's modality may change (44). A third benefit of using the dip statistic is that it identifies phenomenological bifurcations associated with changes in the position distribution. Although this approach might have missed modality changes in the bundle's state distribution associated with unobserved variables, such as the hair cell's transduction current, it clearly defined a boundary between an oscillatory and a quiescent regime based only on experimental observations of the bundle's motion. Although we found that noise introduced an unavoidable bias in the estimation of a deterministic bifurcation's position, we note that phenomenological bifurcations can occur at values of a control parameter that differ from those in the deterministic cases.

The coefficient of variation for the values of a system's state variables in a time series was previously employed to experimentally estimate the locations of Hopf bifurcations in a predator-prey system, in which the bifurcation's location was defined by the transition from a small to a large value of the coefficient corresponding to the onset of spontaneous oscillations (45). By using the magnitude of the state variables rather than the time intervals between events, this coefficient of variation captures a different aspect of a dynamical system's behavior than the coefficient of variation we employ here. Because the coefficient of variation for the values of a system's state variables does not describe the regularity of a system's oscillations or spiking, it cannot distinguish between noisy switching in a bistable system and limit-cycle oscillations. The mean value of the variables we study is often zero, as is the case for the Hopf normal form, so it is not possible to calculate this coefficient of variation. Moreover, a change in this metric with a control parameter could arise from a change in a variable's mean value rather than from a system crossing a Hopf bifurcation. Nonetheless, this metric will likely be useful for bifurcation analysis of some systems, especially if it is combined with some of the other measures that we utilize here.

Identity of a bifurcation

We developed a protocol that permits the identification of bifurcations solely on the basis of noisy time series. This diagnostic method has several appealing features. Although the approach requires data from a range of operating points near a bifurcation, it does not necessitate external stimulation. In studies of climate change, finance, and geophysics (3,4), among other disciplines, stimulation may be difficult or even impossible. Moreover, the method performs well at high noise levels and relies on few (if any) choices by the experimenter.

Although the dip statistic can be employed to locate a bifurcation, it cannot be used to distinguish between types of bifurcation. To identify the bifurcation near which a system operates, we apply five additional metrics, each of which captures a different feature of the system's behavior (Fig. 6). These metrics and the analytical distributions allow us to distinguish supercritical Hopf bifurcations from subcritical Hopf and SNIC bifurcations. Near a supercritical Hopf bifurcation, the RMS magnitude grows more slowly with the control parameter, and the oscillation frequency and coefficient of variation are more dependent on the peak-detection threshold, than near subcritical Hopf and SNIC bifurcations. In addition, the analytical distribution often evidences a fixed point surrounded by a limit cycle when a bundle operates near a subcritical Hopf bifurcation, but never does so near a supercritical Hopf bifurcation. The similarities between simulations and observations allow us to conclude that a hair bundle possess a line of supercritical Hopf bifurcations in the high-stiffness regime.

The agreement between the metrics for simulations and observations also implies that a hair bundle manifests lines of either subcritical Hopf or SNIC bifurcations at low stiffnesses. Experimentally observed bundles exhibit the graded response in the frequency of spiking that occurs near a SNIC bifurcation, but not near a subcritical Hopf bifurcation. However, a model bundle near a subcritical Hopf bifurcation in the presence of noise also exhibits a graded spike-frequency response resembling that of a SNIC bifurcation (21,22), even though no SNIC bifurcation occurs in this region of the state diagram (16).

Graded spiking responses can arise from fluctuations inducing a system to cross a threshold. Moving a control parameter in a specific direction can increase the probability of crossing the threshold and consequently elevate the

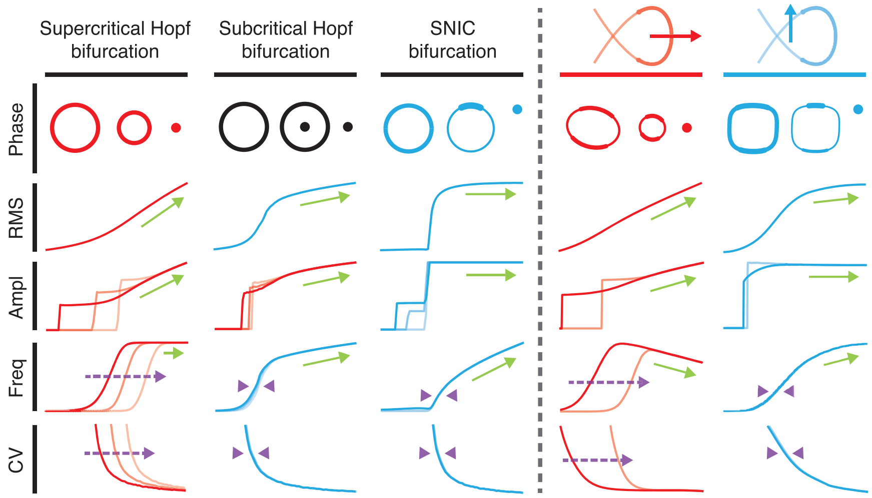

FIGURE 6 Summary of the metrics used to identify bifurcations. We present a schematic diagram for each metric that was used to identify the type of the bifurcation near which a system operated. The three columns on the left include diagrams for noisy systems crossing supercritical Hopf, subcritical Hopf, and SNIC bifurcations. The two columns on the right refer to a model hair bundle crossing either a supercritical (*red*) or subcritical (*blue*) Hopf bifurcation. Red and blue arrows highlight the range of parameter values explored in each instance. Green arrows indicate trends in each of the statistics as a function of the control parameter. Purple arrows and purple arrowheads illustrate the dependence and independence, respectively, of the frequency of oscillation and coefficient of variation with changes in peak-detection threshold. In each panel, we highlight in color the metrics that agree with observations of bundles subjected to high-stiffness (*red*) and low-stiffness (*blue*) loads.

spiking frequency. Near a SNIC bifurcation, noise can cause a system to repeatedly cross a threshold and produce a spike. When operating in the low-stiffness regime, the model bundle instead possesses a quasi-threshold within the quiescent region near a subcritical Hopf bifurcation (Figs. S15–S18). In contrast to a true threshold that separates sub- and suprathreshold regimes, a quasi-threshold constitutes a region over which the model bundle can display spikes of all amplitudes (10). Noise can induce the model bundle's trajectory to cross this quasi-threshold, which can be very narrow, eliciting an excursion resembling an all-or-none spike. Increasing the stiffness diminishes both the amplitude of spikes and the range of constant forces over which spikes can occur. These noise-induced excursions are similar to the voltage spikes or action potentials produced by neurons (6,7,46). For example, the Hodgkin-Huxley model possesses a quasi-threshold, as does the FitzHugh-Nagumo model, a two-dimensional simplification of the Hodgkin-Huxley model that is similar in form to our qualitative hair-bundle model (16,46,47). In the presence of noise, the FitzHugh-Nagumo model exhibits noise-induced spikes with a frequency that depends on a control parameter. Although the graded-frequency spiking present in class I excitable neurons has typically been described by operation near a SNIC bifurcation (6,7,9), similar behavior can arise instead from model-specific dynamics near a subcritical Hopf bifurcation. Therefore, some behaviors do not result solely from operation near a bifurcation, but are specific to the system in question. The presence of a graded frequency response is not sufficient to conclude that a system operates near a SNIC bifurcation.

The appearance of large-amplitude oscillations as the constant force is changed is consistent with a hair bundle crossing either a subcritical Hopf or SNIC bifurcation. Alternatively, the emergence of large oscillations could arise from a third mechanism. Here, a small-amplitude limit cycle is created at a supercritical Hopf bifurcation, but the amplitude of the cycle grows rapidly within an exponentially small range of control-parameter values, resulting in a large-amplitude limit cycle. This phenomenon, termed a canard explosion, has been observed in a model of hair-bundle motility over a limited range of operating points (48,49). Although canard explosions can in principle emerge in our model, it is unlikely that we observed this phenomenon in experiments. A canard explosion emerges as a sharp rise in the amplitude of oscillation with a corresponding decrease in frequency (50). In contrast, we found that large bundle oscillations appeared with a corresponding increase in frequency as the constant force declined.

Although we could not reliably distinguish a noisy system operating near a SNIC bifurcation from one poised close to a subcritical Hopf bifurcation, one could in principle discriminate between these bifurcations by assessing their phase portraits. The phase portrait of a system operating in the region of coexistence between a limit cycle and a fixed point near a subcritical Hopf bifurcation evidences a stable fixed point within a stable limit cycle. The phase portrait of a system near a SNIC bifurcation does not illustrate such coexistence. Using the analytic distributions as a proxy for the bundle's phase portraits, we at times found a region of increased probability within a loop, as would be expected for a stable fixed point within a limit cycle (Supporting Material Section F.2). Although we require additional data to confirm that the bundle operates in a coexistence region, these results indicate that a bundle subjected to a small load stiffness is more likely to operate close to a subcritical Hopf bifurcation than to a SNIC bifurcation.

Because a single model explains the behavior of bundles for both large and small values of load stiffness as arising in part from operation near supercritical and subcritical Hopf bifurcations, respectively, it is more likely that a bundle experiences subcritical Hopf rather than SNIC bifurcations. Taken together, these data indicate a clear distinction between a bundle's operation near a supercritical Hopf bifurcation at high stiffness values and its operation close to a subcritical Hopf bifurcation at low stiffnesses.

Hair-bundle function

Systems operating near different bifurcations exhibit distinct behaviors. Both the proximity to a bifurcation and the type of bifurcation can determine how a system responds to different classes of stimuli. For example, a system poised near a supercritical Hopf bifurcation responds well to periodic stimuli, whereas one operating near a SNIC bifurcation can exhibit a graded frequency response in response to changes in its control parameter. Dynamical-systems analysis therefore reveals how a system might possess different functions within different regions of its state diagram. By noting where bifurcations lie in the state diagram, one can predict how that system might function in various contexts.

The stiffness of a hair bundle's load in vivo depends on the sensory organ in which it resides. For example, a mammalian auditory hair bundle tuned to 14 kHz might experience a stiffness load by the tectorial membrane of $>200\ \mathrm{mN \cdot m^{-1}}$ (43), whereas many vestibular hair bundles are coupled to otolithic membranes with a much smaller stiffness of $\sim 1\ \mathrm{mN \cdot m^{-1}}$ (51). A bundle's load stiffness might therefore determine its sensory role.

When an auditory receptor organ imposes a high stiffness on a hair bundle, the bundle operates in the vicinity of a supercritical Hopf bifurcation. Under these conditions, the bundle responds to periodic stimuli with robust amplification, sharp frequency selectivity, and a broad dynamic range (20,52,53). If a bundle is instead coupled to a load of low stiffness, as might be the case in a vestibular organ, it operates in the vicinity of a subcritical Hopf bifurcation. Thermal fluctuations can induce spikes that permit the bundle to represent changes in constant force as changes in spike frequency. This graded frequency response could be useful for the detection of accelerations and gravistatic forces. For operating points in the same region of a bundle's state diagram, a bundle can also spike in response to the beginning or end of a force step, and thus can serve as a step detector owing to the quasi-threshold behavior that allows it to detect abrupt changes in force (16,20).

The dual sensory roles of individual hair bundles might be mirrored by different subpopulations of the afferent neurons that innervate them. Within vestibular organs such as the sacculus and utriculus, hair cells are innervated by afferents that discharge regularly or irregularly in the absence of stimulation (54). These neurons are classified according to their distribution of interpeak time intervals: regular and irregular afferents possess distributions with small and large coefficients of variation, respectively. Regular afferents generate action potentials with a frequency that depends on the magnitude of a constant injected current (55), a behavior resembling that of a noisy hair bundle subjected to a low stiffness. Irregular afferents, on the other hand, respond better to periodic stimuli and display spike rates that change little with the injected current (56), similar to the behavior of an oscillating hair bundle operating in the high-stiffness regime in response to changes in constant force. Whether these neuronal subpopulations operate in the vicinity of subcritical or supercritical Hopf bifurcations, respectively, remains to be seen. For example, as the firing rate of a regular afferent neuron decreases, its coefficient of variation correspondingly increases (55,57). We observe the same negative correlation between the frequency and coefficient of variation as a system crosses a bifurcation, indicating that the afferent neurons might also cross a bifurcation as their control parameter is changed. The algorithms presented here may permit identification of the bifurcations near which the neurons operate. Furthermore, it remains uncertain whether these two neuronal subpopulations selectively innervate hair cells with bundles operating within different functional regimes, and whether afferent neurons in the auditory system possess traits similar to those of bundles operating in the high-stiffness regime.

In summary, one sensory function—the detection of periodic stimuli—arises from a hair bundle's operation near a supercritical Hopf bifurcation. Two other sensory functions—the measurement of constant forces and the detection of force steps—result from a bundle's operation within the quiescent region near a subcritical Hopf bifurcation. These results highlight the remarkable flexibility of the hair bundle as a signal detector and suggest how the bundle might have evolved through changes in its operating point to serve disparate functions in various auditory, vestibular, and lateral-line organs.

SUPPORTING MATERIAL

Supporting Materials and Methods, 18 figures, and one table are available at http://www.biophysj.org/biophysj/supplemental/S0006-3495(16)30596-3.

AUTHOR CONTRIBUTIONS

J.D.S., D.Ó M., and A.J.H. designed the experiments, analyzed the data, and wrote the manuscript. J.D.S. performed the experiments and the simulations.

ACKNOWLEDGMENTS

We thank B. Fabella for his technical expertise and the members of our research group for comments on the manuscript.

J.D.S. is supported by grants F30DC013468 and T32GM07739 from the National Institutes of Health. A.J.H. is an Investigator of the Howard Hughes Medical Institute.

REFERENCES

1. Strogatz, S. 2005. Nonlinear Dynamics and Chaos. Westview Press, Boulder, CO.
2. Hudspeth, A. J., F. Jülicher, and P. Martin. 2010. A critique of the critical cochlea: Hopf—a bifurcation—is better than none. *J. Neurophysiol.* 104:1219–1229.
3. Dijkstra, H. A. 2013. Nonlinear Climate Dynamics. Cambridge University Press, Cambridge.
4. Scheffer, M., J. Bascompte, …, G. Sugihara. 2009. Early-warning signals for critical transitions. *Nature.* 461:53–59.
5. Kuznetsov, Y. A. 2013. Elements of Applied Bifurcation Theory. Springer Science & Business Media, Berlin.
6. Rinzel, J., and G. B. Ermentrout. 1989. Analysis of neural excitability and oscillations. *In* Methods in Neuronal Modeling. C. Koch and I. Segev, editors. MIT Press, Cambridge, MA.
7. Izhikevich, E. M. 2000. Neural excitability, spiking and bursting. *Int. J. Bifurcat. Chaos.*.
8. Hodgkin, A. L. 1948. The local electric changes associated with repetitive action in a non-medullated axon. *J. Physiol.* 107:165–181.
9. Izhikevich, E. M. 1999. Class 1 neural excitability, conventional synapses, weakly connected networks, and mathematical foundations of pulse-coupled models. *IEEE Trans. Neural Netw.* 10:499–507.
10. Izhikevich, E. M. 2007. Dynamical Systems in Neuroscience. MIT Press, Cambridge, MA.
11. Nadrowski, B., P. Martin, and F. Jülicher. 2004. Active hair-bundle motility harnesses noise to operate near an optimum of mechanosensitivity. *Proc. Natl. Acad. Sci. USA.* 101:12195–12200.
12. Rhode, W. S. 2007. Basilar membrane mechanics in the 6-9 kHz region of sensitive chinchilla cochleae. *J. Acoust. Soc. Am.* 121:2792–2804.
13. Dalhoff, E., D. Turcanu, …, A. W. Gummer. 2007. Distortion product otoacoustic emissions measured as vibration on the eardrum of human subjects. *Proc. Natl. Acad. Sci. USA.* 104:1546–1551.
14. de Vries, H. L. 1952. Brownian motion and the transmission of energy in the cochlea. *J. Acoust. Soc. Am.* 24:527.
15. Hudspeth, A. J. 2014. Integrating the active process of hair cells with cochlear function. *Nat. Rev. Neurosci.* 15:600–614.
16. Ó Maoiléidigh, D., E. M. Nicola, and A. J. Hudspeth. 2012. The diverse effects of mechanical loading on active hair bundles. *Proc. Natl. Acad. Sci. USA.* 109:1943–1948.
17. Eguíluz, V. M., M. Ospeck, …, M. O. Magnasco. 2000. Essential nonlinearities in hearing. *Phys. Rev. Lett.* 84:5232–5235.
18. Choe, Y., M. O. Magnasco, and A. J. Hudspeth. 1998. A model for amplification of hair-bundle motion by cyclical binding of Ca2+ to mechanoelectrical-transduction channels. *Proc. Natl. Acad. Sci. USA.* 95:15321–15326.

19. Camalet, S., T. Duke, …, J. Prost. 2000. Auditory sensitivity provided by self-tuned critical oscillations of hair cells. *Proc. Natl. Acad. Sci. USA*. 97:3183–3188.

20. Salvi, J. D., D. Ó Maoiléidigh, …, A. J. Hudspeth. 2015. Control of a hair bundle's mechanosensory function by its mechanical load. *Proc. Natl. Acad. Sci. USA*. 112:E1000–E1009.

21. Fredrickson-Hemsing, L., C. E. Strimbu, …, D. Bozovic. 2012. Dynamics of freely oscillating and coupled hair cell bundles under mechanical deflection. *Biophys. J.* 102:1785–1792.

22. Shlomovitz, R., L. Fredrickson-Hemsing, …, D. Bozovic. 2013. Low frequency entrainment of oscillatory bursts in hair cells. *Biophys. J.* 104:1661–1669.

23. Salvi, J. D., D. Ó Maoiléidigh, …, A. J. Hudspeth. 2015. Characterization of active hair-bundle motility by a mechanical-load clamp. *AIP Conf. Proc.* 1703:030005.

24. Jacobson, M. L. 2001. Auto-threshold peak detection in physiological signals. *Proc. 23rd Annu. Int. Conf. IEEE.* Vol. 3.

25. Hartigan, J. A., and P. M. Hartigan. 1985. The dip test of unimodality. *Ann. Stat.* 13:70–84.

26. Bialek, W., and H. P. Wit. 1984. Quantum limits to oscillator stability: theory and experiments on acoustic emissions from the human ear. *Phys. Lett. A.* 104:173–178.

27. Longtin, A. 1990. Oscillation onset in neural delayed feedback. *Proc. 1990 Conf. Adv. Neural Info. Process. Syst.* 3

28. Longtin, A., J. G. Milton, …, M. C. Mackey. 1990. Noise and critical behavior of the pupil light reflex at oscillation onset. *Phys. Rev. A.* 41:6992–7005.

29. Freeman, J. B., and R. Dale. 2013. Assessing bimodality to detect the presence of a dual cognitive process. *Behav. Res. Methods.* 45:83–97.

30. Fraser, A. M., and H. L. Swinney. 1986. Independent coordinates for strange attractors from mutual information. *Phys. Rev. A Gen. Phys.* 33:1134–1140.

31. Cao, L. 1997. Practical method for determining the minimum embedding dimension of a scalar time series. *Physica D.* 110:43–50.

32. Kennel, M. B., R. Brown, and H. D. Abarbanel. 1992. Determining embedding dimension for phase-space reconstruction using a geometrical construction. *Phys. Rev. A.* 45:3403–3411.

33. Ma, H.-G., and C.-Z. Han. 2006. Selection of embedding dimension and delay time in phase space reconstruction. *Front. Electr. Electron. Eng. China.* 1:111–114.

34. King, F. W. 2009. Hilbert Transforms. Cambridge University Press, Cambridge, UK.

35. Shera, C. A. 2003. Mammalian spontaneous otoacoustic emissions are amplitude-stabilized cochlear standing waves. *J. Acoust. Soc. Am.* 114:244–262.

36. Khovanov, I. A., and L. Schimansky-Geier. 2006. Spectral analysis of noisy oscillators near Hopf bifurcations. *Acta Phys. Pol. B.* 37:1551–1560.

37. Albers, D. J., and G. Hripcsak. 2012. Using time-delayed mutual information to discover and interpret temporal correlation structure in complex populations. *Chaos.* 22:013111.

38. Shlomovitz, R., Y. Roongthumskul, …, R. Bruinsma. 2014. Phase-locked spiking of inner ear hair cells and the driven noisy Adler equation. *Interface Focus.* 4:20140022.

39. Howard, J., and A. J. Hudspeth. 1988. Compliance of the hair bundle associated with gating of mechanoelectrical transduction channels in the bullfrog's saccular hair cell. *Neuron.* 1:189–199.

40. Martin, P., A. D. Mehta, and A. J. Hudspeth. 2000. Negative hair-bundle stiffness betrays a mechanism for mechanical amplification by the hair cell. *Proc. Natl. Acad. Sci. USA.* 97:12026–12031.

41. Eatock, R. A., D. P. Corey, and A. J. Hudspeth. 1987. Adaptation of mechanoelectrical transduction in hair cells of the bullfrog's sacculus. *J. Neurosci.* 7:2821–2836.

42. Le Goff, L., D. Bozovic, and A. J. Hudspeth. 2005. Adaptive shift in the domain of negative stiffness during spontaneous oscillation by hair bundles from the internal ear. *Proc. Natl. Acad. Sci. USA.* 102:16996–17001.

43. Ó Maoiléidigh, D., and A. J. Hudspeth. 2013. Effects of cochlear loading on the motility of active outer hair cells. *Proc. Natl. Acad. Sci. USA.* 110:5474–5479.

44. Arnold, L. 1998. Random Dynamical Systems. Springer, Berlin.

45. Fussmann, G. F., S. P. Ellner, …, N. G. Hairston, Jr. 2000. Crossing the hopf bifurcation in a live predator-prey system. *Science.* 290:1358–1360.

46. Fitzhugh, R. 1955. Mathematical models of threshold phenomena in the nerve membrane. *Bull. Math. Biophys.* 17:257–278.

47. Lindner, B. 2004. Effects of noise in excitable systems. *Phys. Rep.* 392:321–424.

48. Han, L., and A. B. Neiman. 2010. Spontaneous oscillations, signal amplification, and synchronization in a model of active hair bundle mechanics. *Phys. Rev. E Stat. Nonlin. Soft Matter Phys.* 81:041913.

49. Martin, P., D. Bozovic, …, A. J. Hudspeth. 2003. Spontaneous oscillation by hair bundles of the bullfrog's sacculus. *J. Neurosci.* 23:4533–4548.

50. Makarov, V. A., V. I. Nekorkin, and M. G. Velarde. 2001. Spiking behavior in a noise-driven system combining oscillatory and excitatory properties. *Phys. Rev. Lett.* 86:3431–3434.

51. Benser, M. E., N. P. Issa, and A. J. Hudspeth. 1993. Hair-bundle stiffness dominates the elastic reactance to otolithic-membrane shear. *Hear. Res.* 68:243–252.

52. Martin, P., and A. J. Hudspeth. 1999. Active hair-bundle movements can amplify a hair cell's response to oscillatory mechanical stimuli. *Proc. Natl. Acad. Sci. USA.* 96:14306–14311.

53. Martin, P., and A. J. Hudspeth. 2001. Compressive nonlinearity in the hair bundle's active response to mechanical stimulation. *Proc. Natl. Acad. Sci. USA.* 98:14386–14391.

54. Goldberg, J. M., and C. Fernández. 1971. Physiology of peripheral neurons innervating semicircular canals of the squirrel monkey. I. Resting discharge and response to constant angular accelerations. *J. Neurophysiol.* 34:635–660.

55. Kalluri, R., J. Xue, and R. A. Eatock. 2010. Ion channels set spike timing regularity of mammalian vestibular afferent neurons. *J. Neurophysiol.* 104:2034–2051.

56. Somps, C. J., R. H. Schor, and D. L. Tomko. 1994. Vestibular Afferent Responses to Linear Accelerations in the Alert Squirrel Monkey. NASA, Ames Research Center, Moffett Field, CA.

57. Goldberg, J. M., G. Desmadryl, …, C. Fernández. 1990. The vestibular nerve of the chinchilla. IV. Discharge properties of utricular afferents. *J. Neurophysiol.* 63:781–790.

Biophysical Journal, Volume *111*

Supplemental Information

Identification of Bifurcations from Observations of Noisy Biological Oscillators

Joshua D. Salvi, Dáibhid Ó Maoiléidigh, and A.J. Hudspeth

SUPPORTING MATERIAL

Identification of bifurcations from observations of noisy biological oscillators

Joshua D. Salvi, Dáibhid Ó Maoiléidigh, and A. J. Hudspeth*

Howard Hughes Medical Institute and Laboratory of Sensory Neuroscience
The Rockefeller University
1230 York Avenue, New York, NY, 10065, USA

*Correspondence: hudspaj@rockefeller.edu

Table of Contents

List of Figures

Preface

This document is a self-contained guide to the methods presented in the accompanying paper. We hope that this Supporting Material will benefit those who may wish to employ similar methodology for identification and location of bifurcations in noisy systems. The Supporting Material is organized as follows:

- **Section A: The Mechanical-Load Clamp.** We describe the theoretical foundation and implementation of a feedback-based clamp system to control the mechanical loads delivered to individual biological oscillators.
- **Section B: The Hair Bundle's State Diagram.** Having verified the mechanical-load clamp, we used this system to systematically deliver loads to individual hair bundles. This allowed us to generate a state diagram, a two-dimensional map of bundle behavior as a function of these loads.
- **Section C: Analytical Metrics.** We describe here the tools and metrics used to identify the types and locations of bifurcations near which a dynamical system might operate.
- **Section D: Noisy Simulations of Bifurcation Normal Forms.** The behavior of a system operating near a bifurcation can be reduced to a simple mathematical representation: a normal form. Here we describe each of the normal forms used in this study and provide details on how stochastic simulations were performed.
- **Section E: Noisy Simulations of a Model of Hair-Bundle Mechanics.** We describe here a qualitative model of hair-bundle mechanics that captures the dynamics of bundles across organs and species. We include details on how the simulations were performed and provide examples of the model's output.
- **Section F: Analysis of Hair Bundles in the Presence of Noise.** We provide additional details on the two classes of hair-bundle behavior and the bifurcations that correspond to these classes.
- **Section G: Noise-Induced Spiking in a Model of Hair Bundle Mechanics.** We show that a model hair bundle crossing a subcritical Hopf bifurcation displays spiking behavior resembling that of a system operating near a SNIC bifurcation.

SECTION A

The Mechanical-Load Clamp

To control the mechanical loads applied to individual hair bundles, we designed and implemented a mechanical-load clamp [1, 2]. The load clamp permits robust control of the constant force, stiffness, drag coefficient, and mass of a mechanical load. Rather than physically exchanging mechanical objects coupled to individual bundles, the bundle's load can be adjusted using only a feedback-based circuit. Here we describe both the mathematical foundation and the experimental verification of a mechanical-load clamp.

A.1 Mathematical Description

A hair bundle's mechanical load controls its function [2, 3]. This load may include a constant force, a stiffness, a drag, and a mass. The behavior of a hair bundle under different combinations of these loads can be captured by a map: a state diagram. One may thus envision an experimental system that—analogously to accessory structures *in vivo*—imposes mechanical loads to adjust the behavior of an active hair bundle. Such a system would allow characterization of a bundle's behavior throughout its state diagram. We earlier developed a feedback-based mechanical-load clamp; here we describe an extension to the system to encompass not only an external force and virtual stiffness but also a virtual drag and virtual mass.

The equation of motion for a hair bundle coupled to a flexible stimulus fiber is

$$m_B\ddot{X} + \xi_B\dot{X} + K_BX - F_A = -\xi_{XX}\dot{X} - \xi_{\Delta X}\dot{\Delta} + K_F(\Delta - X), \tag{S1}$$

in which X is the position of the hair bundle and m_B, ξ_B, and K_B are respectively its mass, drag coefficient, and stiffness. $\dot{X}$ and $\ddot{X}$ correspond to respectively the bundle's velocity and acceleration. The term F_A represents the bundle's active force. Δ and $\dot{\Delta}$ are the position and velocity of the stimulus fiber's base, K_F is the fiber's stiffness, ξ_{XX} is the drag coefficient owing to motion at the fiber's tip, and $\xi_{\Delta X}$ is that owing to motion of the fiber's base.

We measured the bundle's position by tracking the shadow of the fiber's tip, magnified and projected onto a dual-photodiode system, which generated a voltage $V_D = \alpha X$. To calculate the coefficient α, we displaced the shadow of the fiber's tip with a piezoelectric actuator in 20 µm steps. In a feedback-based position clamp, an error signal was generated in proportion to the difference between the bundle's actual position X and a commanded position X_C: $V_E = V_C - V_D = \alpha(X_C - X)$. This error signal was relayed through a differential amplifier and multiplied by a proportional gain G to generate an output voltage $V_O = GV_E$. This output signal was then directed to another piezoelectric actuator that controlled the motion of the stimulus fiber's base. The relationship between the error signal and the motion of the base of the stimulus fiber is

$$\Delta = \beta V_O = \beta G V_E = \beta G(V_C - V_D) = \alpha\beta G(X_C - X). \tag{S2}$$

The calibration term β describes the relationship between the input voltage to the piezoelectric actuator that controls the fiber's base and its resulting motion.

We can next suppose the bundle is loaded with a virtual mass m_V, a virtual drag ξ_V, stiffness K_L, and external force F_E. The external force can be considered a sum of a constant force F_C and a stimulus force F_S, $F_E = F_C + F_S$. The bundle's equation of motion then becomes

$$m_B\ddot{X} + \xi_B\dot{X} + K_B X - F_A = -m_V\ddot{X} - \xi_V\dot{X} - K_L X + F_C + F_S. \tag{S3}$$

By combining Equations S1 and S3, we obtain a relation describing the capacity of the mechanical-load clamp to deliver loads to individual hair bundles:

$$-\xi_{XX}\dot{X} - \xi_{\Delta X}\dot{\Delta} + K_F(\Delta - X) = -m_V\ddot{X} - \xi_V\dot{X} - K_L X + F_C + F_S. \tag{S4}$$

We must now calculate the value of the commanded position X_C required to deliver these virtual mechanical loads. This is achieved by combining Equations S2 and S4, yielding

$$\alpha\beta G\left(\xi_{\Delta X}\dot{X}_C - K_F X_C\right) = m_V\ddot{X} + (\xi_V - \xi_{XX} + \alpha\beta G\xi_{\Delta X})\dot{X} + \left[K_L - (1+\alpha\beta G)K_F\right]X - F_C - F_S. \tag{S5}$$

A real-time processor discretizes equation S5 with time intervals δt of equal duration. Estimates of the bundle's instantaneous velocity and acceleration at index j therefore become

$$\dot{X}_j = \frac{X_j - X_{j-1}}{\delta t}, \tag{S6}$$

$$\ddot{X}_j = \frac{X_j - 2X_{j-1} + X_{j-2}}{\delta t}. \tag{S7}$$

Combining Equations S5-S7 yields the command signal $V_{C,j}$ at the j^{th} time interval:

$$\begin{aligned} V_{C,j} = {} & \frac{\xi_{\Delta X} V_{C,j-1}}{\xi_{\Delta X} - K_F\delta t} \\ & + \left(\frac{m_V\ddot{X}_j + (\xi_V - \xi_{XX} + \alpha\beta G\xi_{\Delta X})\dot{X}_j + \left[K_L - (1+\alpha\beta G)K_F\right]X_j - F_{C,j} - F_{S,j}}{\beta G(\xi_{\Delta X} - K_F\delta t)}\right)\delta t. \end{aligned} \tag{S8}$$

Given a set of inputs G, m_V, ξ_V, K_L, F_C, and F_S, the mechanical-load clamp calculated for each time interval an appropriate command voltage according to Equation S8. For experiments in this study, we controlled only the load stiffness and constant force applied to an individual hair bundle, setting m_V, ξ_V, and sometimes F_S equal to zero.

Our experiments employed fibers with typical stiffnesses of $K_F = 100 - 300\ \mu\mathrm{N} \cdot \mathrm{m}^{-1}$ and drag coefficients of $\xi_{XX} = 130 - 250\ \mathrm{nN} \cdot \mathrm{s} \cdot \mathrm{m}^{-1}$ and $\xi_{\Delta X} = 80 - 150\,\mathrm{nN} \cdot \mathrm{s} \cdot \mathrm{m}^{-1}$ [4]. The gain G was typically 0.01-0.1.

For our experiments we computed the complete Equation S8 at each index j. This allowed us to avoid the need for assumptions regarding the bundle's drag coefficients that were required in our previous study [2]. Moreover, we previously adjusted the command voltage V_C and gain G to change the mechanical load. Here we varied only the command voltage V_C to control the load, resulting in an increase in the load clamp's stability.

A.2 Verification of the Mechanical-Load Clamp

We verified that the mechanical-load clamp successfully imposes a load stiffness and constant force on a hair bundle. To do so, we coupled the tip of a flexible glass stimulus fiber to the tip of a vertically mounted glass fiber that served as a model hair bundle. We then delivered force pulses of different amplitudes in the presence of a range of virtual load stiffnesses. This yielded a relationship that accorded with the behavior of a Hookean material (Fig. S1).

To assess the clamp's effect on spontaneously active hair bundles, we coupled the tip of a stimulus fiber to the kinociliary bulb of an active bundle from the bullfrog's sacculus. In keeping with our theoretical predictions and prior work [2, 3], a hair bundle's spontaneous oscillations decreased in amplitude and increased in frequency as the load stiffness rose (Fig. S2A). Another bundle initially exhibited multimodal oscillations for small values of load stiffness. Upon an increase in the stiffness, both the fast and slow modes of oscillation increased in frequency and decreased in amplitude until oscillations ceased altogether at a load stiffness of $500\ \mu\mathrm{N} \cdot \mathrm{m}^{-1}$ (Fig. S2B).

Finally, we assessed a simulated load clamp's effect on a model hair bundle. To do so, we performed simulations of a model of hair-bundle dynamics when coupled to a mechanical-load clamp:

$$\dot{X} = -K_B X + a(X - f) - (x - f)^3 + F_O + F_F, \tag{S9}$$

$$\tau_f \dot{f} = bx - f, \tag{S10}$$

$$F_F = K_F \left[\alpha\beta G (X_C - X) - X \right], \tag{S11}$$

in which $X_C = V_C/\alpha$ and V_C is described by Equation S8. Here a is a stiffness, F_O is the bundle's intrinsic offset force, F_F is a force exerted by the stimulus fiber onto the bundle, f is the bundle's force of adaptation, τ_f is the time constant of adaptation, and b is a stiffness. Because the model of hair-bundle dynamics has been rescaled, we additionally rescaled the load clamp's unitless parameters to exert forces of an appropriate order of magnitude. For these simulations, $a = 3.5$, $K_B = F_O = 0$, $\tau_f = 10$, $b = 0.5$, $\alpha = 10$, $\beta = 0.1$, $G = 1$, $K_F = 1$, and drag owing to the fiber has been neglected. We integrated Equations S9-S11 numerically in MATLAB (R2014a) with the Euler-Murayama method using a time step of 10^{-2} for combinations of 41 values each of constant force and load stiffness.

We calculated the amplitude and frequency of the model hair bundle's spontaneous oscillations from the largest peak in each power spectrum. Operating points for which the bundle's oscillations fell below an amplitude of 10^{-2} and displayed only single peaks in their position histograms were classified as non-oscillatory. This approach produced an artificial state diagram that agreed with theoretical predictions (Fig. S3). As the load stiffness increased, the bundle's oscillation amplitude fell and its frequency of spontaneous oscillation rose. The oscillatory region followed closely the lines of supercritical and subcritical Hopf bifurcations for this set of parameters [3]. Both in experiments and in simulations, the mechanical-load clamp therefore controlled the constant force and load stiffness applied to a hair bundle.

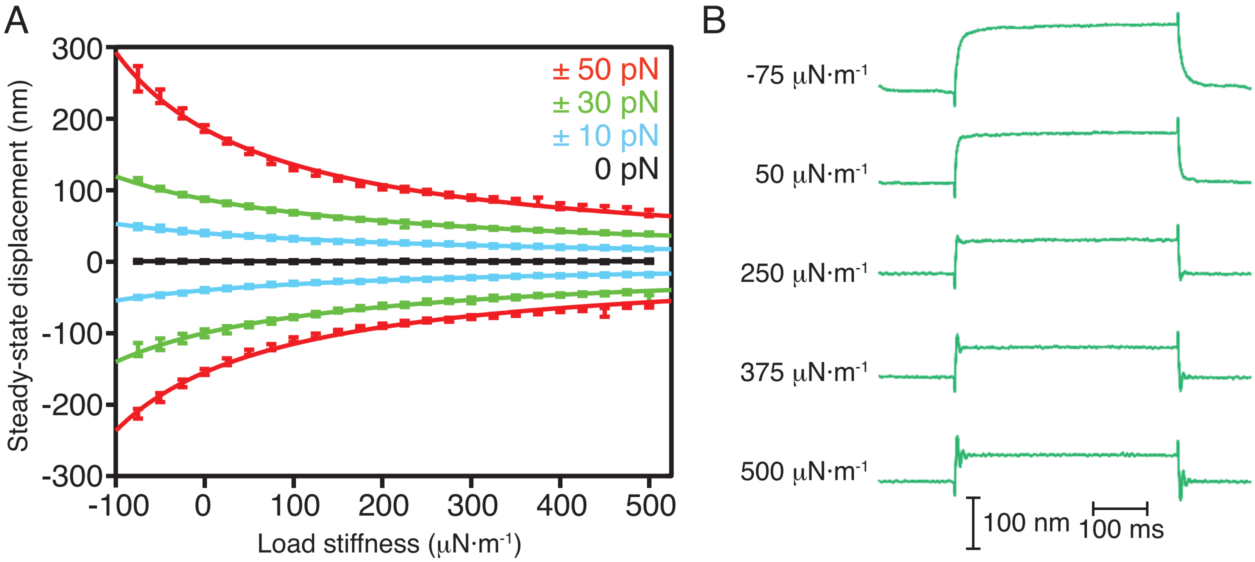

Figure S1: **Control of constant force and load stiffness with a mechanical-load clamp**. (A) To verify that a load clamp can adjust a bundle's virtual stiffness and constant force, we coupled the tip of a glass stimulus fiber to a vertically mounted fiber and delivered a series of constant forces ($F_C = 0, \pm 10, \pm 30, \pm 50$ pN) at different values of load stiffness ($-100\ \mu\mathrm{N \cdot m^{-1}} \leq K_L \leq 500\ \mu\mathrm{N \cdot m^{-1}}$). Fits to the expression $X = F_C/(K_L + K_B)$ yielded $R^2 > 0.99$ in all cases. (B) Example traces for the experiment in (A) at $F_C = 30$ pN revealed a change in the rise time of the fiber's step response: as the load stiffness increased, the rise time declined. For load stiffnesses exceeding 250 $\mu\mathrm{N \cdot m^{-1}}$, the response rang with a decay time that grew with the stiffness owing to the mass of the vertically mounted fiber. These phenomena accord with the prediction that the fiber's virtual stiffness increased. In all panels, $m_V = \xi_V = F_C = 0$ and $G = 0.01$.

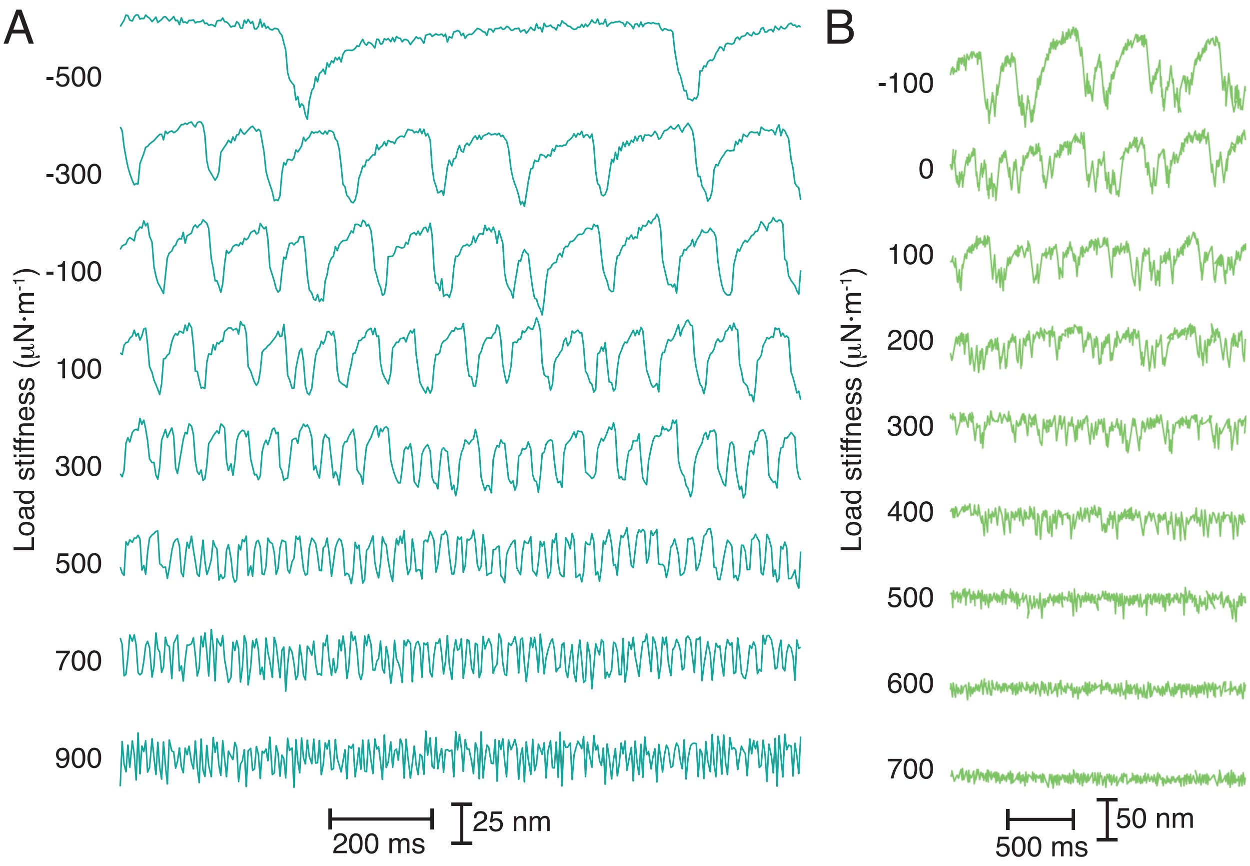

Figure S2: **Hair-bundle motion as a function of changes in load stiffness**. (A) We subjected a spontaneously oscillating hair bundle to load stiffnesses of -500 µN · m^{-1} through 900 µN · m^{-1}. As the stiffness increased, the bundle's oscillations rose in frequency and declined in amplitude. At a load stiffness of -500 µN · m^{-1}, the bundle resided mostly at a positive position with a downward excursion occurring approximately every 700 ms. (B) Imposing on another hair bundle load stiffnesses ranging from -100 µN · m^{-1} through 700 µN · m^{-1} disclosed a similar pattern in amplitude and frequency. Load stiffnesses exceeding 500 µN · m^{-1} suppressed the hair bundle's oscillations. The total acquisition time under each condition was 30 s at a sampling interval of 200 µs. The stimulus fiber possessed a stiffness of 150 µN · m^{-1} and a drag coefficient of 100 nN · s · m^{-1}. In all panels, $m_V = \xi_V = F_C = 0$ and $G = 0.01$.

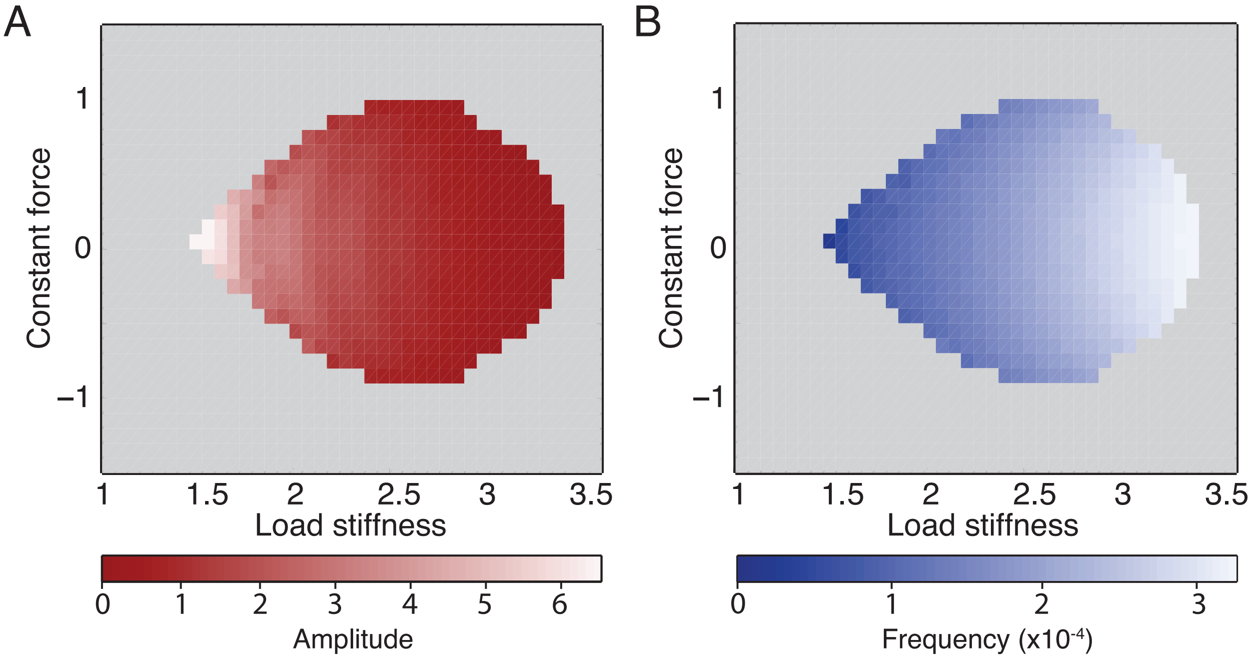

Figure S3: **Exploration of a model bundle's state diagram with a simulated load clamp**. (A) We set both the intrinsic offset force and the stiffness of a hair bundle to zero and adjusted the constant force and load stiffness applied with a virtual mechanical-load clamp. The resultant oscillatory region (red) bounded by a domain of quiescence (gray) resembled that of a bundle's theoretical state diagram (Fig. 1A). An increase in load stiffness caused a decrease in the amplitude of spontaneous oscillation. (B) The frequency of oscillation rose with an increase in load stiffness (blue).

SECTION B

The Hair Bundle's State Diagram

We used the mechanical-load clamp from Section A to control the loads applied to hair bundles of the bullfrog's sacculus. By changing the constant force and load stiffness applied to a bundle, we generated a map of the bundle's behavior—a state diagram—as a function of these two control parameters. Here we describe the statistical methods by which we classified a hair bundle's behavior as either spontaneously oscillatory or quiescent and calculated an oscillating bundle's amplitude and frequency of motion. We include the results of these measures for an individual hair bundle.

B.1 Preparation of an Experimental State Diagram

A state diagram captures the behavior of a hair bundle when coupled to different mechanical loads. We employed a mechanical-load clamp to apply loads to an individual hair bundle and recorded the bundle's position for 12 s at each operating point. From the results we could map the bundle's experimental state diagram.

For a given combination of constant force and load stiffness, a hair bundle could either oscillate spontaneously or remain quiescent. To classify a bundle's behavior, we assessed its position histogram at each operating point. If the bundle oscillated with an amplitude that exceeded the level of noise, its distribution of positions displayed at least two peaks. If the bundle instead remained quiescent or possessed oscillations indistinguishable from noise, its position distribution displayed only one. We therefore quantified the modality of the bundle's position histogram at each operating point, in which unimodal and multimodal distributions corresponded respectively to quiescent and oscillatory behavior.

Hartigans' dip statistic evaluates the modality of a distribution, with a low value reflecting a unimodal distribution [5]. To calculate the dip statistic for each combination of constant force and load stiffness, we first removed the slow drift in a time series by subtracting from it the data smoothed with a moving average with a window 1 s in width. We then eliminated high-frequency noise by applying another moving average with a window of 0.02 s in width. These procedures represented the equivalent of band-pass filtering with cutoff frequencies of 1 Hz and 50 Hz. The dip statistic was subsequently calculated from the bundle's position histogram binned according to the Freedman-Diaconis rule [6]. We tested the distribution against a null uniform distribution possessing the same mean, variance, and length as that of the experimental record. We then classified as oscillatory all operating points possessing a dip statistic of at least 0.01 and a p-value below 10^{-3}.

We employed two methods to estimate the amplitude and frequency of the bundle's spontaneous oscillations. First, we measured these values from the peak of the time series' Fourier transform. The unfiltered trace of bundle motion was multiplied by a Hamming window, mean-subtracted, and zero-padded to reduce spectral leakage and improve precision in determining the peak. Because the time series was filtered for calculation of the dip statistic, we searched for peaks across a range of 1-50 Hz. The peak's value was then rescaled by a factor calculated by applying the same procedure to a sinusoidal waveform of the same length as the original time series.

Because the Fourier transform of noisy hair-bundle motion sometimes possessed many peaks due to phase slips, changes in oscillatory frequency, and other factors, we additionally employed a peak-detection algorithm to calculate the bundle's amplitude and frequency of oscillation [7]. By finding the locations of all peaks and troughs in the time series of bundle motion, we calculated the frequency as the inverse of the mean inter-peak interval and the amplitude as half of the mean difference between each peak and trough. We tested the algorithm over a range of thresholds between the maximum noise floor and the maximum amplitude of spontaneous oscillation. Here we selected a threshold of 25 nm, which rested in the middle of this range and yielded values consistent with observations of the bundle's time-series data. Together, these methods provided two experimental state diagrams for an individual hair bundle.

B.2 Results

We subjected a hair bundle with a diameter of 4 µm from the bullfrog's sacculus to 81 combinations of constant force ranging from -80 pN to +80 pN and load stiffness from $200\,\mu\mathrm{N}\cdot\mathrm{m}^{-1}$ to $1000\,\mu\mathrm{N}\cdot\mathrm{m}^{-1}$. The hair bundle oscillated spontaneously at 60 of these operating points, resulting in an experimental state diagram with an ovoid oscillatory regime surrounded by a domain of quiescence (Fig. S4). For state diagrams calculated from a peak-detection algorithm and the Fourier transform of the time series, the bundle's amplitude fell and its frequency of oscillation rose with an increase in load stiffness. We found that the bundle's frequency of motion calculated from the Fourier transform varied over the same range of values as the frequency calculated from the peak-detection algorithm. However, due to the presence of multiple peaks in the bundle's amplitude spectrum, the amplitudes of oscillation calculated from the Fourier transform were about one-quarter of those calculated by peak detection and the frequencies of oscillation were much more variable as the control parameter was changed than those found using the peak-detection algorithm. Owing to the variability in the frequency of oscillation calculated using the Fourier transform, the correlation between the frequency of oscillation and load stiffness was statistically significant for only the peak-detection algorithm (Table S1).

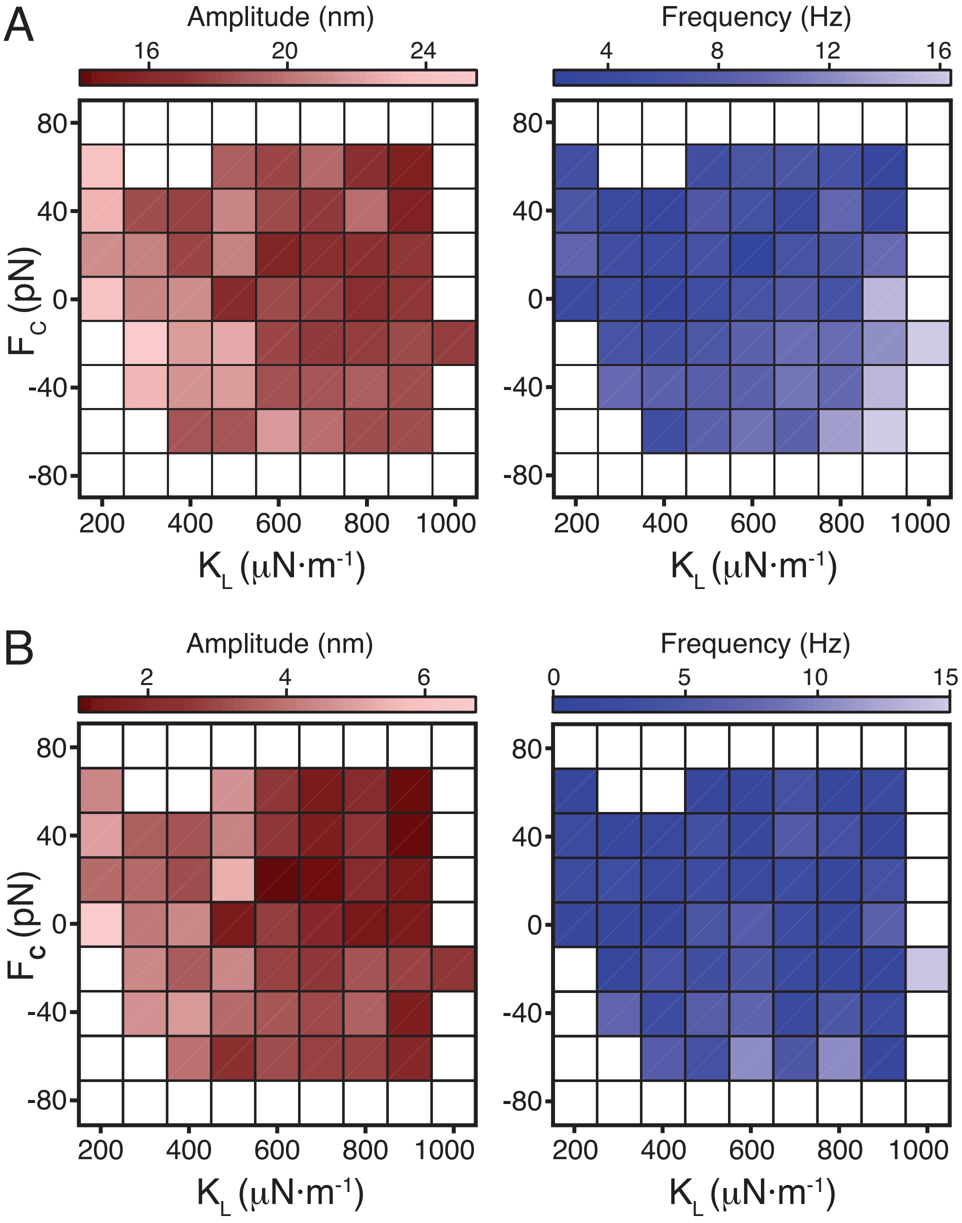

Figure S4: **A hair bundle's experimental state diagram.** (A) A hair bundle oscillated spontaneously for combinations of constant force (F_C) and load stiffness (K_L) within an oscillatory regime (colored) bounded by a region of quiescence (white). The amplitude and frequency of oscillation calculated with a peak-detection algorithm are displayed respectively in shades of red and blue. (B) The same bundle's experimental state diagram displayed similar patterns in amplitude and frequency when they were calculated from the Fourier transform of the time series of bundle motion.

PEAK DETECTION

	Ampl. ***vs*** $\mathbf{K_L}$	**Freq.** ***vs*** $\mathbf{K_L}$	Ampl. *vs* $\mathrm{F_C}$	**Freq.** ***vs*** $\mathbf{F_C}$	Ampl. *vs* Freq.
Spearman's ρ	**-0.67**	**0.48**	-0.24	**-0.56**	0.07
p-value	**7.4 x** $\mathbf{10^{-8}}$	**4.1 x** $\mathbf{10^{-4}}$	8.4 x 10^{-2}	**1.7 x** $\mathbf{10^{-5}}$	6.3 x 10^{-1}

FOURIER TRANSFORM

	Ampl. ***vs*** $\mathbf{K_L}$	Freq. *vs* $\mathrm{K_L}$	Ampl. *vs* $\mathrm{F_C}$	**Freq.** ***vs*** $\mathbf{F_C}$	Ampl. *vs* Freq.
Spearman's ρ	**-0.74**	0.13	-0.15	**-0.45**	-0.08
p-value	**3.9 x** $\mathbf{10^{-10}}$	3.5 x 10^{-1}	2.9 x 10^{-1}	**8.8 x** $\mathbf{10^{-4}}$	5.6 x 10^{-1}

Table S1: **Correlations within the bundle's experimental state diagram.** Spearman's ρ quantifies the correlations between the amplitude or frequency of oscillation and the constant force (F_C) or load stiffness (K_L). The values of Spearman's ρ and its associated p-value are shown for results from the peak-detection algorithm and from the Fourier transform of the time series. Columns in bold represent cases for which $p < 10^{-3}$.

SECTION C

Analytical Metrics

We employed several metrics to characterize the behavior of a noisy dynamical system operating near one or more bifurcations. Using these metrics, we hoped to classify the system according to the type of bifurcation near which it operates and to estimate the value of the control parameter at which the bifurcation resides. We estimated the location of a bifurcation from Hartigans' dip statistic for the distribution of positions in the time series, from the coefficient of variation for the distribution of times between successive peaks or troughs, and from the mutual information between the real and imaginary components of the analytic signal of a time series. In addition to the above metrics, we classified the type of bifurcation from the joint probability distribution of the real-valued positions of the system and its Hilbert transform and from the amplitude and frequency of the system's spontaneous motion.

We include here a set of tools that requires few manual choices by an experimenter. An experimenter should also be able to employ these metrics with ease, encountering little difficulty in either interpretation or implementation. Finally, we sought methods that can be applied to a system—such as a hair bundle—operating in an environment with substantial noise and whose time series may be of limited length.

C.1 Hartigans' Dip Statistic

A system that exhibits limit-cycle oscillations that can be distinguished from noise possesses a distribution of time-series values with more than one peak. As a measure of the onset of spontaneous oscillations, we therefore employed Hartigan's dip statistic, whose high and low values correspond respectively to multimodal and unimodal distributions. For an empirical probability density function $f(x)$ and its cumulative distribution function $F(x)$, the dip statistic is

$$D(F) = \inf_{H \epsilon \mathcal{U}} \left[\sup_{x} |F(x) - H(x)| \right], \tag{S12}$$

in which H is a member of a family of cumulative distribution functions $\mathcal{U}$ arising from unimodal probability density functions, $\inf\limits_{H \epsilon \mathcal{U}}$ is the infinum for all distributions H that are members of $\mathcal{U}$, and $\sup\limits_{x}$ corresponds to the supremum across all values of x. The maximum value of $D(F)$ is 0.25, corresponding to a maximally bimodal probability density function [5].

For stochastic simulations it was not necessary to detrend or filter the data prior to calculation of the dip statistic. For experimental time series of bundle motion, we detrended the data by subtracting the smoothened time series calculated from a moving average with a window of a length equal to half that of the time series (typically 8-30 s). Error bars from stochastic simulations represent the standard errors of the means from five time series, and those from experimental data represent standard errors calculated from 10^4 bootstrap samples. We calculated the dip statistic's p-value by comparing the dip statistic from the empirical distribution to a distribution of dip statistics drawn from $5 \cdot 10^3$ uniformly-distributed arrays, each of the same length as the original signal. Time-series data yielding $p < 10^{-3}$ were classified as oscillatory and all others as non-oscillatory.

C.2 The Analytic Distribution

The phase portrait of a dynamical system reveals fixed points and limit cycles that may be either stable or unstable. Under experimental conditions one may reconstruct an n-dimensional phase space by embedding the system's trajectory in these dimensions [8, 9]. Although this approach works in principle, phase-space embedding requires the specification of several parameters, such as the number of dimensions and a time delay [10, 11, 12]. Because these methods depend upon a number of decisions made by an experimenter and are at times difficult to employ and interpret, we instead used the Hilbert transform to reconstruct a map similar to a phase space. A real-valued signal and its Hilbert transform permit embedding of data into a two-dimensional phase space [13, 14, 15]. The analytic distribution is the joint probability distribution between the real and imaginary parts of the analytic signal. This method does not require the selection of any parameter values and can reveal both limit cycles and fixed points.

We define the Hilbert transform of a real-valued signal $X(t)$ as

$$X_H(t) = \mathcal{F}^{-1}\left[-i \cdot \mathrm{sgn}(\omega) \cdot \tilde{X}(\omega)\right], \tag{S13}$$

in which $\mathcal{F}^{-1}\left[f(x)\right]$ is the inverse Fourier transform of the function $f(x)$, $i = \sqrt{-1}$, $\mathrm{sgn}(\omega)$ is the sign function of the frequency ω, and $\tilde{X}(\omega)$ is the Fourier transform of $X(t)$. We can then generate the analytic distribution as the joint probability distribution of $X(t)$ and $X_H(t)$. For this paper, we calculated this distribution with a total of 2^8-2^{11} equal-width bins. In the presence of limit-cycle oscillations, the distribution yielded a circle or oval. The absence of limit-cycle oscillations instead revealed a unimodal density. Finally, fixed points within, on, or near a limit cycle appeared as regions of high probability within the joint distribution of $X(t)$ and $X_H(t)$.

In Fig. S5 we display higher magnification joint probability distributions corresponding to those illustrated in the main text.

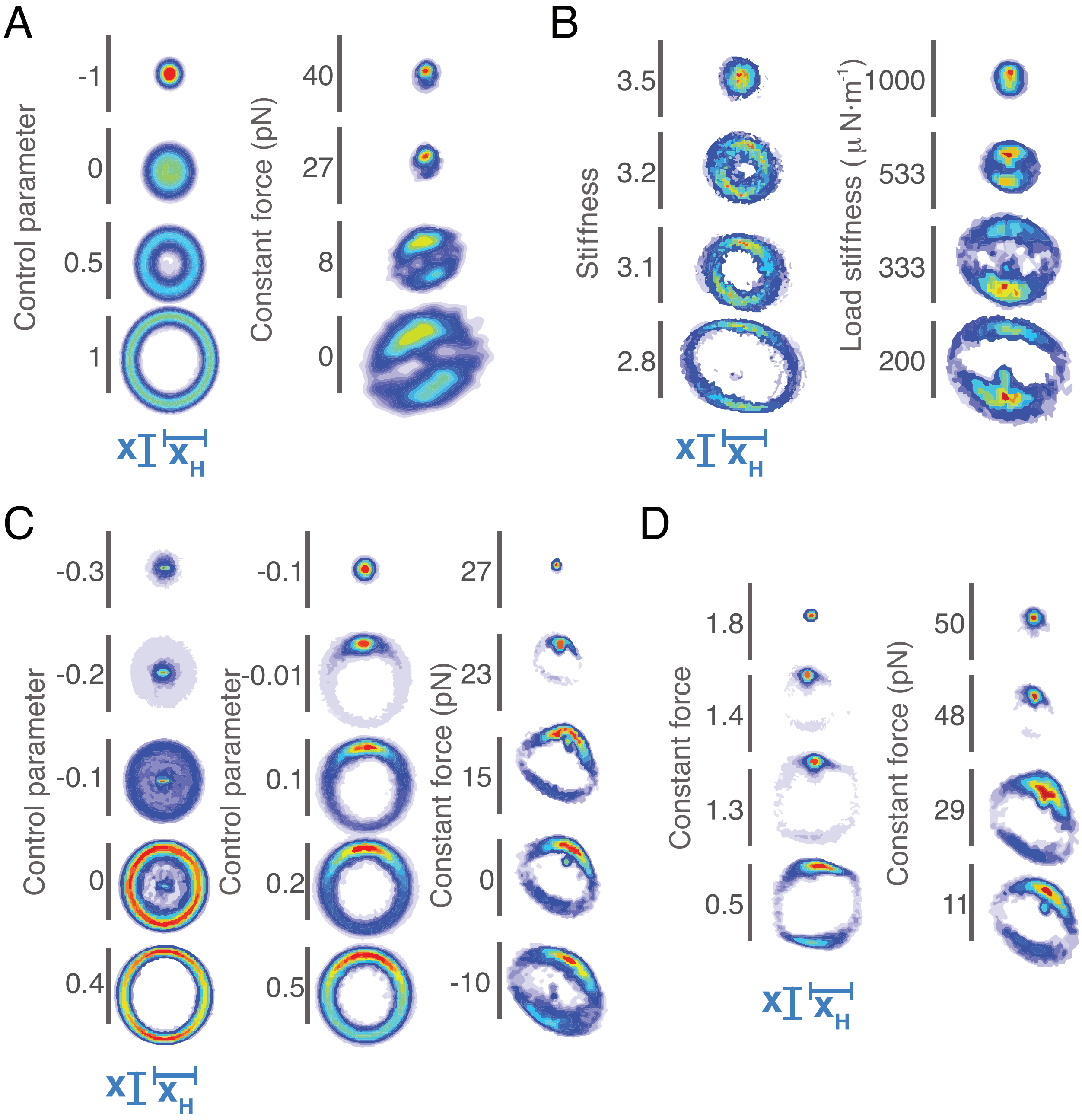

Figure S5: **Analytic distributions from a system's analytic signal.** For the distributions displayed in Fig. 2 (A), Fig. 3 (B), Fig. 4 (C), and Fig. 5 (D), we show the joint probability distributions of each system's position X and the Hilbert transform of its position X_H. The data in each column are presented in the same order as those in the associated figures.

C.3 Peak Detection

Using a peak-detection algorithm [7], we defined for each time series the local maxima and minima as respectively peaks and troughs in the signal. For a given threshold δ, peaks and troughs were defined as

$$P_j = \max_X \left\{X\colon X\epsilon\left\{P_i\colon t_{T_j} \leq t_{P_i} \leq t_{T_{j+1}}\right\}; T_j + \delta \leq X \cap T_{j+1} + \delta \leq X\right\}, \tag{S14}$$

$$T_j = \min_X \left\{X\colon X\epsilon\left\{T_i\colon t_{P_j} \leq t_{T_i} \leq t_{P_{j+1}}\right\}; P_j - \delta \geq X \cap P_{j+1} - \delta \geq X\right\}, \tag{S15}$$

in which P_j and T_j correspond respectively to the j^{th} peak or trough in the signal and t_{P_j} and t_{T_j} are the times at which the j^{th} peak or trough occurs. We specified a number of thresholds that fell between the maximum noise floor and the maximum amplitude of oscillation from the time series across all operating points.

C.4 Amplitude from Peak Detection

We defined the peak-to-peak magnitude as the difference between the value of each peak P_j and the nearest trough. For each time series, we reported the mean amplitude as one-half the mean peak-to-peak magnitude. The associated error bars represented the standard errors of the mean from five time series for stochastic simulations and the standard error from 10^4 bootstrapped samples for experimental results.

C.5 Frequency from Peak Detection

We calculated the mean frequency of oscillation $\langle r\rangle$ for each time series as the inverse of the mean inter-event interval $\langle IEI\rangle$

$$\langle r\rangle = \frac{1}{\langle IEI\rangle}, \tag{S16}$$

in which the inter-event interval corresponds to the length of time between successive peaks, $IEI_k = t_{P_{k+1}} - t_{P_k}$. The mean frequency can additionally be estimated as the number of peaks $n(P)$ divided by the length of the signal in time T:

$$\langle r\rangle = \frac{n(P)}{T}. \tag{S17}$$

In this study, we reported the frequency calculated from Equation S16 and confirmed that these values accorded with those from Equation S17. For stochastic simulations, error bars represented the standard errors of the mean from five time series. For hair-bundle data, error bars represented standard errors calculated from 10^4 bootstrapped samples.

C.6 Coefficient of Variation from Peak Detection

To assess the regularity of oscillations in a time series, we calculated the coefficient of variation C_V for the distribution of inter-event intervals

$$C_V = \frac{\sqrt{\langle \Delta IEI^2 \rangle}}{\langle IEI \rangle}, \tag{S18}$$

in which $\left\langle \Delta IEI^2 \right\rangle = \left\langle IEI^2 \right\rangle - \langle IEI \rangle^2$ represents the variance of IEI and $\sqrt{\langle \Delta IEI^2 \rangle}$ its standard deviation. The coefficient of variation is larger for irregular oscillations than it is for regular ones. We estimated the control parameter at which a bifurcation occurred as the value for which C_V crossed an empirically derived threshold. To distinguish limit-cycle oscillation from stochastic switching between stable states, we selected a threshold of 0.5 because the coefficient of variation is never less than 0.5 in the case of stochastic switching (Section D.6). Error bars represented the standard errors of the mean from five time series for stochastic simulations and standard errors from 10^4 bootstrapped samples for experimental data. In many cases we excluded from display coefficients of variation drawn from a pool of fewer than 0.05 counts per unit time (*e.g.* three counts for a 60-second time series of bundle motion or 100 counts for a numerical simulation with 10^4 units of time).

C.7 Fourier Transform

We estimated the amplitude and frequency of spontaneous oscillation from a noisy system's Fourier transform. With a moderate level of noise ($\sigma_R = \sigma_I = 0.1$, see Section D), the estimates for each time series revealed patterns consistent with those expected for a system operating near the relevant bifurcation (Fig. S6). Near a supercritical Hopf bifurcation, the amplitude rose gradually with an increase in the control parameter and the frequency of oscillation remained constant when that parameter exceeded zero (Fig. S6A). Near a SNIC bifurcation, the frequency of oscillation grew gradually from zero as the control parameter increased and the amplitude of oscillation rose sharply until it achieved a nearly constant value (Fig. S6B). Finally, a system operating near a subcritical Hopf bifurcation possessed an amplitude and frequency that both rose sharply near the associated saddle-node of limit cycles bifurcation and gradually increased thereafter (Fig. S6C). These examples show that the Fourier transform can be used to estimate the location of a bifurcation if the noise level is low.

To demonstrate that the Fourier transform of a time series may fail to evidence the presence of a bifurcation when the noise level is large, we calculated the amplitude and frequency of spontaneous oscillation from stochastic simulations of a model of hair-bundle dynamics (see Section E). Here the amplitude and frequency of oscillation failed to indicate the transection of either a subcritical or a supercritical Hopf bifurcation (Fig. S7). In spite of the fact that this simulation involved long time series ($5 \cdot 10^8$ points) and several spectra we averaged to improve the signal-to-noise ratio, the results remained poor.

We next determined that the Fourier transform of a hair bundle's time series was less successful at indicating the onset of oscillations than the peak-detection algorithm. We defined the amplitude and frequency from the peak of maximal height in the bundle's amplitude spectrum (Fig. S8A). In many cases, however, the spectrum displayed multiple peaks of similar height. The presence of more than one peak made it difficult to select an appropriate maximum, which in turn yielded a poor estimate of the frequency of spontaneous oscillation.

In response to a decrease in constant force, the peak-detection algorithm yielded a sharp rise to a nearly constant amplitude of oscillation indicating the onset of oscillations near a bifurcation and a gradual growth in frequency for both peak-detection thresholds (Fig. S8B). The amplitude and frequency estimated from the Fourier transform displayed large fluctuations obscuring the onset of oscillations (Fig. S8C). The bundle's amplitude of spontaneous oscillation calculated from the Fourier transform was sometimes only about half that computed from the peak-detection algorithm.

When a hair bundle displays spikes, calculation of its amplitude and frequency of spiking from the peak-detection algorithm yields more accurate results than those from its spectra (Fig. S9). To demonstrate this, we calculated the amplitude and frequency of spiking for a model hair bundle. The bundle displayed spikes with an amplitude exceeding one and a frequency of approximately 0.01 (Fig. S9A). The bundle's spectrum displayed a broad peak (Fig. S9B). Subdividing the signal into increasing numbers of non-overlapping windows to calculate averaged spectra made this peak clearer, but the peak remained broad. We then calculated for increasing numbers of non-overlapping windows the amplitude and frequency of spiking using both the peak-detection algorithm and the bundle's spectra. As the number of windows used for averaging increased, the amplitude of spiking calculated using three different peak-detection thresholds remained constant around 1.7-1.75 (Fig. S9C). However, the amplitude calculated from the averaged spectra increased from 0.04 to a maximum of 0.18 as the number of windows increased. The amplitude of spiking calculated using the bundle's averaged spectra therefore yielded a result that did not agree with the expected amplitude from the raw time series (Figure S9A). The frequency of spiking calculated using the peak-detection algorithm also remained constant around 0.01 as the number of windows changed (Fig. S9D). This value agrees with the expected frequency of 0.01 from the raw time series (Fig. S9A). However, the frequency of spiking calculated using the bundle's averaged spectra fluctuated greatly around 0.02-0.03 as the number of windows changed, well above the expected spiking frequency. Furthermore, there was no obvious improvement in the estimate of the bundle's frequency of spiking using its averaged spectra as the number of windows increased. The peak-detection algorithm therefore performed better than spectral analysis in capturing the amplitude and frequency of spiking. Because the peak-detection algorithm produced accurate estimates of spike amplitudes and rates and indicated the onset of oscillations, we employed this method throughout this study.

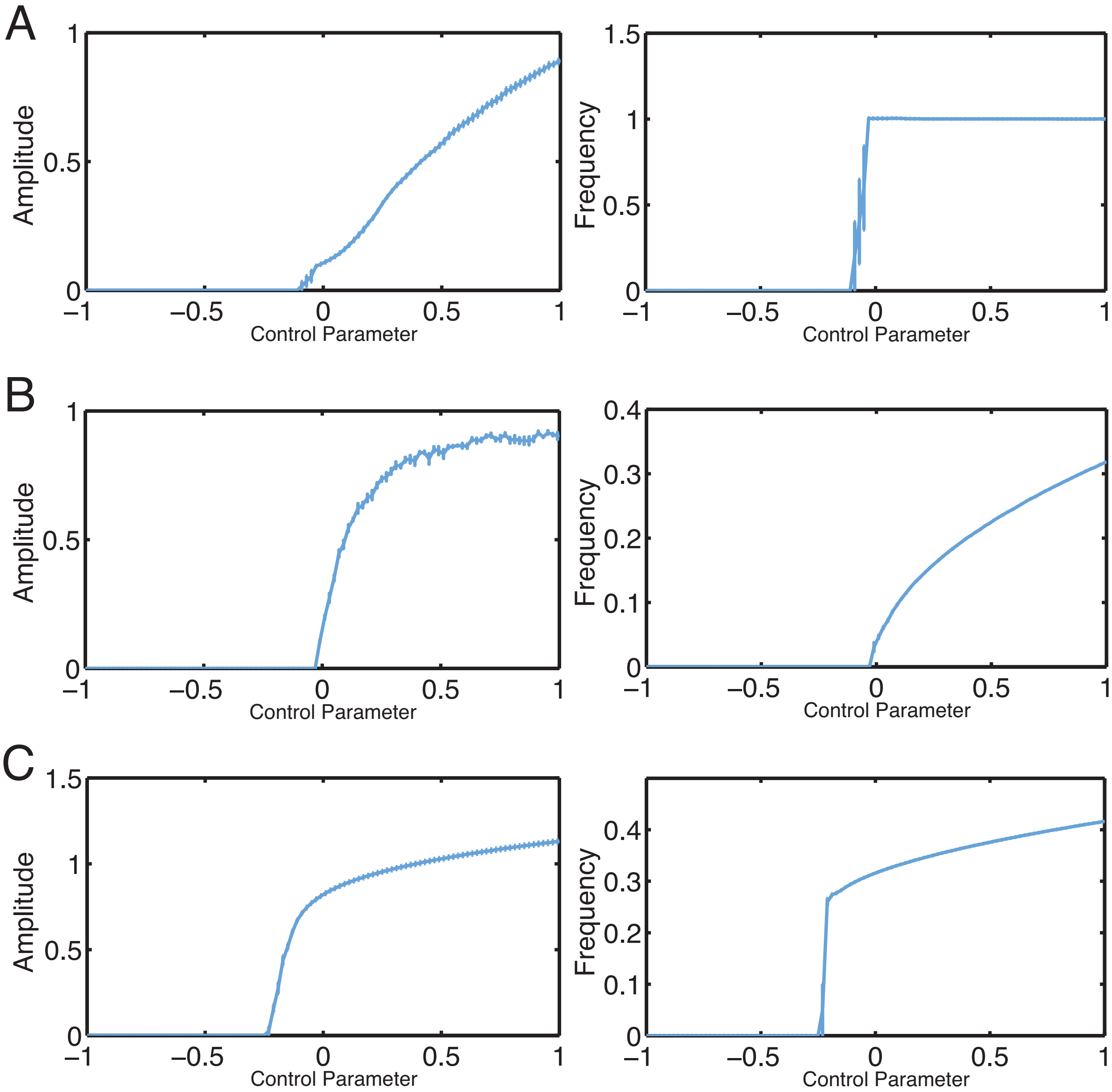

Figure S6: **Amplitude and frequency of oscillation for noisy systems near different bifurcations.** We calculated the amplitude (left column) and frequency (right column) of oscillation as the peak in the Fourier transform of a time series. (A) For a system described by the normal form of a supercritical Hopf bifurcation, the amplitude rose gradually with the control parameter and the frequency remained constant on the oscillatory side of the bifurcation. (B) A system crossing a SNIC bifurcation exhibited an oscillation amplitude that asymptoted to a constant value as the control parameter increased. With a decrease in the control parameter, its frequency of oscillation fell to an arbitrarily small value. (C) For a system described by the normal form of a subcritical Hopf bifurcation, the amplitude and frequency both increased sharply on the non-oscillatory side of the deterministic bifurcation and subsequently grew gradually as the control parameter continued to rise. All simulations were integrated numerically as described in Section D with noise levels of $\sigma_R = \sigma_I = 0.1$. Error bars correspond to the standard errors of the mean from five time series.

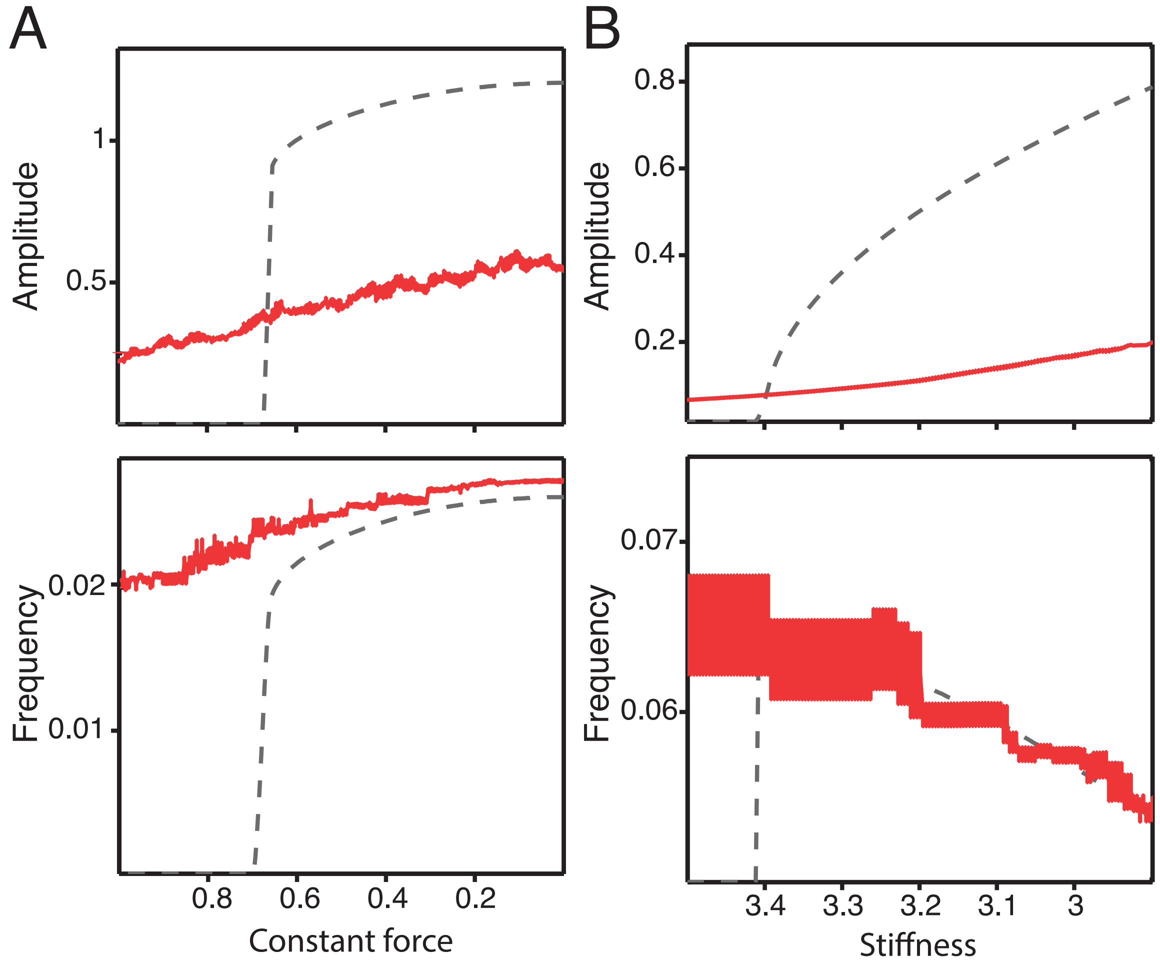

Figure S7: **Amplitude and frequency of oscillation for a model hair bundle in the presence of noise.** We calculated the amplitude (top) and frequency (bottom) of oscillation as the peak in the Fourier transform of a time series. (A) For a stiffness of 2, a model hair bundle crossed a subcritical Hopf bifurcation with changes in constant force. In the absence of noise, both the amplitude and frequency of oscillation rose sharply near the bifurcation, then gradually on the oscillatory side of the bifurcation with decreases in constant force (dashed line). In the presence of noise, neither the amplitude nor the frequency indicated a bifurcation had been transected and the amplitude fell to less than half the value obtained in the noise-free scenario (red). (B) At a constant force of 0, the model bundle crossed a supercritical Hopf bifurcation with an increase in stiffness. In the absence of noise the amplitude rose gradually from zero and the frequency achieved a non-zero value at the bifurcation before falling with further decreases in load stiffness (dashed line). The addition of noise effaced the transition from zero to non-zero in amplitude, which for the largest amplitudes fell to less than one-fifth the value of the noise-free scenario (red). The pattern in amplitude was qualitatively similar to that of the subcritical Hopf bifurcation. Noise eliminates some differences between supercritical and subcritical Hopf bifurcations. All panels correspond to numerical simulations of a model of hair-bundle dynamics as outlined in Section E with a noise level of $\sigma_X = \sigma_f = 0.2$. Error bars correspond to the standard errors of the mean from five time series.

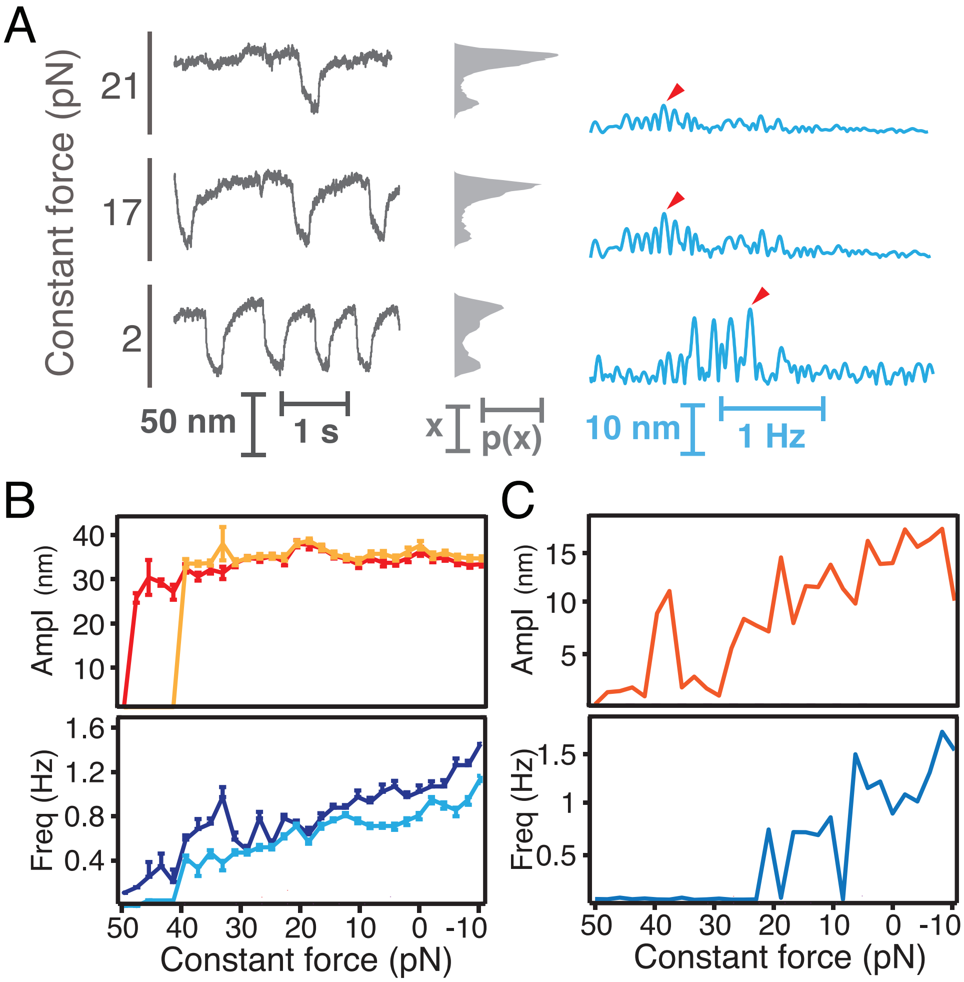

Figure S8: **Comparison of amplitude and frequency calculations for experimental data.** (A) Displayed on the left are the time series and position histograms for the bundle in Fig. 5. We calculated the amplitude and frequency of oscillation from the peak (red arrowhead) in the bundle's spectrum (blue, right). (B) We calculated with a peak-detection algorithm the bundle's amplitude (red, orange) and frequency (dark and light blue) of spontaneous oscillation. We used thresholds of 50 nm (red, dark blue) and 60 nm (orange, light blue). (C) We compared the results in panel B with the amplitude and frequency curves calculated from the bundle's Fourier transform. For all panels, the load stiffness was 100 $\mu\mathrm{N}\cdot\mathrm{m}^{-1}$ and the proportional gain was 0.1. We used a stimulus fiber with a stiffness of 139 $\mu\mathrm{N}\cdot\mathrm{m}^{-1}$ and a drag coefficient of 239 $\mathrm{nN}\cdot\mathrm{s}\cdot\mathrm{m}^{-1}$. Additional analyses can be found in Figs. 5H-N. Error bars represent standard errors of the means from 10^4 bootstrap samples. To detect a peak in the spectrum with accuracy the time series must be sufficiently long to produce the required frequency resolution. Because of this requirement the time series was not partitioned into windows for averaging.

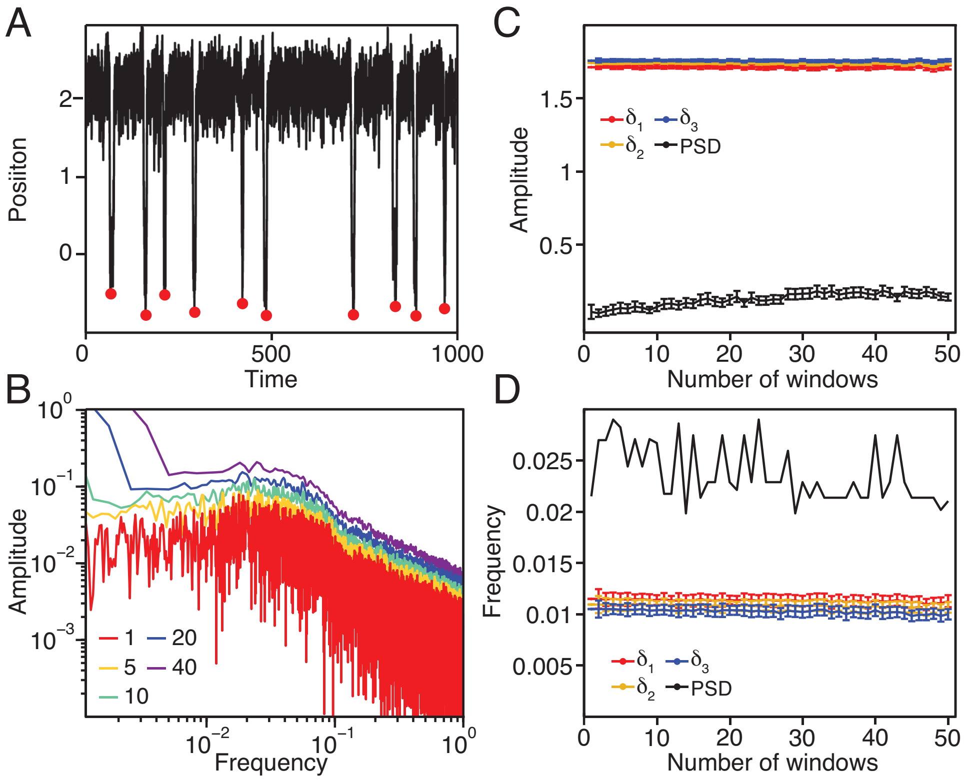

Figure S9: **Comparison of amplitude and frequency calculations for simulated data.** (A) A model bundle subjected to a constant force of 2 and a stiffness of 2 displayed large-amplitude spikes. The peak-detection algorithm successfully identified each spike for a peak-detection threshold of 3 (red circles). Over the course of this time segment, the bundle displayed approximately 0.01 spikes per time point with an amplitude larger than one. (B) Spectra for the entire time series of $2 \cdot 10^6$ time points are displayed for different numbers of non-overlapping windows, in which each spectrum is an average over the number of windows indicated (red through purple). (C) The bundle's spike amplitude was calculated using both a peak-detection algorithm with three thresholds and the averaged spectra for one through fifty non-overlapping time windows. The amplitude remained constant around 1.7-1.75 for all peak-detection thresholds ($\delta_1 = 2$, $\delta_2 = 2.5$, $\delta_3 = 3$) as the number of non-overlapping windows increased from one to fifty. However, the amplitude calculated from the peak in the bundle's averaged spectrum increased from 0.04 to a maximum of 0.18 as the number of windows increased. (D) The bundle's frequency of spiking was calculated using the same method in (C). The frequency of spiking remained constant around 0.01-0.011 for all peak-detection thresholds as the number of windows increased. However, the frequency of spiking calculated using the bundle's averaged spectra displayed large fluctuations from 0.02-0.03 as the number of windows changed from 1-48. When the number of windows became 49 or larger, the averaged spectra possessed too few points to accurately determine the position of the peak. All spectra were calculated using Welch's method. Simulations were performed in MATLAB using equations S31-S32 and a noise level of 0.4. Error bars represent standard errors of the means for the number of averages shown on the abscissa.

C.8 Analytic Information

A system that exhibits limit-cycle oscillations in a two-dimensional phase space displays a high degree of correlation between the two relevant dimensions. A system dominated by noise, however, evidences less correlation between these variables. We therefore sought to estimate the onset of limit-cycle oscillations by measuring the analytic information, which is the mutual information between the real and imaginary parts of a system's analytic signal. As described in Section C.2, we generated an analytic distribution from a system's real-valued signal X and its Hilbert transform X_H. We then calculated the mutual information between X and X_H as

$$I(X;X_H) = \sum_{i=1}^{L_X} \sum_{j=1}^{L_{X_H}} p(i,j) \cdot \log_2 \left(\frac{p(i,j)}{p(i) \cdot q(j)} \right), \tag{S19}$$

in which $p(i,j)$ is height of the bin with index $\{i,j\}$ for the histogram estimating the joint probability distribution between X and X_H and $p(i)$ and $q(j)$ are respectively the values of the marginal probability distributions of X at index i and of X_H at index j. L_X and L_{X_H} correspond respectively to the number of bins used to estimate the distributions for X and X_H. We calculated the analytic information in this manner over 2^8-2^{11} equal-width bins in the analytic distribution, employing the same number of bins for all time series in a given experiment or simulation. Using this metric, we found that the analytic information rose with the emergence of limit-cycle oscillations (Figs. 2-5). For narrow-band Gaussian noise, the analytic information instead approached zero as the length of the sequence of randomly-generated outcomes increased (Fig. S10).

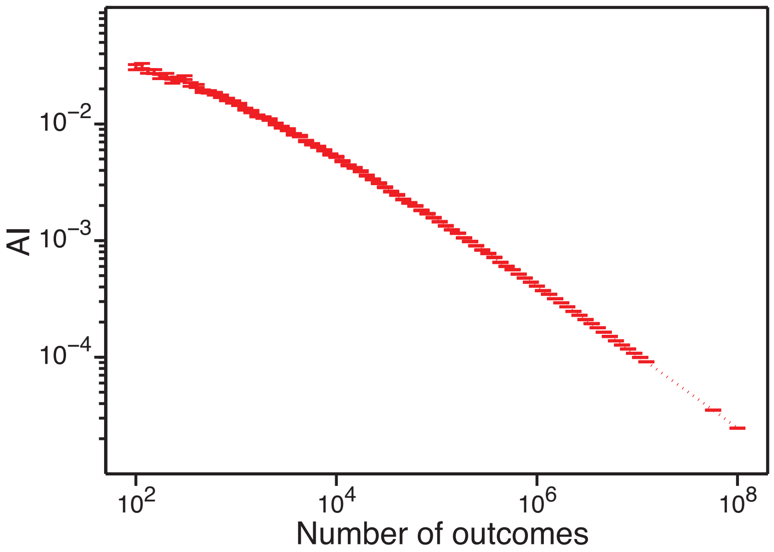

Figure S10: **Analytic information of narrow-band Gaussian noise as a function of the number of outcomes.** We calculated the analytic information for narrow-band Gaussian noise for increasing numbers of outcomes. As the number of outcomes increased by one millionfold, the analytic information fell by more than one thousandfold. All calculations of analytic information employed 2^8 equal-width bins. Error bars represent the standard errors of the mean for 100 repetitions.

Section D

Noisy Simulations of Bifurcation Normal Forms

In order to identify and locate different bifurcations in the presence of noise, we employed the metrics from Section C to noisy time series drawn from systems operating near different bifurcations. Each of these noisy systems can be described by a simple mathematical object—a normal form—that captures the generic features of a particular bifurcation. By employing the same metrics to both our simulations and our experiments, we could then compare these results to identify and locate the bifurcations near which hair bundles might operate.

We performed stochastic simulations of the normal forms of various bifurcations. All equations were numerically integrated with the Euler-Murayama method in MATLAB (R2014a). For each normal form we simulated time series across 500 values of the control parameter ranging from -5 to 5. Each time series possessed $5 \cdot 10^7$ points and was subsequently divided into five partitions of 10^7 points apiece to obtain five examples at each operating point. Each simulation incorporated white noise with standard deviations of 0.05, 0.1, 0.2, and 0.4.

D.1 Supercritical Hopf Bifurcation

Simulations of the supercritical Hopf bifurcation employed the two coupled planar equations

$$dX_R = \left[\mu X_R - \omega X_I - X_R \cdot (X_R^2 + X_I^2)\right] \cdot dt + \sigma_R \cdot dW_R, \tag{S20}$$

$$dX_I = \left[\omega X_R + \mu X_I - X_I \cdot (X_R^2 + X_I^2)\right] \cdot dt + \sigma_I \cdot dW_I, \tag{S21}$$

in which μ is a control parameter, ω is an angular frequency, and X_R and X_I are respectively the real and imaginary parts of the signal. Here W_R and W_I are Wiener processes, such that $\sigma_R \cdot dW_R$ and $\sigma_I \cdot dW_I$ are normally distributed white-noise increments with standard deviations of σ_R and σ_I. For our simulations we defined $\omega = 2\pi$. A supercritical Hopf bifurcation occurs at $\mu = 0$, birthing limit-cycle oscillations for $\mu > 0$. We therefore define $\mu < 0$ and $\mu > 0$ as respectively the quiescent and oscillatory sides of the deterministic Hopf bifurcation.

D.2 Subcritical Hopf Bifurcation

Simulations of the subcritical Hopf bifurcation employed the two coupled planar equations

$$dX_R = \left[\mu X_R - \omega X_I + X_R \cdot (X_R^2 + X_I^2) - X_R \cdot (X_R^2 + X_I^2)^2\right] \cdot dt + \sigma_R \cdot dW_R, \tag{S22}$$

$$dX_I = \left[\omega X_R + \mu X_I + X_I \cdot (X_R^2 + X_I^2) - X_I \cdot (X_R^2 + X_I^2)^2\right] \cdot dt + \sigma_I \cdot dW_I, \tag{S23}$$

in which μ is a control parameter, ω is a frequency, and the noise terms are the same as those for the supercritical Hopf bifurcation. We defined $\omega = 2\pi$ for all stochastic simulations. The subcritical Hopf bifurcation occurs at $\mu = 0$ and a saddle-node of limit cycles bifurcation resides at $\mu = -0.25$. We again define $\mu > 0$ as the oscillatory side of the deterministic Hopf bifurcation. There is a quiescent region near the subcritical Hopf bifurcation defined by $\mu < -0.25$, as there is coexistence of a limit cycle with a stable fixed point for $-0.25 < \mu < 0$.

D.3 Saddle-Node on Invariant Cycle (SNIC) Bifurcation

A system operating near a SNIC bifurcation may be defined in polar coordinates [16, 17, 18]:

$$\dot{r} = r \cdot (1 - r^2), \tag{S24}$$

$$\dot{\theta} = 1 - \cos\theta + \mu \cdot (1 + \cos\theta), \tag{S25}$$

in which r and θ describe motion in respectively the radial and angular directions. Strictly speaking, Equation S25 is the normal form of the SNIC bifurcation, and Equation S24 is an auxiliary equation that is necessary to define the amplitude dynamics. A SNIC bifurcation occurs at $\mu = 0$, with limit-cycle oscillations existing for all values of μ exceeding zero. We performed a change of variables to describe this system using the two coupled planar equations

$$dX_R = \left\{(1 - X_R^2 - X_I^2) \cdot X_R - X_I \cdot \left[1 - \frac{X_R}{\sqrt{X_R^2 + X_I^2}} + \mu \cdot \left(1 + \frac{X_R}{\sqrt{X_R^2 + X_I^2}}\right)\right]\right\} \cdot dt + \sigma_R \cdot dW_R, \tag{S26}$$

$$dX_I = \left\{(1 - X_R^2 - X_I^2) \cdot X_I + X_R \cdot \left[1 - \frac{X_R}{\sqrt{X_R^2 + X_I^2}} + \mu \cdot \left(1 + \frac{X_R}{\sqrt{X_R^2 + X_I^2}}\right)\right]\right\} \cdot dt + \sigma_I \cdot dW_I, \tag{S27}$$

in which all noise terms are defined in the same manner as those for a Hopf bifurcation. We define the quiescent and oscillatory sides of the deterministic bifurcation as respectively $\mu < 0$ and $\mu > 0$.

D.4 Saddle-Node Bifurcation

We additionally performed stochastic simulations of a system crossing a saddle-node bifurcation. To do so, we employed the normal form of a cusp bifurcation, given by [19]:

$$dX = \left[\mu + bX - X^3\right] \cdot dt + \sigma \cdot dW, \tag{S28}$$

in which μ and b are control parameters. We used $b = 0.2565$, so that a saddle-node bifurcation occurs at $\mu = \mp\frac{2}{3\sqrt{3}}b^{3/2} \approx \mp 0.05$. Simulations were obtained over 500 values of μ ranging from -0.5 to 0, each with $5 \cdot 10^8$ points and subsequently divided into five time series with 10^8 points apiece, one order of magnitude longer than the simulations described in Sections D.1-D.3.

D.5 Frequency of Motion in the Presence of Noise

We performed stochastic simulations of each of the normal forms outlined in Sections D.1-D.4. To assess the dependence of our calculations on the level of noise, we compared the relationship between frequency and control parameter at two noise levels, for which $\sigma = \sigma_R = \sigma_I$, and two peak-detection thresholds for each normal form (Fig. S11).

A system operating near a supercritical Hopf bifurcation should exhibit a discontinuous jump in frequency to a non-zero value upon crossing the bifurcation (Fig. S11A). However, the addition of noise blurred this discontinuity, resulting in a gradual rise in the frequency of oscillation to a constant value at $\mu > 0$. Increasing the value of the peak-detection threshold shifted the frequency curve rightward. A system operating in the vicinity of a subcritical Hopf bifurcation instead exhibited limit-cycle oscillations in the coexistence and quiescent regions near the deterministic bifurcation ($\mu < 0$) in the presence of noise (Fig. S11B). Although noise blurred the sharp rise in frequency predicted in a deterministic scenario, the subcritical Hopf bifurcation could be distinguished from its supercritical counterpart for sufficiently weak noise by a peak-detection algorithm. For the subcritical Hopf bifurcation an increase in the peak-detection threshold did not shift the curve rightward at low noise levels. However, when the noise was large ($\sigma = 0.2$) the shift reappeared rendering the subcritical Hopf similar to a supercritical Hopf bifurcation, as the oscillation frequency asymptotes to a constant as the control parameter is increased in both cases.

A system crossing a SNIC bifurcation displayed a frequency that rose gradually from zero in the absence of noise (Fig. S11C). Adding noise caused the system to cross a separatrix in its phase space, inducing all-or-none excursions with a frequency that depended on the noise level. Unlike the frequency relationship for a supercritical Hopf bifurcation, that of a SNIC bifurcation was insensitive to changes in the peak-detection threshold.

Finally, a system crossing a saddle-node bifurcation displayed a frequency that depended strongly on both the noise level and the peak-detection threshold (Fig. S11D). When the noise level was larger or the peak-detection threshold smaller, the detected frequency of motion increased for all operating points and achieved a maximum at $\mu = 0$. Unlike the previous bifurcations, the frequencies for different noise levels and peak-detection thresholds did not converge to the same values when the control parameter became large. For a deterministic system, in which the noise level was zero, no peaks were detected and the frequency was zero (not shown).

D.6 Irregularity of Interpeak Intervals in a Bistable System

A bistable system displays noise-induced switching between its stable states, revealing a bimodal distribution of positions. Because the switching arises from noise-induced motion, however, we expect the residence times to be irregular. In such a scenario, the distribution of interpeak intervals will be broad and the coefficient of variation large. The coefficient of variation does not distinguish between the monostable and bistable sides of a saddle-node bifurcation (Fig. S12). The dip statistic rises, however, as a system transitions from monostability to bistability.

Stochastic switching between states A and B of a double-well potential can be idealized by homogeneous Poisson processes between the two states. The distribution of durations for which the particle remains in either state A or state B—the residence-time distribution—is therefore exponential. When calculating the coefficient of variation we quantified the time between peaks in a time series, which represents the time for a particle to start in state B (or A) and to return to state B (or A). Let the time τ between events represent the time between starting in state B and returning to state B. The distribution of τ follows

$$P(\tau) = N \cdot \int_0^{\tau} \lambda_1 \exp\left(-\lambda_1 t\right) \lambda_2 \exp\left(-\lambda_2(\tau - t)\right) dt, \tag{S29}$$

in which N is a normalization constant, and λ_1 is the rate at which the system transitions from B to A and λ_2 is the rate of transitioning from A to B. The coefficient of variation for this distribution is

$$C_V = \frac{\sqrt{\lambda_1^2 + \lambda_2^2}}{\lambda_1 + \lambda_2}. \tag{S30}$$

In the case that $\lambda_1 = \lambda_2$, the coefficient of variation becomes $C_V = 1/\sqrt{2} \approx 0.7$. When either $\lambda_1 \to \infty$ or $\lambda_2 \to \infty$, the coefficient of variation instead becomes $C_V = 1$, which is what we expect for an exponential distribution. Consequently, a noisy, bistable system's coefficient of variation never falls below 0.7. To rule out bistability in experimental observations, we choose a threshold for the coefficient of variation of 0.5. This conservative threshold allows us to account for numerical errors that could allow the coefficient calculated for a bistable system to attain values slightly below 0.7 (Fig. S12). The variance in the recurrence time is smaller in the two-state Poisson process limit than it is for a system with multiple stable states. The coefficient of variation for a multistable system therefore always exceeds $1/\sqrt{2}$. This threshold on the coefficient of variation therefore distinguishes a system's operation in a bistable or multistable regime from operation in a regime allowing limit-cycle oscillations.

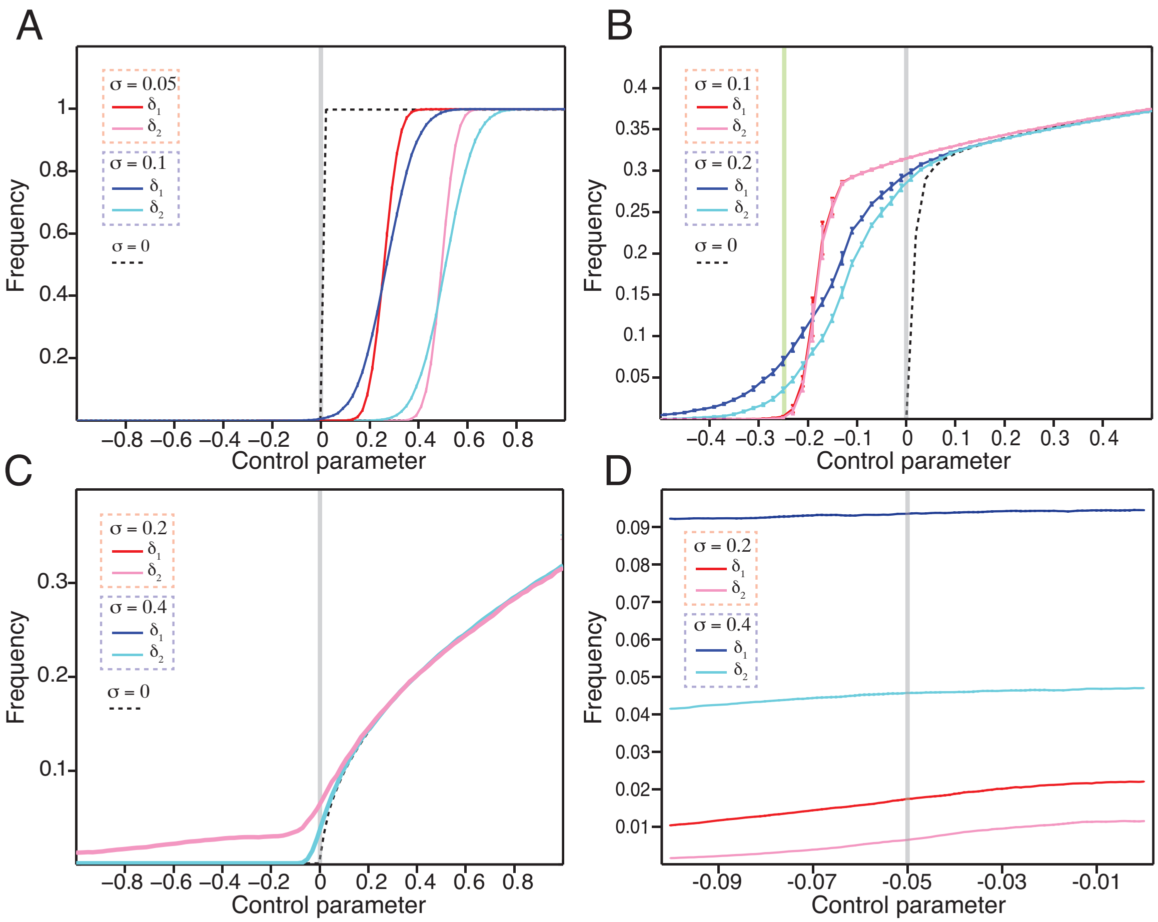

Figure S11: **Dependence of the frequency of oscillation on noise level.** (A) Simulations of the normal form of a supercritical Hopf bifurcation reveal changes in the frequency of oscillation with variation of the control parameter. Here the bifurcation resides at $\mu = 0$ (gray line). In the absence of noise, the spike rate discontinuously jumped to a non-zero value and remained constant upon crossing the bifurcation (dashed line). Adding noise caused the slope of this relationship to decrease as a function of the noise level (red *vs.* blue). Changing the peak-detection threshold at a given level of noise shifted the frequency relationship without changing its slope (red *vs.* pink). (B) A subcritical Hopf bifurcation resides at $\mu = 0$ (gray line) and a saddle-node of limit cycles at $\mu =$ -0.25 (green line). In the absence of noise with initial conditions $X_R = X_I \approx 0$, the spike rate rose discontinuously upon crossing the Hopf bifurcation and slowly increased until it achieved a constant value for $\mu \gg 0$. Adding noise caused limit-cycle oscillations to appear in the coexistence and quiescent regions near the deterministic bifurcation ($\mu < 0$). With a low noise level, the spike rate curve had a similar shape as in the deterministic case and fell to zero near the saddle-node of limit cycles (red and pink). Higher noise levels skewed the curve and induced ringing in the quiescent regime (blue and cyan). Changing the threshold yielded either little change in the spike rate relationship (red *vs.* pink) or a small change in its slope and magnitude near the bifurcation (blue *vs.* cyan). (C) A SNIC bifurcation occurs at $\mu = 0$ (gray line). Oscillations emerged with an arbitrarily low frequency at $\mu = 0$ and grew in frequency as μ increased. Adding noise increased the frequency near the bifurcation and induced oscillations for $\mu < 0$. Changing the peak-detection threshold caused no change in this relationship. (D) A saddle-node bifurcation occurs near $\mu =$ -0.05. Increasing the noise level or decreasing the peak-detection threshold increased the fluctuation frequency across all operating points. For panels A-C, we employed thresholds of $\delta_1 = 1$ and $\delta_2 = 1.5$. Panel D employed thresholds of $\delta_1 = 0.8$ and $\delta_2 = 1.2$. Deterministic plots were calculated with a threshold of 10^{-3}. Error bars represent standard errors of the means for five time series.

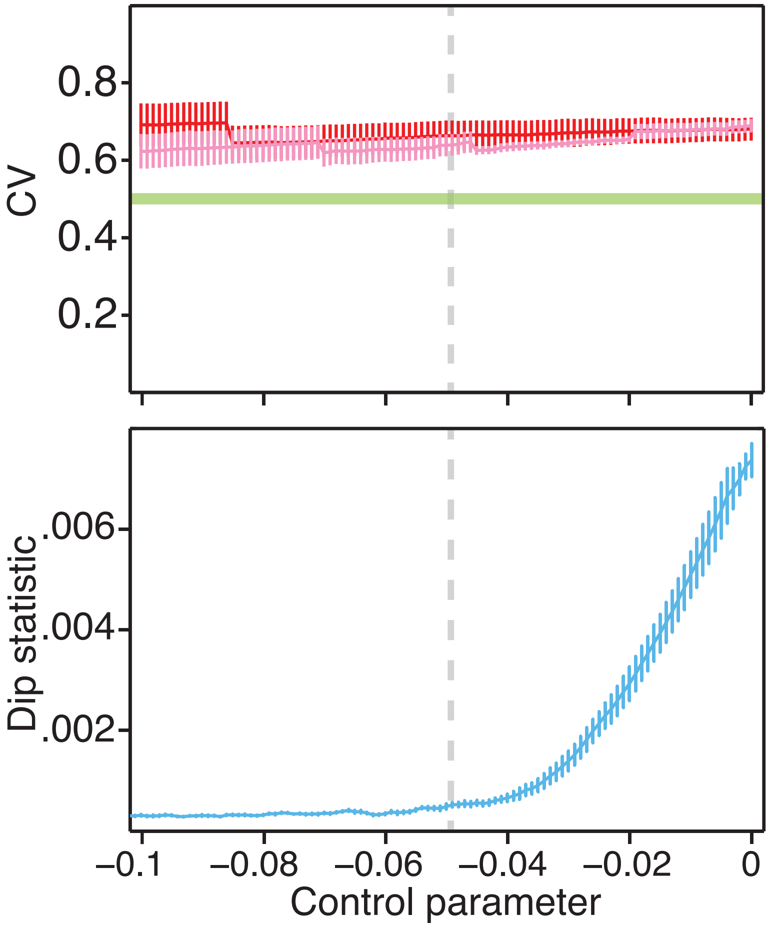

Figure S12: **Coefficient of variation and dip statistic for a system possessing both monostable and bistable regimes.** A system is monostable for control-parameter values below -0.05 and bistable for values above this threshold, at which a saddle-node bifurcation occurs. (Top) For a noisy system crossing a saddle-node bifurcation, the coefficients of variation remained larger than a threshold of 0.5 (green line) for peak-detection thresholds of $\delta_1 = 0.8$ (red) and $\delta_2 = 1.2$ (pink) and a noise level of $\sigma = 0.4$. (Bottom) At the same noise level, the system displays a rise in its dip statistic after crossing the saddle-node bifurcation. Gray dashed lines correspond to the saddle-node bifurcation's location. Error bars represent standard errors of the mean for five repetitions.

SECTION E

Noisy Simulations of a Model of Hair-Bundle Mechanics

We next wished to compare the behavior of experimentally observed hair bundles to simulated ones whose operation near a particular bifurcation is known. This allowed us to test the metrics in Section C on a noisy system that possesses both the generic features of particular bifurcations and behaviors specific to hair bundles. In doing so, we could further verify our ability to identify and locate bifurcations near which noisy bundles might operate.

We performed stochastic simulations of a model of hair-bundle dynamics by the method outlined in Section D. Each time series contained $5 \cdot 10^8$ points and was divided into five partitions of 10^8 points apiece to obtain five examples at each of 500 operating points. Each simulation incorporated white noise generated by the Mersenne twister pseudorandom-number generator with standard deviations of 0.05, 0.1, 0.2, 0.4, 0.5, and 1. We repeated the simulations for a constant force of 0 with stiffnesses ranging from 0 through 4 and for load stiffnesses of 1.5, 1.75, 2, 2.5, and 3 with constant forces ranging from 0 through 2.

E.1 Mathematical Description

The following description captures the dynamics of a mechanically loaded hair bundle [2, 3]:

$$dX = \left[a \cdot (X - f) - (X - f)^3 - K_T \cdot X + F_C\right] \cdot dt + \sigma_X \cdot dW_X, \tag{S31}$$

$$df = \frac{1}{\tau_f}\,(b \cdot X - f) \cdot dt + \sigma_f \cdot dW_f, \tag{S32}$$

in which X is the bundle's position, f is the force owing to adaptation, a is stiffness owing to gating of the mechanotransduction channel, τ_f is the timescale of adaptation, and b is a stiffness coupling bundle position to adaptation. The total stiffness of the bundle with a mechanical load is $K_T = K_B + K_L$, in which K_B is the bundle's stiffness and K_L is that of its load. The bundle may also be subjected to a constant force F_C. W_X and W_f are Wiener processes such that $\sigma_X \cdot dW_X$ and $\sigma_f \cdot dW_f$ are normally distributed white-noise increments with standard deviations of σ_X and σ_f. For all simulations, we used $\sigma = \sigma_X = \sigma_f$, $a = 3.5$, $b = 0.5$, and $\tau_f = 10$.

E.2 Analysis of a Model Hair Bundle in the Presence of Noise

We assessed the effects of noise on the behavior of a model hair bundle crossing either a subcritical or a supercritical Hopf bifurcation. To achieve this we calculated the frequency of spontaneous oscillation as a function of the control parameter for two levels of noise and two peak-detection thresholds (Fig. S13).

When subjected to increasing values of constant force, a model hair bundle with a stiffness of 2 crossed a subcritical Hopf bifurcation (Fig. S13A, [3]). At high values of the constant force the bundle exhibited no spontaneous activity. Decreasing the constant force below a critical value caused a sudden onset of limit-cycle oscillations that corresponded to a discontinuous jump in frequency in the absence of noise. The frequency then rose slowly with further decreases in the constant force. When noise was added, the discontinuity in frequency disappeared and the bundle's oscillations decreased gradually to zero with increased force. Raising the level of noise caused the bundle to oscillate spontaneously at larger values of constant force, indicating that a hair bundle may exhibit spontaneous oscillations far from the deterministic subcritical Hopf bifurcation. Finally, changing the value of the peak-detection threshold caused no changes in the relationship between frequency and constant force.

A model hair bundle subjected to a constant force of 0 and increasing values of stiffness instead crossed a supercritical Hopf bifurcation (Fig. S13B, [3]). When the stiffness was large, the bundle exhibited no spontaneous motion in the absence of noise. Upon reduction of the stiffness below a critical value, limit-cycle oscillations emerged at a non-zero frequency. Further decreases in the stiffness caused a decline in the bundle's frequency of oscillation. As for a bundle operating near a subcritical Hopf bifurcation, adding noise to the system obscured the discontinuity in the relationship between frequency and stiffness. Unlike that of a subcritical Hopf bifurcation, however, the frequency relationship shifted rightward with an increase in the peak-detection threshold value.

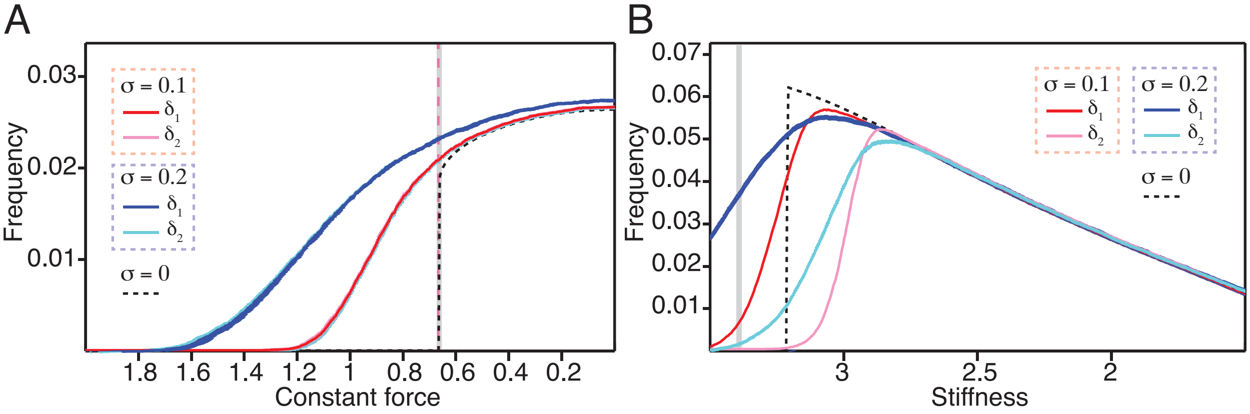

Figure S13: **Effects of noise on a model hair bundle's frequency of oscillation.** (A) A model hair bundle was poised at a stiffness of 2 and subjected to an array of 500 constant forces ranging from 0 through 2 such that the bundle crossed a subcritical Hopf bifurcation (gray line). In the absence of noise, the bundle exhibited spontaneous oscillations whose frequency rose discontinuously at a critical value of the constant force (black dashed line). The slope of the frequency relationship decreased as a function of noise level, obscuring the discontinuity (solid lines). Changes to the peak-detection threshold did not appreciably alter the frequency relationship. A saddle-node of limit cycles bifurcation occurred at $F_C = 0.664$ (pink dashed line). (B) A model bundle was poised at a constant force of 0 and subjected to 500 stiffnesses ranging from 1.5 through 3.5 such that the bundle crossed a supercritical Hopf bifurcation (gray line). In the absence of noise, spontaneous oscillations emerged with a non-zero frequency at a critical value of the total stiffness and the frequency of oscillation fell with decreased stiffness (dashed line). Adding noise reduced the slope of the rise in frequency (solid lines). Increasing the peak-detection threshold shifted the frequency curves rightward. All error bars represent standard errors of the means from five time series. We employed thresholds of $\delta_1 = 1$ and $\delta_2 = 1.5$. Deterministic plots were calculated with a threshold of 10^{-3} in both panels.

SECTION F

Analysis of Hair Bundles in the Presence of Noise

We found that hair bundles exhibited at least two classes of behavior that corresponded to operation near distinct bifurcations. Here we include extended time-series data that correspond to these two regimes.

F.1 Operation Near a Supercritical Hopf Bifurcation

A hair bundle subjected to a large load stiffness and a constant force of 0 displayed behaviors consistent with those of a system near a supercritical Hopf bifurcation (Fig. S14A). As the load stiffness fell, the bundle's amplitude of spontaneous oscillation increased. We additionally observed a decline in the frequency of oscillation that agreed with simulations of a model of hair-bundle dynamics (Fig. S13B). The joint probability distribution of the bundle's position and the Hilbert transform of its position possessed a circular region that increased in diameter with a decrease in load stiffness.

F.2 Operation Near a SNIC or Subcritical Hopf Bifurcation

Subjecting another bundle to a small load stiffness and a range of constant forces evoked behaviors that accorded with operation near either a SNIC or a subcritical Hopf bifurcation (Fig. S14B). A decrease in constant force caused the bundle to exhibit asymmetric oscillations with downward excursions that resembled spikes. The interval between successive excursions fell with a decrease in constant force. Joint probability distributions of the bundle's position and its Hilbert transform disclosed a limit cycle whose diameter remained invariant to changes in constant force. A region of high probability additionally existed on the limit cycle. Although we expected the bundle to cross a subcritical Hopf bifurcation in the low-stiffness regime [3], the behavior instead resembled that of a system near a SNIC bifurcation. We noted, however, that the same behaviors arose in our model of hair-bundle mechanics when noise was added to the system (Figs. 5, S13A). We therefore hypothesize that a hair bundle crossing a subcritical Hopf bifurcation can exhibit behaviors resembling those of a system near a SNIC bifurcation. We further explore this phenomenon in Figures 4 and 5.

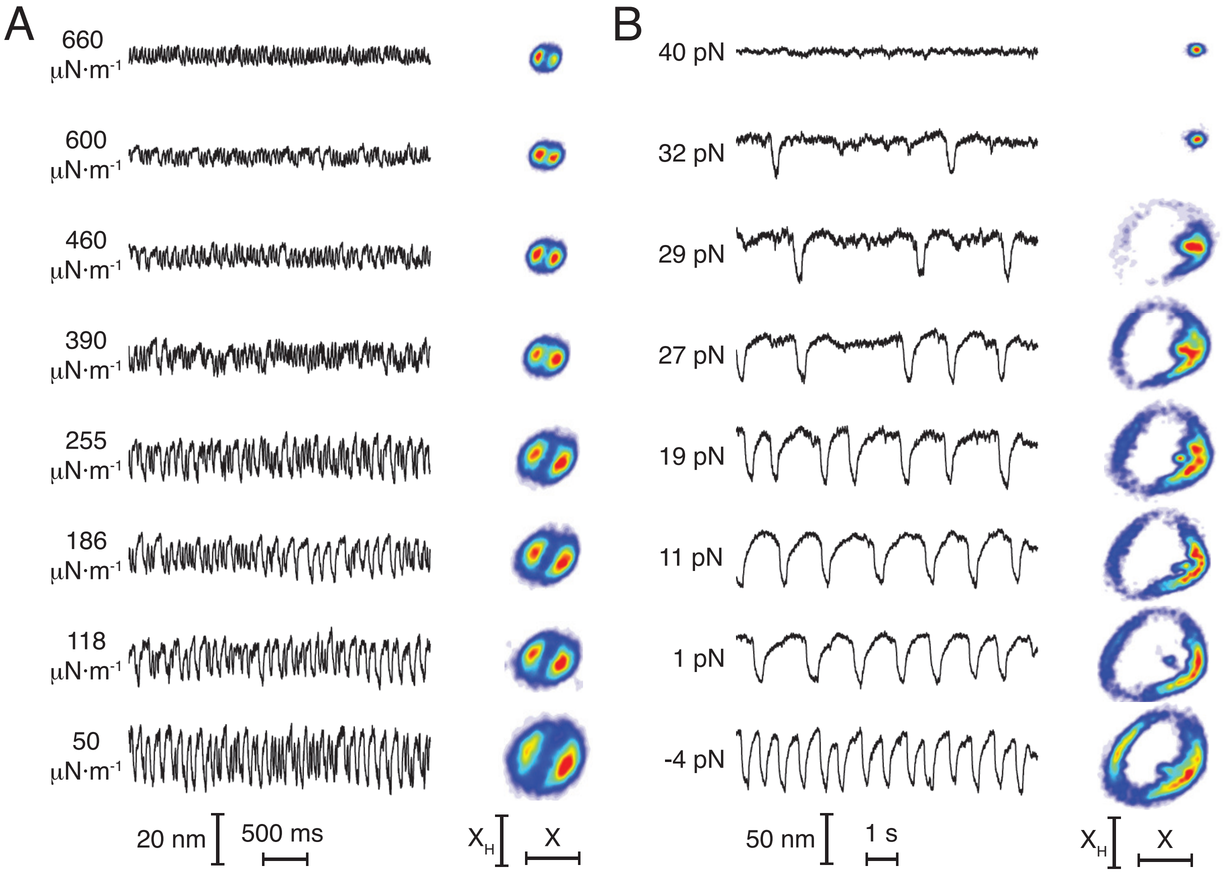

Figure S14: **Two classes of hair-bundle behavior.** (A) While subjecting a hair bundle to a constant force of 0 and load stiffnesses ranging from 50 $\mu\mathrm{N}\cdot\mathrm{m}^{-1}$ through 660 $\mu\mathrm{N}\cdot\mathrm{m}^{-1}$, we monitored its position over the course of 30 s under each condition. We display a 3.5 s window of each time series. (left) The bundle oscillated spontaneously with high frequency and low amplitude at a load stiffness of 660 $\mu\mathrm{N}\cdot\mathrm{m}^{-1}$. Reducing the load stiffness caused the bundle's oscillations to decrease in frequency and increase in amplitude. (right) The distributions of the bundle's position X and its Hilbert transform X_H based on 30 s of data revealed a limit cycle whose diameter rose with a decrease in load stiffness. (B) We subjected a second hair bundle to a load stiffness of 50 $\mu\mathrm{N}\cdot\mathrm{m}^{-1}$ and constant forces ranging from -4 pN to 40 pN and tracked its motion over a course of 30 s under each condition, and we display a 10 s window of each time series. Subjecting the bundle to a constant force of 40 pN suppressed its spontaneous activity (left). Decreasing the force caused downward excursions to emerge at a low frequency; further declines in the constant force increased the frequency of these excursions. Distributions of the bundle's position X and its Hilbert transform X_H based on 30 s of data indicated the presence of a single fixed point at a constant force of 40 pN (right). Reducing the force to 29 pN unveiled a limit cycle upon which rested a region of high probability. Further decreases in constant force caused the bundle to reside with greater probability at other positions along the cycle. For forces below 19 pN, a region of high probability appeared within the cycle. All data were acquired at sampling intervals of 1 ms. The stimulus fiber possessed a stiffness of 260 $\mu\mathrm{N}\cdot\mathrm{m}^{-1}$ and a drag coefficient of 130 $\mathrm{nN}\cdot\mathrm{s}\cdot\mathrm{m}^{-1}$.

SECTION G

Noise-Induced Spiking in a Model of Hair-Bundle Mechanics

We hypothesized that a hair bundle achieves behaviors resembling those of a system near a SNIC bifurcation through an asymmetry in its phase space and quasi-threshold phenomena similar to those in models of spiking neurons [20, 21, 22]. In other words, a bundle could exhibit noise-induced excursions resembling all-or-none spikes in the quiescent regime at small stiffnesses. We assessed this possibility by analyzing the vector fields for a model hair bundle within different regions of its state space.

G.1 Effects of Constant Force and Stiffness

We first assessed the vector fields of our model of hair-bundle dynamics when the bundle was subjected to a low stiffness and increasing values of constant force. When its operating point rested on the oscillatory side of a subcritical Hopf bifurcation, the bundle exhibited limit-cycle oscillations (Figs. S15A-B). All trajectories proceeded toward a stable limit cycle in which the bundle displayed relaxation oscillations. The slow parts of each cycle corresponded to trajectories that fell near the cubic $\dot{X} = 0$ nullcline and the fast parts to rapid jumps across this nullcline's middle region. An unstable fixed point was situated at the intersection of the cubic $\dot{X} = 0$ and linear $\dot{f} = 0$ nullclines. An increase in the constant force caused the cubic nullcline to migrate in the positive X- and f-directions until the fixed point became stable at a subcritical Hopf bifurcation and the limit-cycle attractor subsequently disappeared at the nearby saddle-node of limit cycles (Figs. S15B-C). This behavior closely resembled the excitation-block phenomenon in models of neuronal dynamics [23]. After the bundle's operating point crossed a subcritical Hopf bifurcation and the subsequent saddle-node of limit cycles bifurcation, the bundle's trajectories converged on a stable fixed point (Fig. S15C). Trajectories diverged sharply from a region near and above the middle part of the cubic nullcline. If the hair bundle's trajectory were to cross this quasi-threshold region, the trajectory would correspond to a large-amplitude excursion in X as it extended toward one of the cubic nullcline's side branches [20, 24, 25]. Further increases in constant force propelled the stable fixed point farther from the middle branch of the cubic nullcline (Fig. S15D). By increasing the distance between the stable fixed point and the quasi-threshold region, a larger perturbation would be required to move the bundle's trajectory beyond the quasi-threshold.

We next assessed the behavior of a model hair bundle subjected to a constant force of zero and increasing values of stiffness. As the bundle's stiffness increased and its operating point approached a supercritical Hopf bifurcation, the slope of the middle branch of the $\dot{X} = 0$ nullcline fell (Figs. S16A-B). This caused the diameter of the limit cycle to decline with an increase in stiffness. On the quiescent side of the deterministic bifurcation, the slope of the middle branch of the $\dot{X} = 0$ nullcline became negative, rendering its fixed point stable (Figs. S16C-D). Because in the quiescent regime there existed no divergent trajectories near the $\dot{X} = 0$ nullcline, no quasi-threshold existed.

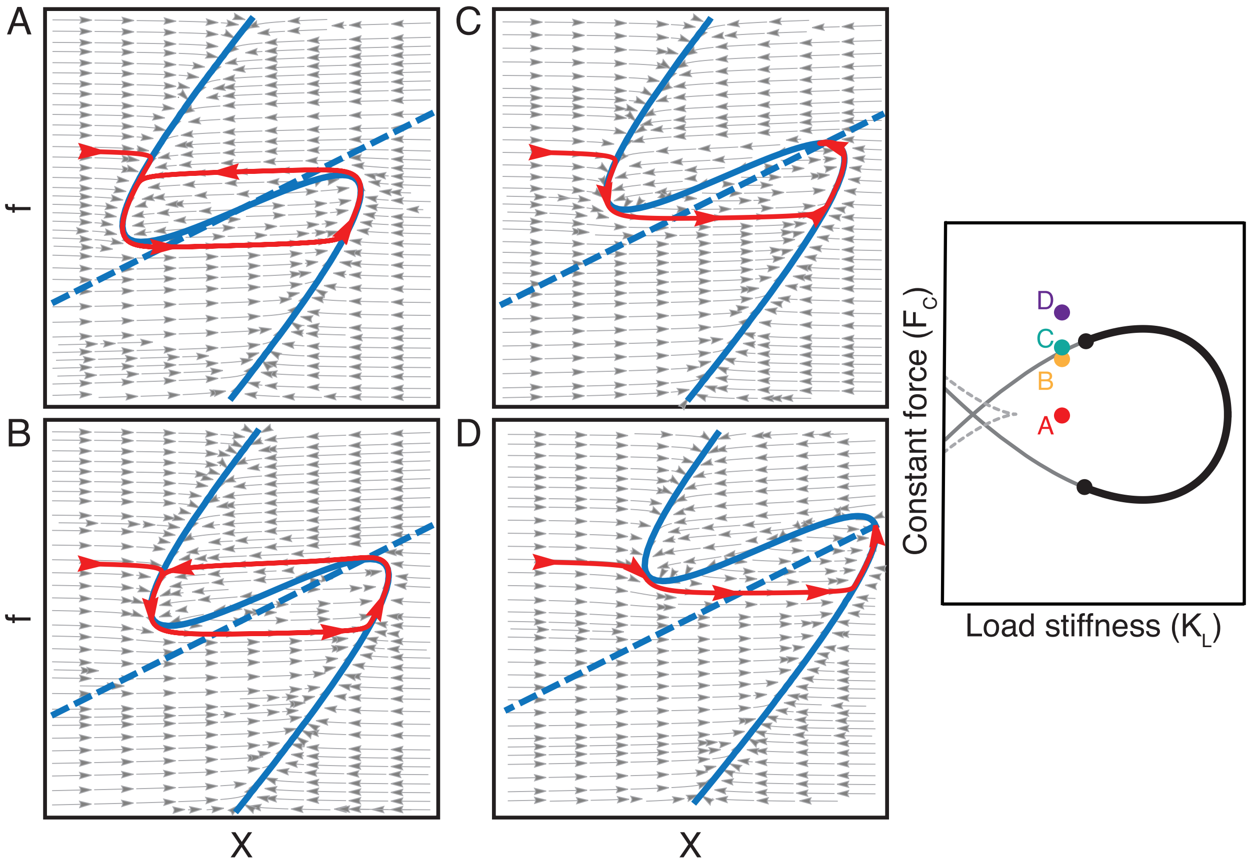

Figure S15: **Vector fields for a model hair bundle as a function of constant force.** We calculated the vector fields in the bundle's position X and the adaptive force f from Equations S31 and S32. As depicted in the panel on the right, we subjected the hair bundle to a stiffness of 2 and constant forces of 0 (A), 0.6 (B), 0.7 (C), and 1.5 (D); the bundle's operating point crossed a subcritical Hopf bifurcation at a constant force of 0.66. A fixed point resided at the intersection of the $\dot{X} = 0$ (solid blue) and $\dot{f} = 0$ (dashed blue) nullclines. Gray arrows indicate the local directions of trajectories. Although trajectories always cross the X nullcline vertically and the f nullcline horizontally, the region over which this occurs is often too small for the trajectories' directions to be represented accurately by the arrows. Red curves and arrows highlight example trajectories in the absence of noise. All panels were generated in Mathematica (10.2.0.0).

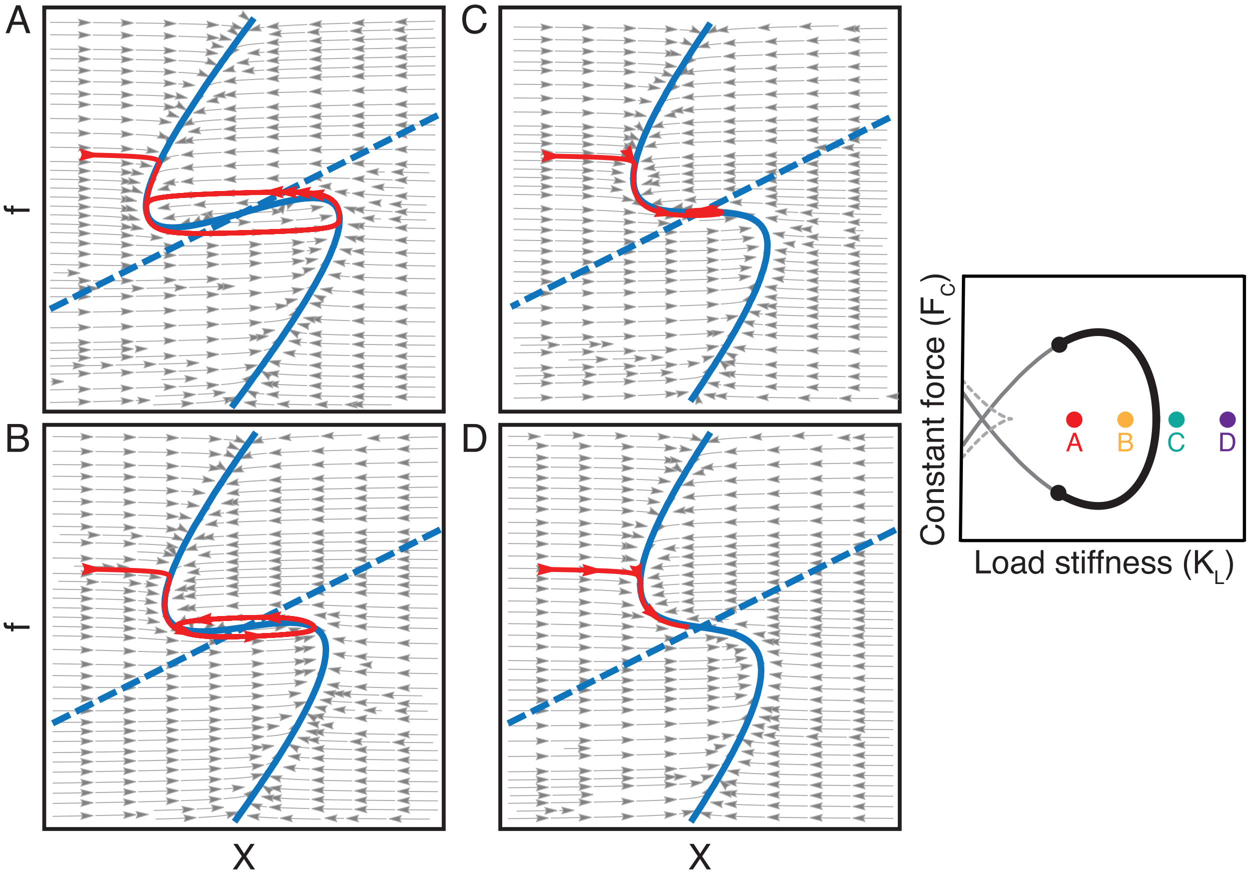

Figure S16: **Vector fields for a model hair bundle as a function of stiffness.** We calculated the vector fields in the bundle's position X and the adaptive force f. As shown in the rightmost panel, we subjected the hair bundle to a constant force of 0 and stiffnesses of 2.5 (A), 3 (B), 3.5 (C), and 4 (D); the bundle's operating point crossed a supercritical Hopf bifurcation at a stiffness of 3.4. A fixed point resided at the intersection of the $\dot{X} = 0$ (solid blue) and $\dot{f} = 0$ (dashed blue) nullclines. Gray arrows indicate the trajectories' local directions. Red curves and arrows highlight example trajectories in the absence of noise. All panels were generated in Mathematica (10.2.0.0).

G.2 Quasi-Threshold Behavior in a Bundle Model

We hypothesized that a hair bundle's stiffness and constant force control its capacity to exhibit large-amplitude spikes in the presence of noise. To assess this possibility, we simulated a hair bundle's response to shocks—instantaneous changes in X—that mimicked noisy perturbations to the bundle's position starting at the system's stable fixed point (Fig. S17). These shocks could induce excursions that appeared to be all-or-none spikes arising from quasi-thresholds in the bundle's phase portrait. Unlike a true threshold with a well-defined boundary, a quasi-threshold corresponds to a region near a stable fixed point in which nearby trajectories can diverge from one another. All shocks that exceed the quasi-threshold region cause large excursions of indistinguishable amplitudes. For this reason, crossing a quasi-threshold leads to a behavior similar to the that obtained by crossing a true threshold. A quasi-threshold region may be so narrow that it becomes difficult to distinguish it from a true threshold. A classic example of this phenomenon can be found in the Hodgkin-Huxley model of neurons, in which large-amplitude excursions resembling all-or-none spikes arise from quasi-threshold behavior [21, 23].

We searched for a quasi-threshold's location by manually iterating through different shock magnitudes and defined the quasi-threshold as the value of X at which trajectories diverged from one another and beyond which a family of trajectories possessed amplitudes that were indistinguishable from one another within a certain resolution. When the stiffness was low and the bundle operated closer to a subcritical Hopf bifurcation, the bundle exhibited a large-amplitude spike if the shock exceeded a quasi-threshold over a broad range of constant forces. Increasing the bundle's stiffness caused the spike amplitude to fall and the range of constant forces over which quasi-threshold behavior could occur to decrease, but the magnitude of the shock required to exceed the quasi-threshold shrunk owing to the fact that the bundle's operating point resided closer to a Hopf bifurcation. When the stiffness was high and the bundle operated closer to a supercritical Hopf bifurcation, no quasi-threshold was found for shocks in X across all constant forces. Here the bundle rang in response to a shock with an amplitude that grew with the shock's magnitude.

Quasi-threshold phenomena in a bundle's response to shocks arose from its specific dynamics rather than the behavior of a system described by the normal form of a subcritical Hopf bifurcation. To illustrate these dynamics, we calculated a hair bundle's response to shocks in phase space using the same parameters as before. Increases in a bundle's constant force induced translation of the $\dot{X} = 0$ nullcline, causing the stable fixed point to move farther from the location of a quasi-threshold in the X-direction (Fig. S18). Shocks of larger magnitude were therefore required to induce a spike as the constant force rose. When the constant force was very large, the bundle's fixed point fell below the middle branch of the $\dot{X} = 0$ nullcline. Increasing a bundle's stiffness caused the middle part of the $\dot{X} = 0$ nullcline to become shallower. This had two effects. First, the amplitude of shock-induced spikes decreased as the stiffness rose. Second, nearby trajectories no longer diverged as sharply from a region near the middle branch of the $\dot{X} = 0$ nullcline. As a result, the range of constant forces over which a quasi-threshold existed fell with an increase in stiffness. No quasi-threshold was found for shocks in X across all constant forces at stiffnesses of 2.6 and 3.0.

Noise can induce shocks in the f as well as the X direction. A quasi-threshold thus corresponds to an area in the bundle's phase portrait. For illustration, we analyzed shocks in only the X direction rather than in both the X and f directions. Noise-induced excursions resembling all-or-none spikes therefore arise from a quasi-threshold in a hair bundle's phase space. These spikes achieve similar amplitudes and can be elicited over a broader range of constant forces when the bundle's operating point lies in the low-stiffness regime. The spike amplitude additionally increases for smaller stiffness values. Finally, the perturbation size required for a bundle to spike falls as changes in constant force bring the system's operating point toward a line of subcritical Hopf bifurcations.

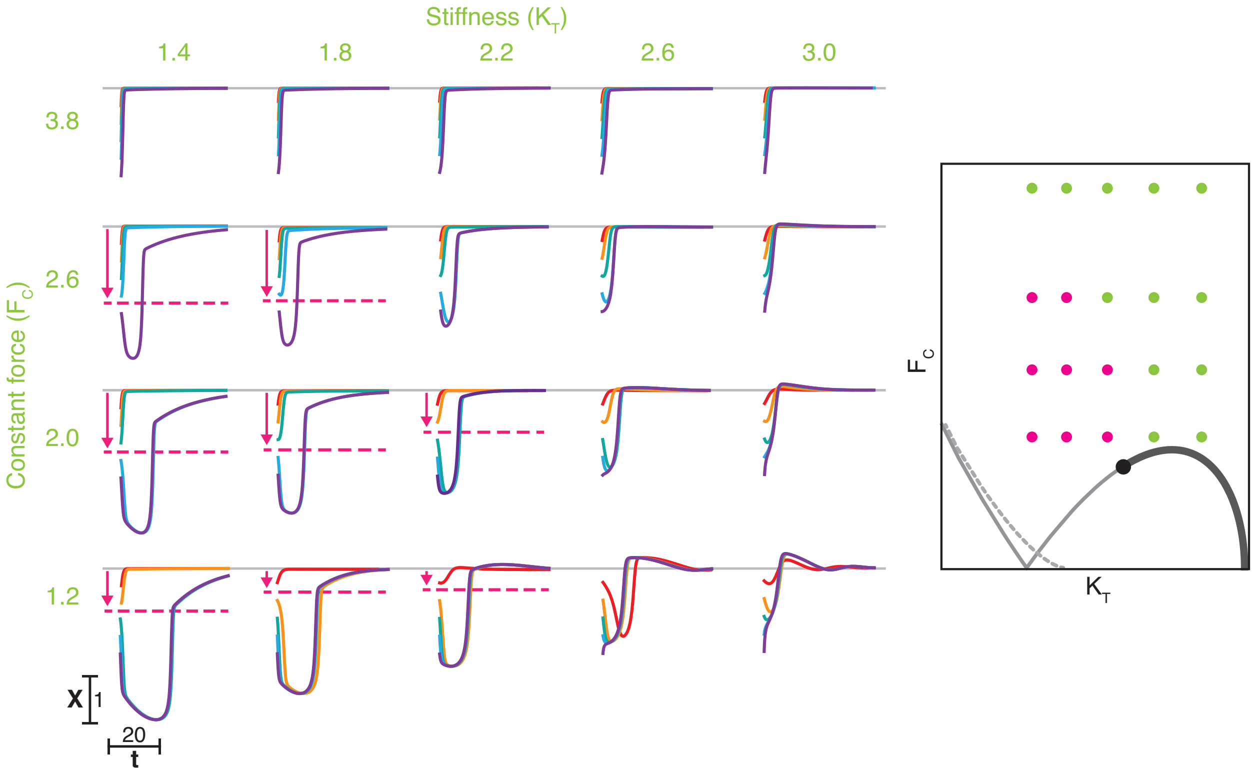

Figure S17: **Time series of a model bundle's response to instantaneous changes in its position.** A model hair bundle was subjected to constant forces of $F_C = \{1.2, 2.0, 2.6, 3.8\}$ and stiffnesses of $K_T = \{1.4, 1.8, 2.2, 2.6, 3.0\}$. The locations of these operating points are represented in the schematic state diagram on the right, in which dashed, thin, and thick lines correspond respectively to lines of fold, subcritical Hopf, and supercritical Hopf bifurcations. Pink circles correspond to those operating points at which a quasi-threshold was found. At each operating point, the bundle's dynamics was simulated using five different initial conditions. Each initial condition corresponded to the fixed-point value for f but to different values for X, each separated by $\Delta X = 0.4$ (red to purple). Pink dashed lines and arrows correspond to the approximate location in X of a quasi-threshold. If the bundle's position exceeded the quasi-threshold, the bundle exhibited a large-amplitude excursion that resembled an all-or-none spike. The distance between the bundle's steady-state position and the quasi-threshold at a given stiffness rose with an increase in constant force. No quasi-threshold existed for the constant forces shown at stiffness values of 2.6 and 3.0. In the absence of a quasi-threshold, the bundle instead exhibited ringing with an amplitude that grew with the bundle's initial position. All simulations were generated from Equations S31 and S32 in Mathematica (10.2.0.0).

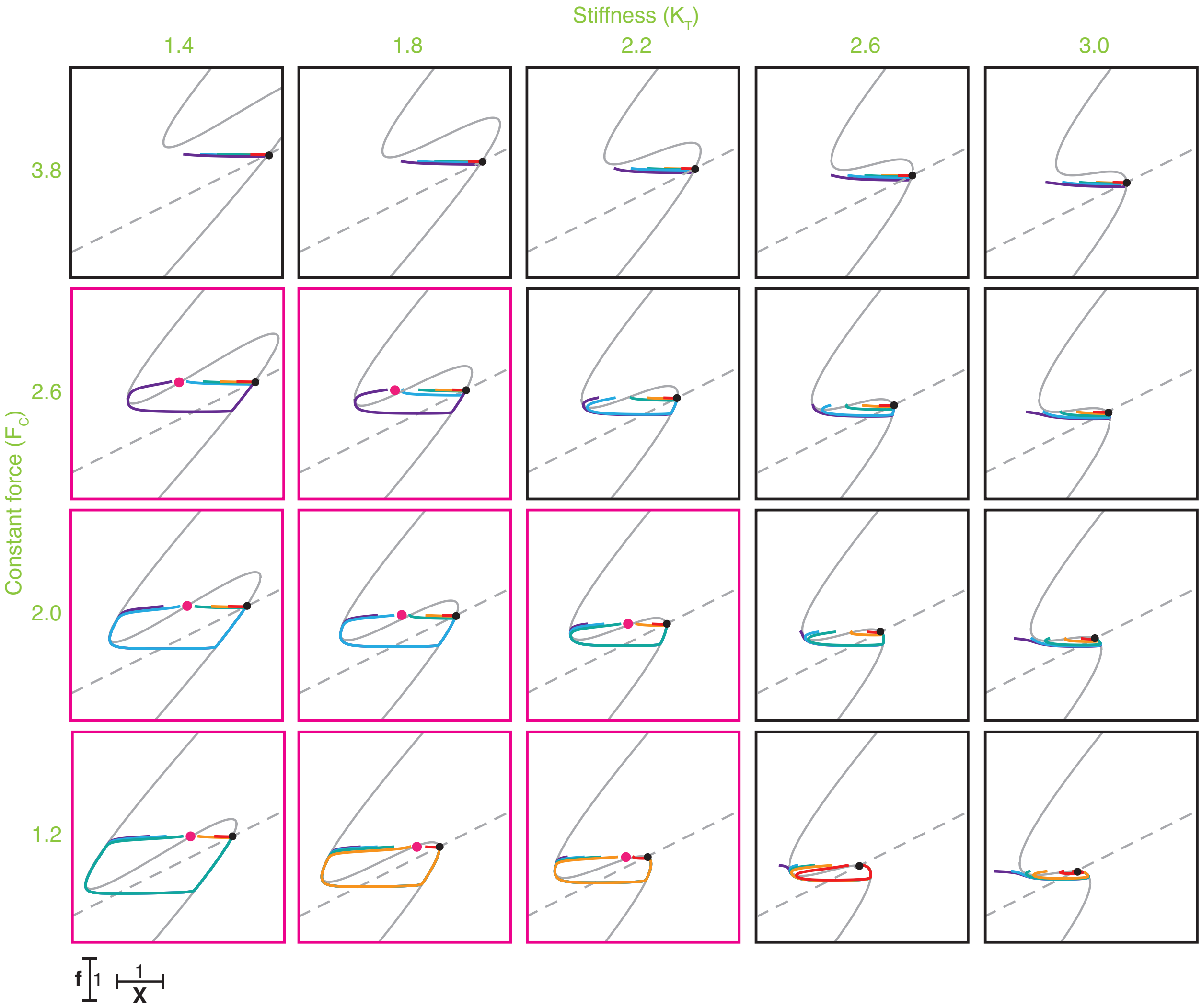

Figure S18: **Phase portraits of a model bundle's response to instantaneous changes in its position.** Using the same parameters as for Fig. S17, we simulated a model hair bundle's trajectory in phase space. Solid and dashed gray lines correspond respectively to the $\dot{X} = 0$ and $\dot{f} = 0$ nullclines. Black circles at the intersection of these nullclines correspond to stable fixed points. Pink circles approximate the location of a quasi-threshold. Those operating points for which a quasi-threshold existed are outlined in pink. Each colored curve represents the bundle's trajectory starting at a fixed value of f and increasing initial positions in X (red to purple). All trajectories evolved to eventually reside at the stable fixed point for each operating point. Increases in constant force shifted the $\dot{X} = 0$ nullcline in the positive X- and f-directions. This caused the distance between the bundle's stable fixed point and its quasi-threshold to grow. When the constant force increased to 3.8 the fixed point fell below the middle part of the $\dot{X} = 0$ nullcline, rendering the quasi-threshold inaccessible to shocks in the bundle's position X. As the stiffness increased, the slope of the middle part of the $\dot{X} = 0$ nullcline declined, causing the magnitude of shock-induced spikes to decrease and the range of constant forces over which a quasi-threshold existed to fall. No quasi-threshold in the X-direction existed for any value of constant force at stiffnesses of 2.6 and 3.0. All simulations were generated from Equations S31 and S32 in Mathematica (10.2.0.0).

References

[1] Salvi, J. D., D. Ó Maoiléidigh, B. A. Fabella, M. Tobin, and A. J. Hudspeth. 2015. Characterization of Active Hair-Bundle Motility by a Mechanical-Load Clamp. In K. D. Karavitaki and D. P. Corey (Eds.), Mechanics of Hearing: Protein to Perception, pages 030005:1–5.

[2] Salvi, J. D., D. Ó Maoiléidigh, B. A. Fabella, M. Tobin, and A. J. Hudspeth. 2015. Control of a hair bundle's mechanosensory function by its mechanical load. Proceedings of the National Academy of Sciences 112(9):E1000–9.

[3] Ó Maoiléidigh, D., E. M. Nicola, and A. J. Hudpseth. 2012. The diverse effects of mechanical loading on active hair bundles. Proceedings of the National Academy of Sciences of the United States of America 109(6):1943–1948.

[4] Bormuth, V., J. Barral, J.-F. Joanny, F. Jülicher, and P. Martin. 2014. Transduction channels' gating can control friction on vibrating hair-cell bundles in the ear. Proceedings of the National Academy of Sciences of the United States of America 111(20):7185–7190.

[5] Hartigan, J. A. and P. M. Hartigan. 1985. The dip test of unimodality. The Annals of Statistics 13(1):70–84.

[6] Freedman, D. and P. Diaconis. 1981. On the histogram as a density estimator: L2 theory. Probability Theory and Related Fields (Heidelberg: Springer Berlin) 57(4):453–476.

[7] Jacobson, M. L. 2001. Auto-Threshold Peak Detection in Physiological Signals. 23rd Annual International Conference of the IEEE Engineering in Medicine and Biology Society pages 1–4.

[8] Whitney, H. 1936. Differential manifolds. Annals of Mathematics 37(3):645–680.

[9] Takens, F. 1981. Detecting strange attractors in turbulence. Lecture Notes in Mathematics 898.

[10] Kennell, M. B. and H. D. I. Abarbanel. 2002. False neighbors and false strands: A reliable minimum embedding dimension algorithm. Physical Review E 66:026209.

[11] Fraser, A. M. and H. L. Swinney. 1986. Independent coordinates for strange attractors from mutual information. Physical Review A 33(2):1134–1140.

[12] Sauer, T., J. A. Yorke, and M. Casdagli. 1991. Embedology. Journal of Statistical Physics 65(3):579–616.

[13] Kralemann, B., L. Cimponeriu, M. Rosenblum, A. Pikovsky, and R. Mrowka. 2007. Uncovering interaction of coupled oscillators from data. Physical Review E 76(055201(R)):1–4.

[14] Kralemann, B., L. Cimponeriu, M. Rosenblum, A. Pikovsky, and R. Mrowka. 2008. Phase dynamics of coupled oscillators reconstructed from data. Physical Review E 77(066205):1–16.

[15] Zhu, Y., Y.-H. Hsieh, R. R. Dhingra, T. E. Dick, F. J. Jacono, and R. F. Galán. 2013. Quantifying interactions between real oscillators with information theory and phase models: Application to cardiorespiratory coupling. Physical Review E 87(2):022709.

[16] Ermentrout, G. B. and N. Kopell. 1986. Parabolic bursting in an excitable system coupled with a slow oscillation. SIAM Journal on Applied Mathematics 46(2):233–253.

[17] Ermentrout, B. 1996. Type I membranes, phase resetting curves, and synchrony. Neural Computation 8(5):979–1001.

[18] McKennoch, S., T. Voegtlin, and L. Bushnell. 2008. Spike-timing error backpropagation in theta neuron networks. Neural Computation 21(1):9–45.

[19] Kuznetsov, Y. 2004. Elements of Applied Bifurcation Theory. Applied Mathematical Sciences. Springer.

[20] FitzHugh, R. 1955. Mathematical models of threshold phenomena in the nerve membrane. Bulletin of Mathematical Biophysics 17(4):257–278.

[21] Izhikevich, E. M. 2000. Neural excitability, spiking and bursting. International Journal of Bifurcation and Chaos 10(6):1171–1266.

[22] Rinzel, J. and G. B. Ermentrout. 1989. Analysis of neural excitability and oscillations. Methods in neuronal modeling: From synapses to networks. MIT Press (Cambridge, MA).

[23] Izhikevich, E. M. 2007. Dynamical Systems in Neuroscience: The Geometry of Excitability. The MIT Press (Cambridge, MA).

[24] Treutlein, H. and K. Schulten. 1985. Noise induced limit cycles of the bonhoeffer-van der pol model of neural pulses. Berichte der Bunsen-Gesellschaft für Physikalische Chemie 89:710–718.

[25] Lindner, B., J. García-Ojalvo, A. Neiman, and L. Schimansky-Geier. 2004. Effects of noise in excitable systems. Physics Reports 392:321–424.